

Diss. ETH No 13804

Control of Circular Cylinder Wakes
using Base Mass Actuation

A dissertation submitted to the
SWISS FEDERAL INSTITUTE OF TECHNOLOGY ZURICH

for the degree of
Doctor of Technical Sciences

presented by
Yannick Delaunay
Mechanical Engineer

born 23.06.72
citizen of France

Accepted on the recommendation of
Prof. Dr. L. Guzzella, examiner
Prof. Dr. P. Koumoutsakos, co-examiner
Dr. L. Kaiktsis, co-examiner

2000

Seite Leer /
Blank leaf

A ma femme,
Magdalena,
et mes enfants,
Daniel,
Roxane,
Camille

Seite Leer /
Blank leaf

Abstract

The dynamical behaviour and stability properties of the circular cylinder wake subject to passive control is investigated using Direct Numerical Simulation (DNS) and stability analysis. The control action consists of either suction or blowing at a steady flow rate from a control arc symmetrically placed at the cylinder base. The study is limited to two-dimensional flows, at low Reynolds numbers ($Re \leq 90$), where the non-manipulated flow is either steady or characterized by vortex shedding.

DNS results show that, in the supercritical Reynolds number regime ($Re > 47$), slight blowing or high enough suction stabilizes the wake; in the subcritical regime, suction can destabilize the wake for $Re > 17$, and result in vortex shedding, whereas blowing does not affect the flow stability in this regime.

At supercritical Reynolds numbers, suction can strongly modify the dynamics of vortex shedding, in comparison to the uncontrolled flow. With increasing suction, the flow frequency can drastically decrease, while the fluctuation amplitudes increase. At a critical suction flow rate, the flow undergoes a first bifurcation: it becomes steady and asymmetric simultaneously. At a higher critical suction flow rate, the flow undergoes a second bifurcation and becomes steady symmetric.

With increasing suction flow rate, the flow state is naturally affected away from the cylinder base. However, the computational domains used have finite size, and the assumption of free stream velocity is made at the inflow and lateral boundaries. The study of the effects of computational domain size on the simulation results suggests that the transition from a steady asymmetric flow to a steady symmetric flow at very high suction flow rates, found with the use of computational domains of finite size, may not exist in an infinite flow domain. This transition occurs at increasing suction flow rate with increasing domain size.

Global linear stability analysis calculations confirm the main results of the numerical simulations. They show furthermore that, at supercritical Reynolds numbers, small suction has an even further destabilizing effect, as it increases the global growth rate of small perturbations superimposed on the steady symmetric base flow solutions. High enough suction is necessary to inverse the global growth rate trend and lead to negative values, as also deduced from DNS. Stability analysis strongly supports the hypothesis that the transition from steady asymmetric to steady symmetric flow would not exist in an infinite flow domain.

Seite Leer /
Blank leaf

Übersicht

Das dynamische Verhalten und die Stabilitätseigenschaften der gesteuerten Nachlaufströmung hinter einem kreisförmigen Zylinder werden mittels direkter numerischer Simulationen (DNS) und Stabilitätsanalyse untersucht. Zur Steuerung wird Fluid durch einen symmetrisch auf der Zylinderbasis angeordneten Bogen stationär entweder abgesaugt oder eingeblassen. Die Studie beschränkt sich auf zwei-dimensionale Strömungen bei tiefen Reynoldszahlen ($Re \leq 90$), im stationären Zustand oder mit Wirbelablösung.

Die DNS-Ergebnisse zeigen, dass bei überkritischen Reynoldszahlen ($Re > 47$) sowohl leichtes Blasen als auch genügend starkes Absaugen die Nachlaufströmung stabilisieren kann. Im subkritischen Regime, und für $Re > 17$, kann nur Absaugen die Strömung destabilisieren, wobei sich eine Wirbelablösung ergibt; Blasen hat keine Auswirkung auf die Stabilität der Strömung in diesem Regime.

Im Vergleich zum ungesteuerten System kann bei überkritischen Reynoldszahlen die Dynamik der von Kármán-Wirbelstrasse durch Absaugen stark modifiziert werden. Mit zunehmendem Absaugen kann die Frequenz der Strömungsschwingungen stark reduziert und dabei deren Amplitude erhöht werden. Bei einem kritischen Absaugdurchfluss tritt eine erste Bifurcation auf: die Strömung wird gleichzeitig stationär und asymmetrisch. Bei einem höheren kritischen Absaugdurchfluss wird eine zweite Bifurcation beobachtet, wobei die Strömung stationär und symmetrisch wird.

Mit zunehmendem Absaugdurchfluss wird die Strömung in immer grösserer Distanz vom Zylinder beeinflusst. Zur Simulation jeder Strömung wurde jedoch stets ein begrenzter Bereich betrachtet, unter Annahme freier Strömungsgeschwindigkeit an den seitlich und strom-aufwärts vom Zylinder platzierten Bereichsgrenzen. Aus einer Studie der Auswirkungen der Netzgrösse auf die Simulationsergebnisse ergibt sich, dass der Übergang von stationär-asymmetrischen zu stationär-symmetrischen Strömungen - üblicherweise im begrenzten Netz ermittelt - in einem unendlichen Strömungsfeld wahrscheinlich nicht stattfinden würde. Mit zunehmender Bereichsgrösse tritt dieser Übergang bei steigendem Absaugdurchfluss auf.

Die Stabilitätsanalysen bestätigen die Ergebnisse der direkten numerischen Simulation. Sie zeigen ausserdem, dass bei überkritischen Reynoldszahlen leichtes Absaugen eine vermehrt destabilisierende Wirkung hat, da die Wachstumsrate kleiner Störungen dadurch erhöht wird. Wie schon anhand der direkten Simulationen beobachtet, ist genügend starkes

Absaugen notwendig, um diese Tendenz umzukehren und die Wachstumsrate auf Werte unter Null zu reduzieren. Die Resultate der Stabilitätsanalyse stützen die Hypothese, dass der Übergang vom stationär-asymmetrischen zum stationär-symmetrischen Strömungszustand in einem unendlichen Strömungsfeld nicht existieren würde.

Acknowledgements

During the preparation of my thesis, I had the chance to be supported by many people, to whom I would like to express my deep gratitude.

I would like to thank, first and foremost, my mentor Dr. L. Kaiktsis for his strong involvement in and his constant support in my work, and for providing me with a very pleasant work environment.

My supervisor Prof. L. Guzzella has not only supported and motivated me during these three years of research work, but also involved himself to make my family life in Zürich possible. I would like to express to him deepest thanks in the name of the family.

Special thanks go to my closest colleagues from the laboratory of combustion, for all the technical discussions and for being always available to support me in any kind of problem, and for their friendship, Dr. J. Lee, Dr. C. Frouzakis, and Dr. A. Tomboulides.

Special thanks go to Prof. P. Koumoutsakos for the fruitful discussions and comments on my work; and to Dr. D. Barkley and Dr. R. Henderdon for providing me the global stability code and technical support.

Technical support on the CRAY SV1, the HP/Convex Exemplar SPP2000/X-32 and my own SGI workstation was kindly provided by Mr. B. Loepfe, Mr. T. Racic and Mr. M. Essig. Dr. O. Byrde has given me precious help in optimizing and debugging all my applications on the CRAY.

This project was supported financially by the Swiss Federal Institute of Technology of Zürich (ETHZ).

Seite Leer /
Blank leaf

Contents

1	Introduction	1
1.1	Flow around a circular cylinder: a prototype flow past bluff bodies	1
1.2	Brief review of hydrodynamic stability concepts	3
1.3	Flow control: motivation and applications	10
2	Problem definition	15
2.1	Basic flow setup	15
2.2	Problem formulation	15
2.3	Numerical method	18
2.3.1	Temporal discretization	19
2.3.2	Spatial discretization	21
3	Resolution and validation tests	23
3.1	Basic validation tests	23
3.2	Tolerance in velocity iterative solver and system stability	27
3.2.1	Instability suppression due to numerics	28
3.2.2	Instability triggered by a jump in the system parameter	28
3.3	Spatial and temporal resolution tests	35
3.4	Validation with the Stuart-Landau model	38
3.5	Mass conservation	47
3.6	Summary	51

4	Flow control simulations	53
4.1	The flow under control action	53
4.2	Feedback control method	70
5	Domain size and boundary conditions effects	77
5.1	Domain size effects	77
5.1.1	Effects on shedding period	79
5.1.2	Effects on flow transitions	81
5.2	Boundary conditions effects	84
5.3	Summary	87
6	Stability analysis	91
7	Conclusions	101
A	Temporal Resolution Tests	103
	Bibliography	113

List of Figures

1.1	Colour-coded vorticity isocontours of the circular cylinder wake at $Re = 90$.	4
1.2	Sketch of spatio-temporal evolution of a perturbation u' in a parallel flow, in the cases of (a) linearly stable, (b) convectively unstable, and (c) absolutely unstable flow. Flow direction: left to right.	8
1.3	Sketch of a typical near wake velocity profile.	8
2.1	Sketch of the flow set-up with control action (here only the blowing case is illustrated).	16
2.2	Spectral element skeleton used for the flow around a circular cylinder: (a) entire mesh, (b) elements close to the cylinder.	17
3.1	Time-averaged total drag coefficient versus Reynolds number (uncontrolled flow).	24
3.2	Strouhal number versus Reynolds number (uncontrolled flow).	25
3.3	Recirculation length, normalized by cylinder diameter, versus Reynolds number (uncontrolled flow).	26
3.4	Time-history of V-velocity offset at points A, D and E, for $Re=70$, $C_{suc}=0$. The initial condition is the steady symmetric solution.	29
3.5	Time-history of U- and V-velocity at point A. $Re=45$ at $t=0$, Re is increased by an increment of 5 every 200 time steps. $TOL = 10^{-8}$.	30
3.6	Transient signals of V-velocity at point A, illustrating the effect of time step (Δt) and tolerance (TOL) in the velocity iterative solver on global mode evolution. Here $Re=50$, while the initial condition is the steady field at $Re=45$.	33
3.7	CPU seconds per time step, versus TOL value. $Re=80$, $C_{suc}=0.90$, 9×9 resolution.	34

3.8	U- and V-velocity time-history at point A, illustrating the growth and saturation of global instability at $Re=60$	40
3.9	(a) Instantaneous growth rate $\frac{1}{ A } \frac{d A }{dt}$ and (b) instantaneous frequency f of the uncontrolled flow at $Re=50$, versus global mode amplitude $ A ^2$. The data are obtained from the analysis of V-velocity signal at point A.	45
3.10	(a) Instantaneous growth rate $\frac{1}{ A } \frac{d A }{dt}$ and (b) instantaneous frequency f of the uncontrolled flow at $Re=60$, versus global mode amplitude $ A ^2$. The data are obtained from the analysis of V-velocity signal at point A.	46
3.11	Instantaneous divergence fields at different system parameter values and spatial resolutions. The region of suction is delimited by the two white lines. The structure of the grid near the cylinder base is shown for (a) the original grid and (f) the h-refined grid.	48
3.12	V-velocity profile along the centerline ($y = 0$) at $Re=90$, $C_{suc}=1.4$	50
4.1	Flow states and critical curves in the parameter plane, $Re - C_{suc}$	54
4.2	Strouhal number versus suction coefficient at different Reynolds numbers. . .	55
4.3	(a) u'_{max} and (b) v'_{max} versus suction coefficient at different Reynolds numbers.	56
4.4	$Re=90$: maximum RMS fluctuations along lines of constant x , u'_y and v'_y , versus streamwise abscissa, for different suction coefficients.	58
4.5	$Re=90$, $C_{suc}=-0.14$: colour-coded instantaneous vorticity isocontours.	58
4.6	$Re=90$: time history of the V-velocity on the limit cycle at point A, for different suction coefficient values.	59
4.7	$Re=90$, $C_{suc}=0.8$: time evolution of vorticity over one shedding period ($T_0=72.8$).	60
4.8	$Re=90$: wake transient (V-velocity at point A) as the suction coefficient is impulsively increased from $C_{suc}=0.85$ to $C_{suc}=1.0$	61
4.9	$Re=30$, $C_{suc}=1.65$: time history of V-velocity at point A on the limit cycle.	63
4.10	$Re=30$: colour-coded instantaneous vorticity contours. (a) $C_{suc}=1.2$, (b) $C_{suc}=1.4$	64
4.11	$Re=90$: absolute value of time-averaged V_A value versus C_{suc}	65
4.12	$Re=90$, $C_{suc}=1.0$: streamline pattern of the time-asymptotic flow state.	66
4.13	$Re=90$, $C_{suc}=1.0$: (a) streamwise velocity and (b) pressure fields in the region close to the cylinder.	67

4.14	$Re=90$: deflection of front stagnation point (angle in degrees) with respect to the centerline, versus suction coefficient.	68
4.15	$Re=90$: drag and lift coefficients versus C_{suc} ; full symbols correspond to steady symmetric solutions. In the unsteady regime, the time-averaged value of the drag, and the amplitude of the lift coefficients are reported. Also sketched: flow structure (streamlines) in the asymmetric regime.	69
4.16	Sketch of the time evolution of the dominant global mode for two levels of initial perturbation, in the case of a subcritical bifurcation ($\sigma_r < 0$, $l_r < 0$).	71
4.17	$Re=90$: time history of V-velocity at point A, indicating the response of a non-saturated flow to a small C_{suc} jump (from 1.7 to 1.72 at $t=0$).	72
4.18	Control algorithm used to compute unstable asymmetric solutions.	73
4.19	Sketch of the improved C_{suc} update. The “new C_{suc} ” corresponds to $\frac{d V_A }{dt}=0$, in the linear interpolation between $(C_{suc,min}, (\frac{d V_A }{dt})_{min})$ and $(C_{suc,max}, (\frac{d V_A }{dt})_{max})$	75
4.20	$Re=90$: (a) time histories of V-velocity at point A and C_{suc} , while the flow is subject to feedback control, with $V_{target}=0.011$, (b) Phase-portrait in the $C_{suc} - V_A $ plane (the dashed curve represents the unstable branch).	76
5.1	Computational domains used, and corresponding numbers of elements. The cylinder is also represented (to scale).	78
5.2	Boundary of unsteady flow regime in the parameter plane (Re , C_{suc}). Parameter sets (crosses) chosen for frequency comparison tests are also indicated.	80
5.3	$Re=90$, $C_{suc}=0.4$: phase space plot at points A and E: V-velocity vs. U-velocity.	82
5.4	$C_{suc}=2.0$: bifurcation diagram for the transition from steady symmetric to steady asymmetric flow: V_A versus Re	83
5.5	$Re=90$: Bifurcation diagram: $ V_A $ versus C_{suc}	85
5.6	$Re=90$: critical suction coefficients $C_{suc,2}$ and $C_{suc,3}$ versus DX_{IN}	86
5.7	$Re=90$, $C_{suc}=1.8$: V-velocity profile along the y axis at $X = -30$ in the ‘XLW’ domain.	87
6.1	$Re=90$: global growth rate (σ_r), linear frequency ($\sigma_i/2\pi$), and non-linear frequency (St), versus suction coefficient C_{suc} , for symmetric base flow solutions. Data obtained with the domain ‘MAIN’, unless otherwise stated.	95

6.2	$Re=90$: U and V isocontours of the dominant eigenmode corresponding to the base symmetric flow at (a) $C_{suc}=0.4$, (b) $C_{suc}=0.8$	98
6.3	$Re=90$: global growth rate σ_r corresponding to different types of base flow, versus suction coefficient C_{suc} . The dotted lines correspond to exponential curve fits of the ‘XLW’ data.	99
A.1	Time-history of V -velocity at point A: $Re=30$, $C_{suc}=0.90$, 7×7 elemental resolution: — $\Delta t=0.001$, - - - $\Delta t=0.002$. (a) Growth and saturation of global mode, using the base flow slightly perturbed as initial condition. (b) Initial stage of global mode development, using the base flow as initial condition. .	104
A.2	Time-history of V -velocity at point A: $Re=30$, $C_{suc}=0.90$, 11×11 elemental resolution: — $\Delta t=0.001$, - - - $\Delta t=0.002$. (a) Growth and saturation of global mode, using the base flow slightly perturbed as initial condition. (b) Initial stage of global mode development, using the base flow as initial condition. .	105
A.3	Time-history of V -velocity at point A: $Re=50$, $C_{suc}=1.50$, 7×7 elemental resolution: — $\Delta t=0.00075$, - - - $\Delta t=0.0015$. (a) Growth and saturation of global mode, using the base flow slightly perturbed as initial condition. (b) Initial stage of global mode development, using the base flow as initial condition. .	106
A.4	Time-history of V -velocity at point A: $Re=50$, $C_{suc}=1.50$, 9×9 elemental resolution: — $\Delta t=0.0012$, - - - $\Delta t=0.0007$. (a) Growth and saturation of global mode, using the base flow slightly perturbed as initial condition. (b) Initial stage of global mode development, using the base flow as initial condition. .	107
A.5	Time-history of V -velocity at point A: $Re=90$, $C_{suc}=-0.10$, 7×7 elemental resolution: — $\Delta t=0.0075$, - - - $\Delta t=0.015$. (a) Growth and saturation of global mode, using the base flow slightly perturbed as initial condition. (b) Initial stage of global mode development, using the base flow as initial condition.	108
A.6	Time-history of V -velocity at point A: $Re=90$, $C_{suc}=-0.10$, 9×9 elemental resolution: — $\Delta t=0.0075$, - - - $\Delta t=0.015$. (a) Growth and saturation of global mode, using the base flow slightly perturbed as initial condition. (b) Initial stage of global mode development, using the base flow as initial condition.	109

- A.7 Time-history of V-velocity at point A: $Re=90$, $C_{suc}=0.85$, 7×7 elemental resolution: — $\Delta t=0.001$, - - - $\Delta t=0.002$. (a) Growth and saturation of global mode, using the base flow slightly perturbed as initial condition. (b) Initial stage of global mode development, using the base flow as initial condition. . 110
- A.8 Time-history of V-velocity at point A: $Re=90$, $C_{suc}=0.85$, 9×9 elemental resolution: — $\Delta t=0.001$, - - - $\Delta t=0.002$. (a) Growth and saturation of global mode, using the base flow slightly perturbed as initial condition. (b) Initial stage of global mode development, using the base flow as initial condition. . 111

Seite Leer /
Blank leaf

List of Tables

2.1	Coordinates of the observation points.	18
3.1	Spatial resolution tests: Strouhal number and drag coefficient values corresponding to seven parameter sets.	37
3.2	Coefficients of the Stuart-Landau equation at $Re=50$ and $Re=60$, corresponding to the present (computational) and previous (experimental) studies. . . .	44
5.1	Domain names and characteristic dimensions in terms of diameter lengths: DX_{IN} and DX_{OUT} stand for the distances from the cylinder center to the inflow and outflow boundaries, respectively; DY stands for the total domain width.	79
5.2	Flow oscillation period at different parameter sets.	81
5.3	Critical suction coefficient values obtained with the domain ‘MAIN’ and four different types of velocity boundary conditions on the lateral boundaries (the velocity imposed at the inflow boundary is the free stream velocity, if not otherwise stated): free stream, potential (also at the inflow boundary), symmetry boundary condition, and periodic boundary conditions. Also reported: values obtained with the domain ‘OUT’, whereby the free stream boundary condition is applied.	88
6.1	Uncontrolled flow: global linear growth rates and temporal frequencies, based on the Stuart-Landau model (SL), and on stability analysis calculations (SA). . . .	93

Seite Leer /
Blank leaf

Chapter 1

Introduction

1.1 Flow around a circular cylinder: a prototype flow past bluff bodies

Flows around bluff bodies have been extensively studied for more than a century, with first efforts dating back to 1878, with the experimental observations of Strouhal (1878) on the frequency dependence of aeolian tones. He found that the frequency depends on the surrounding fluid velocity rather than on the properties of the wire material. Since then, a very important parameter in bluff body flows, the ‘Strouhal number’, representing the non-dimensional flow oscillation frequency, is named after him. Subsequently, a large number of experiments, and much later, numerical simulations have been carried out to characterize flows past bluff bodies, with the flow around a circular cylinder being the one studied most extensively. Thus, a large amount of information and data on the dynamics and other flow properties is now available in the literature. However, the topic is far from being closed, and detailed studies on the prototype problem of the circular cylinder wake are still underway. The practical importance of wake flows (for example in aerodynamics), and the fact that they still defy our understanding make them a subject of particular interest. As indicated in Fornberg (1993), the cylinder wake belongs to those systems that are easy to define, but represent a real challenge to solve and understand their behaviour, making them only more attractive. Up to the last few decades, research objectives were focused on the dynamics and physical properties of the uncontrolled flow in the steady or vortex shedding regime (for experimental results, see von Kármán 1911, Roshko 1954, Tritton 1959, Acrivos et al.

1968, Hammache and Gharib 1991, Green and Gerrard 1993, and for numerical studies, see Dennis and Chang 1970, Fornberg 1985, Braza et al. 1986). Detailed information related to the problem is also reviewed by Williamson (1996), who has significantly contributed to this field. Currently, a large number of wake flows studies focus on stability properties (see e.g. Důšek et al. 1994, Jackson 1987, Barkley and Henderson 1996, Důšek 1996) and to issues related to low order modeling, primarily for control purposes (Park 1994, Monkewitz 1996, Roussopoulos and Monkewitz 1996, Gillies 1998, Graham et al. 1999a & 1999b).

In the absence of external forces, the dynamics of the incompressible flow of a Newtonian fluid around a circular cylinder depends only on the Reynolds number (here defined in terms of the free stream velocity and the cylinder diameter). Properties of this flow are well known for a wide range of the Reynolds number, from creeping flows ($Re \rightarrow 0$) to fully turbulent flows ($Re \approx 10^7$). The flow regimes can be classified as follows:

For $Re < 6$, the flow is steady and two-dimensional, with only one separation point, at the rear stagnation point. This is the creeping flow regime, where the motion can be accurately described by the Stokes model—a simplification of the Navier-Stokes equations—, where the inertial terms (advection) are neglected and only the viscous and pressure stresses are considered in the momentum conservation equation.

In the range $6 < Re < 47$, the flow is still steady and two-dimensional, but a vortex pair appears behind the cylinder, the recirculation length of which increases linearly with Re .

As Re is increased above $Re_{2D,cr} \approx 47$, a periodic vortex shedding mode is excited in the wake. This transition corresponds to a Hopf bifurcation of the dynamical system (Jackson 1987, Důšek 1994). Note that the critical value of 47 is found by means of computational methods, which allow a perfectly two-dimensional flow. In the absence of end-wall effects, the flow remains strictly two-dimensional up to $Re \approx 200$, and forms a dynamical system which can be described by the Stuart-Landau equation (Mathis et al. 1984, Provansal et al. 1987).

At $Re \approx 200$, the flow undergoes a second bifurcation and becomes three-dimensional, as first reported in the numerical studies of Tomboulides et al. (1992) and Karniadakis and Triantafyllou (1992). Noack and Eckelmann (1994) and Barkley and Henderson (1996) performed Floquet stability analysis of the two-dimensional flow, and determined the critical Reynolds number at which the wake becomes three-dimensional. They reported the values of

$Re_{3D,cr}=170$ and $Re_{3D,cr}=188.5$, respectively; the different numerical methods used, with the one used by Barkley and Henderson being more accurate, lead to the discrepancy between the reported values. Nevertheless, they both concluded that the bifurcation occurs via a secondary instability mode in the spanwise direction.

As the Reynolds number is further increased above $Re_{3D,cr}$, a number of other transitions occur, represented in the plot of ‘base suction coefficient’ versus Reynolds number (see Roshko, 1993); the base suction coefficient (β) is defined by

$$\beta = \frac{p_\infty - p_b}{\frac{1}{2}\rho U_\infty^2} \quad (1.1)$$

where p_∞ and p_b represent the static pressure of the free stream and at the base rear stagnation point on the cylinder, respectively.

To summarize, in the range $0 < Re < 200$, there are two critical Reynolds numbers, $Re_{2D,cr} = 47$ and $Re_{3D,cr} = 188.5$. $Re_{2D,cr}$ is the threshold at which the wake first becomes oscillatory but remains two-dimensional, while $Re_{3D,cr}$ represents the threshold above which the wake becomes three-dimensional.

1.2 Brief review of hydrodynamic stability concepts

Early investigations on flow instability and transition to turbulence were conducted by Reynolds (1883), and Rayleigh (1892). An extensive review on the subject is given by Drazin and Reid (1981), and more recent theoretical advances can be found in Huerre and Monkewitz (1990).

Hydrodynamic instability is classified into two types: global and local. Global stability is related to the most common concept in dynamical systems. In two-dimensional flow problems, it is referred to as the asymptotic stability of a steady flow field. A globally unstable flow is characterized by the growth of self-sustained oscillations until a saturated non-linear state is reached. In the case of the circular cylinder wake, this results in the well known von Kármán vortex street, which is illustrated by the instantaneous vorticity contour plot for $Re=90$ (Figure 1.1). These oscillations, characterized by a single frequency over the entire flow field, form a limit cycle in the saturated non-linear regime. They are also referred to as a ‘global mode’, linear at the early stage of its formation, and non-linear in the limit cycle regime. A linear global mode becomes unstable when a system parameter, e.g. the

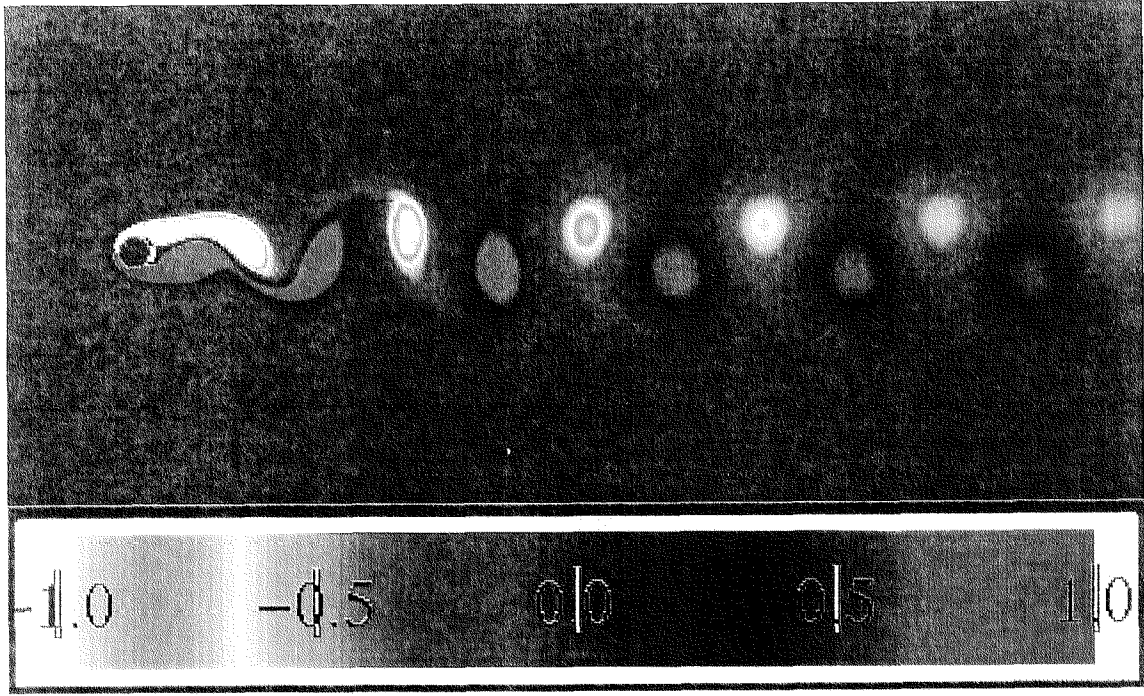


Figure 1.1: Colour-coded vorticity isocontours of the circular cylinder wake at $Re = 90$.

Reynolds number, is increased above a critical value. Linear global modes can be obtained by linearizing the Navier-Stokes equations around the steady solution, and by solving the corresponding eigenvalue problem. In two dimensions, the dynamics of a linear global mode has the form, when expressed in a cartesian coordinate system:

$$u'(x, y, t) = U'(x, y)e^{-i\Omega t} \quad (2a)$$

$$v'(x, y, t) = V'(x, y)e^{-i\Omega t} \quad (2b)$$

$$p'(x, y, t) = P'(x, y)e^{-i\Omega t} \quad (2c)$$

where (u', v') and p' are the instantaneous velocity and pressure perturbations fields, respectively, and Ω is the complex linear global frequency (eigenvalue of the linearized system): $\Omega = \Omega_R + i\Omega_I$. The condition for global instability is the existence of eigenmodes, defined by the fields (U', V', P') , such that $\Omega_I > 0$.

Global stability analysis is a general concept in dynamical systems, while local stability analysis is specific to the field of hydrodynamics. To perform local stability analysis, one must make the assumption of locally parallel flow. In a parallel flow, the velocity is unidirectional and does not depend on the streamwise coordinate, as for example in the case of the flow

inside a long pipe. In a spatially developing flow, which is not parallel by definition, the parallel flow assumption is legitimate if the wave-length λ of a typical instability is much shorter than the characteristic length scale L of the spatial evolution of the flow, i.e.:

$$\lambda \ll L. \quad (3)$$

The characteristic length scale L is defined as:

$$\frac{1}{L} = \frac{1}{\theta} \frac{d\theta}{dx} \quad (4)$$

where $\theta(x)$ represents a characteristic width, for example the momentum thickness.

Under the parallel flow assumption, the velocity vector of a two-dimensional steady ('base') flow, expressed in a cartesian coordinate system (x, y) , reduces to $(U(y), 0)$. We now consider a small initial perturbation superimposed on the base flow, and study its time evolution in terms of velocity (u', v') and pressure p' fluctuations:

$$u' = u'(x, y, t) \quad (5a)$$

$$v' = v'(x, y, t) \quad (5b)$$

$$p' = p'(x, y, t) \quad (5c)$$

The superposition of the base flow and the perturbation field must satisfy the Navier-Stokes equations. In linear stability analysis, the quadratic terms of velocity disturbances are neglected, since one studies the evolution of infinitesimal perturbations. The following partial differential equations governing the perturbation dynamics can be derived:

$$\frac{\partial u'}{\partial t} + U \frac{\partial u'}{\partial x} + v' \frac{dU}{dy} + \frac{1}{\rho} \frac{\partial p'}{\partial x} = \nu \nabla^2 u' \quad (6a)$$

$$\frac{\partial v'}{\partial t} + U \frac{\partial v'}{\partial x} + \frac{1}{\rho} \frac{\partial p'}{\partial y} = \nu \nabla^2 v' \quad (6b)$$

$$\frac{\partial u'}{\partial x} + \frac{\partial v'}{\partial y} = 0 \quad (6c)$$

where P is the pressure of the base flow, ρ is the fluid density and ν the kinematic viscosity.

A combination of equation (6a) and (6b) eliminates the pressure contributions, and together with equation (6c) yields a system of two partial differential equations for the unknowns $u'(x, y, t)$ and $v'(x, y, t)$, with coefficients that are functions of y only. Particular

solutions of this system have the form $F(y)e^{i(kx-\omega t)}$, where $k=k_r+ik_i$ and $\omega=\omega_r+i\omega_i$ represent the complex wavenumber and frequency, respectively. The frequency ω contains as real part the ‘local linear frequency’ ω_r , and as imaginary part the ‘local linear temporal growth rate’ ω_i . These particular solutions are called ‘normal modes’.

To proceed further, we need to introduce the streamfunction of the disturbance field, $\Psi'(x, y, t)$, defined in two-dimensional flows by:

$$u' = \frac{\partial \Psi'}{\partial y} \quad (7)$$

$$v' = -\frac{\partial \Psi'}{\partial x} \quad (8)$$

Hence, $\Psi'(x, y, t)$ necessarily has the form

$$\Psi'(x, y, t) = f(y)e^{i(kx-\omega t)}, \quad (9)$$

and

$$u'(x, y, t) = f'(y)e^{i(kx-\omega t)} \quad (10a)$$

$$v'(x, y, t) = -ikf(y)e^{i(kx-\omega t)} \quad (10b)$$

where $f'(y)$ denotes $\frac{df}{dy}$. Substituting the last two equations for u' and v' into equation (6a, 6b, 6c) yields the *Orr-Sommerfeld* equation:

$$(kU - \omega)(f'' - k^2f) - kU''f + i\nu(f'''' - 2k^2f''' + k^4f) = 0, \quad (11)$$

where primes denote y -derivatives. Note that the pressure does not appear in the final equation, which indicates that in local stability analysis, one invokes the stability of a ‘velocity profile’.

Equation (11) is a fourth order partial differential equation in f , and can be solved with appropriate boundary conditions. In the case of wall-bounded flows, the velocity perturbations must vanish at the walls due to the no-slip condition. Thus equation (10) gives $f=0$, $f'=0$ on the walls, and the trivial solution $f = 0$ satisfies equation (11) for any combination of the three parameters (k, ω, ν) . In the case of wake flows (and similarly in other open flows), vanishing velocity perturbations can also be used as boundary conditions at the profile boundaries, as long as the boundaries lie far enough, to a region where the effect of the bluff-body on the surrounding flow vanishes.

Non-trivial solutions to equation (11) exist only for particular combinations of the parameters k , ω , ν . These combinations are expressed by the dispersion relation, as follows:

$$F(\nu, k, \omega) = 0. \quad (12)$$

Typically, the viscosity ν is known, therefore this equation involves two complex unknown eigenvalues. Thus, in local stability calculations, one needs to assign the viscosity (Reynolds number) and either k or ω , and solve for the eigenvalues of the other complex unknown.

Local instabilities may be classified into absolute and convective type. The concepts of absolute and convective instability have been first introduced by Twiss (1952), in his work on plasma physics. The absolute or convective character of instability can be determined by performing temporal and spatial stability analysis.

In temporal stability analysis, one studies the evolution in time of spatially uniform wave packets, i.e. with real wavenumbers $k = k_r$. If for a certain value of k_r , ω_i becomes positive, then the profile is said to be absolutely unstable. In this case, a local small disturbance is amplified exponentially in time at an initial growth rate ω_i , and subsequently spreads throughout the entire flow field.

In spatial stability analysis, one studies the spatial evolution of time harmonic disturbances, i.e. $\omega = \omega_r$ is pure real. If for a certain value of ω_r , k_i becomes negative, then the profile is said to be convectively unstable, and small disturbances will grow in space in the downstream direction, but can decay at a fixed point at large times.

As may be deduced from equation (11), temporal stability analysis may be easier than spatial stability. Gaster (1962) derived an efficient transformation from temporally to spatially growing modes, which simplifies the spatial stability analysis. To every temporal mode $(\omega_r + i\omega_i, k_r)$, there exists a corresponding spatial mode $(\omega_r, k_r - i\omega_i/c_g)$, where $c_g = \frac{\partial \omega_r}{\partial k_r}$ is the group velocity. A schematic illustration of convective and absolute instability is given in Figure 1.2.

A number of necessary or sufficient conditions for each type of instability can be derived from either the Orr-Sommerfeld equation or from its inviscid form, the Rayleigh equation, which may be appropriate for free shear flows (e.g. shear layers and wakes). For instance, one can show for the inviscid case, that the existence of an inflection point in the velocity profile is a necessary condition for absolute instability (Drazin and Reid 1981). Near wakes

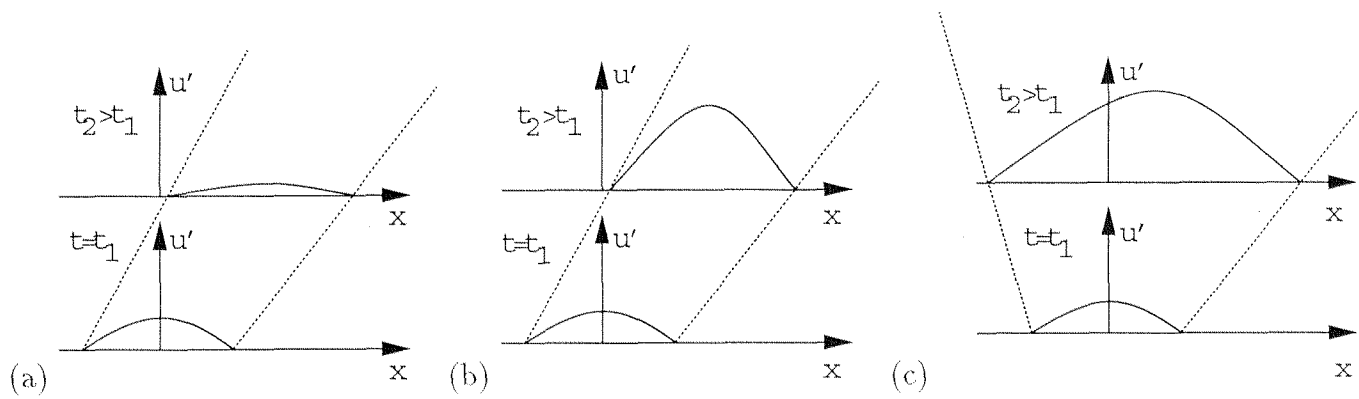


Figure 1.2: Sketch of spatio-temporal evolution of a perturbation u' in a parallel flow, in the cases of (a) linearly stable, (b) convectively unstable, and (c) absolutely unstable flow. Flow direction: left to right.

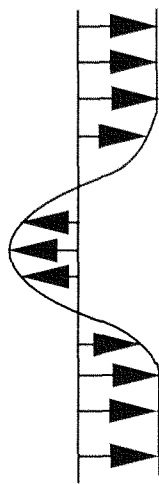


Figure 1.3: Sketch of a typical near wake velocity profile.

are characterized by a finite region of back flow, and thus inflection points exist in the velocity profiles (see Figure 1.3). Therefore, wake flows are good candidates for absolute instability. Koch (1985) showed evidence of the existence of the two types of local instability in wakes and the strong influence of the near wake instability on the instability of the global flow. It is now recognized that wake profiles are absolutely unstable from the bluff body base until slightly downstream the recirculation zone (thus global instability is expected to depend on the recirculation zone length), and become convectively unstable in region farther downstream.

It is reasonable to expect that local and global instability are related. In particular, attempts for finding a condition for the existence of global instability, or a criteria for the selection of the unique shedding-frequency in wakes using local stability analysis has been an important topic in stability research. We might cite, among many others, the pioneering work of Koch (1985), and the subsequent contributions of Monkewitz and Nguyen (1987), Hannemann and Oertel (1989), Triantafyllou et al. (1986), Karniadakis and Triantafyllou (1989), and Chomaz et al. (1988, 1990, 1991).

Chomaz et al. (1988) suggested that the existence of a region of local absolute instability in the wake is a necessary but not a sufficient condition to turn the base flow globally unstable. Chomaz et al. (1990) proposed a qualitative criterion for the existence of oscillatory global modes in a spatially developing flow, which depends only on the absolutely unstable region:

$$\int_{X_a}^{X_b} \sqrt{\omega_{0i}(x)} dx \geq O(1), \quad (13)$$

where $\omega_{0i}(x)$ denotes the local linear temporal growth rate of the modes which have zero group velocity, and $[X_a, X_b]$ is the streamwise extent of absolute instability. This formula shows that a ‘global intensity’ of absolute instability can be defined as the square root of the local growth rate integrated over the length of the absolutely unstable region; this quantity must exceed a certain threshold to excite unstable global modes. This assertion and the presence of absolutely unstable profiles in the near wake confirms the possible implication of local instability on the global flow instability.

Many propositions have also been made to determine the linear and the non-linear global frequency, based on local unstable frequencies. Hammond and Redekopp (1997a) concluded that the criterion proposed by Chomaz et al. (1991) gives most accurate results. This is based on simulation data, for the same flow setup as in the experiments of Leu and Ho

(2000), where the stability of a planar wake subject to steady base suction is investigated. Chomaz et al. (1991) showed that the frequency of a linear unstable global mode can be accurately determined by the imaginary part of the absolute frequency ω at the saddle point at the streamwise coordinate X_s :

$$\frac{d\omega}{dX} \Big|_{X_s} = 0 \quad (14)$$

Since in general the first derivatives of ω_r and ω_i do not vanish at the same streamwise location, the saddle point does not lie on the real x-axis, but at a complex coordinate $X_s = X_{s,r} + iX_{s,i}$, obtainable through analytic continuation methods. This frequency selection criterion, which is very accurate in a nearly parallel flow, becomes deficient in spatially developing flows, i.e. when the assumption of weak deviation from parallel flow is no longer applicable. This issue has been investigated by Monkewitz et al. (1993), who proposed a correction term for the global frequency, for both doubly-infinite and semi-infinite flow domains. Their results were successfully applied in the work of Leu and Ho (2000).

1.3 Flow control: motivation and applications

Flow control can be defined as the action of manipulating a flow in order to obtain a beneficial change. From control theory terminology, the manipulation of the flow is performed via an ‘actuator’, whose action is defined by a ‘controller’, and the beneficial change is the ‘control goal’. One distinguishes between the ‘feedforward’ and ‘feedback’ control strategy (respectively ‘passive’ and ‘active’ in flow control terminology). In the former category, the action of the actuator is predefined, and does not depend on the current state of the system under control. In the second category, the state of the system is taken into account through a measurement signal (provided by a ‘sensor’), which is fed back to the controller. Based on the information contained in the measurement signal, the actuator signal is updated adequately by the controller to approach a given control goal. Passive flow control has been applied already in the prehistoric times, with for instance the manufacture of boomerangs; feedback flow control strategies appeared much later! The primary motivation in modern flow control lies in the enormous financial savings that can be achieved, for example in the case of drag reduction in aircrafts. Other important reasons include pollution control in reactive flows, and issues of safety and product quality. Typical flow control tasks include transition advance

or delay, turbulence enhancement or suppression, and separation prevention or provocation. In many cases, the control strategy used has undesired secondary effects (like drag increase with turbulence enhancement), thus the final goal of flow control consists in an optimization task, i.e. achieving the desired effect while minimizing negative effects.

Flow control studies related to vortex shedding originated a few decades ago. It is well known that the vortex shedding forming behind an immersed body can cause structure damage through the oscillations of the flow, increase drag and noise, although it can have advantageous effects, such as enhancement of mixing and heat or mass transfer. All these issues are also relevant in applications more complex than the simple case of circular cylinder considered here. Since the experiments of Roshko (1955), who, by placing a splitter plate in the near wake of a cylinder, suppressed vortex shedding, many experimental and computational studies have been performed in order to control wake flows at supercritical Reynolds numbers ($Re > Re_{2D,cr}$). The most common approach has been for long time the approach of passive control, by means of endplates (Nishioka and Sato 1978, Stansby 1974), splitter plates (Gerrard 1966, Apelt et al. 1973, Apelt and West 1975), wake heating (Schumm et al. 1994), base bleed or suction (Wood 1964, Wong 1985, Schumm et al. 1994, Hammond and Redekopp 1997a 1997b, Leu and Ho 2000), a thin cylinder placed in the near wake (Strykowski and Sreenivasan 1990), cylinder rotations (Taneda 1978, Tokumaru and Dimotakis 1991), and the use of magnetic fields (Mutschke et al. 1997). Berger (1964, 1967) first implemented a feedback controller for the circular cylinder wake using cylinder transverse oscillations. Supported by Berger's findings, Monkewitz (1989) performed an analytical study on the efficiency of feedback control in global flow stabilization, and concluded that the suppression of self-sustained oscillations like vortex shedding might be possible only over a small range in Reynolds number. This is due to the fact that the high level of feedback control energy input necessary to stabilize the dominant global mode at higher Reynolds number would destabilize higher stable modes. Roussopoulos (1993) confirmed this theory by stabilizing the circular cylinder wake up to $Re=1.2Re_{2D,cr}$, using feedback control with loudspeakers. Since then, other feedback control strategies have been explored (Park et al. 1994, Gillies 1998, Min and Choi 1999), whereby in the last reference, a suboptimal feedback control to suppress vortex shedding was successfully applied up to $Re=160$, i.e. $3.4Re_{2D,cr}$, well above the critical Reynolds number.

Interestingly enough, the numerical simulations of Hammond and Redekopp (1997a,b)

showed that, in the case of an asymmetric wake set-up consisting of two parallel streams of different ambient velocities passing over a forebody with a rectangular trailing edge, base suction can result in simultaneous suppression of unsteadiness and flow vectoring, i.e. deflection of the low-speed stream towards the high-speed stream. Flow vectoring has attractive properties, such as vehicle maneuverability enhancement. A thorough review and classification of aerodynamic and hydrodynamic means to suppress vortex shedding was given two decades ago by Zdravkovich (1981).

As several of the flow control studies cited above, the present work is motivated by the basic stability properties of wake flows. Since global stability is strongly affected by the local stability properties in the region right behind the bluff-body, one may devise a control strategy consisting in the proper modification of the near wake velocity profiles. This is why control actuators are commonly placed in the near wake region. In the case of wake flows controlled by suction or blowing, one can interpret the flow's global stability state by considering the modification of the near wake profiles and its implications on the flow's global stability properties. The suction applied (e.g. at the cylinder base) tends to decrease the length of the recirculation zone (back flow), and thus decreases the streamwise extent of absolute instability. On the other hand, suction also increases the magnitude of negative velocities which acts in favor of instability, as it increases local temporal growth rates. Hence, recalling the qualitative criterion of Chomaz et al. (1990), the effect of suction on the wake is twofold: it increases the local linear growth rates in the near wake but decreases the streamwise extent of absolute instability. Note that blowing has exactly the opposite effects of suction: linear temporal growth rates in the near wake are expected to decrease, due to the decreased back flow; however, the extent of absolute instability is expected to increase. Therefore, in both cases, one has to rely on phenomenological observations to determine which action prevails for a given combination of the problem parameters. These competing effects due to suction or blowing require detailed investigation and have motivated the control studies of cylinder wake in the two-dimensional flow regime presented in this work. Our primary objective is to investigate the effects of base bleed and suction on the stability properties and dynamics of the circular cylinder wake in the two-dimensional regime, using numerical simulation and stability analysis.

The thesis is organized as follows: in chapter (2), we define the problem investigated and present the governing equations and the numerical methodology used to solve them. In chapter (3), we present some tests performed on the controlled and uncontrolled flow to validate the computer code and the computational grids used. In chapter (4), we present the numerical simulation results of the flow under control, and discuss the flow properties in the different flow regimes. In chapter (5), we present in detail the effects of the computational domain size on the flow dynamics, as well as the effects of boundary conditions. In chapter (6), we present the results of global stability analysis and relate them to numerical simulation results. Finally, in chapter (7), we summarize the primary conclusions of the present work.

Seite Leer /
Blank leaf

Chapter 2

Problem definition

2.1 Basic flow setup

We consider an infinitely long circular cylinder of diameter D immersed in a uniform cross-flow of a Newtonian fluid, with free stream velocity U_∞ . A steady fluid suction or blowing flow rate is imposed along a control arc of angle $2\theta_0=45^\circ$, symmetrically placed in the central part of the cylinder base (see Figure 2.1). A similar flow set-up has been used in the experimental work of Schumm et al. (1994), with $2\theta_0=60^\circ$. The base mass transpiration is perfectly symmetric with respect to the axis parallel to the free stream, on which the cylinder is also centered. This axis of symmetry will here to forth be termed the central axis or centerline. The present study is carried out using Direct Numerical Simulation (DNS); the details of control implementation are given together with the governing equations and boundary conditions, in the following section.

2.2 Problem formulation

The present flow problem is fully described by the incompressible Navier-Stokes equations, written here in non-dimensional form:

$$\frac{\partial \mathbf{v}}{\partial t} = -(\mathbf{v} \cdot \nabla) \mathbf{v} - \nabla p + \frac{1}{Re} \nabla^2 \mathbf{v} \quad (1a)$$

$$\nabla \cdot \mathbf{v} = 0 \quad (1b)$$

where $\mathbf{v} = (U, V)$ is the velocity vector, and p the static pressure. ‘ ∇ ’ denotes $(\frac{\partial}{\partial x}, \frac{\partial}{\partial y})$, ‘ ∇^2 ’ is the Laplace operator, $\frac{\partial^2}{\partial x^2} + \frac{\partial^2}{\partial y^2}$, and ‘ \cdot ’ denotes the scalar product. All variables are defined

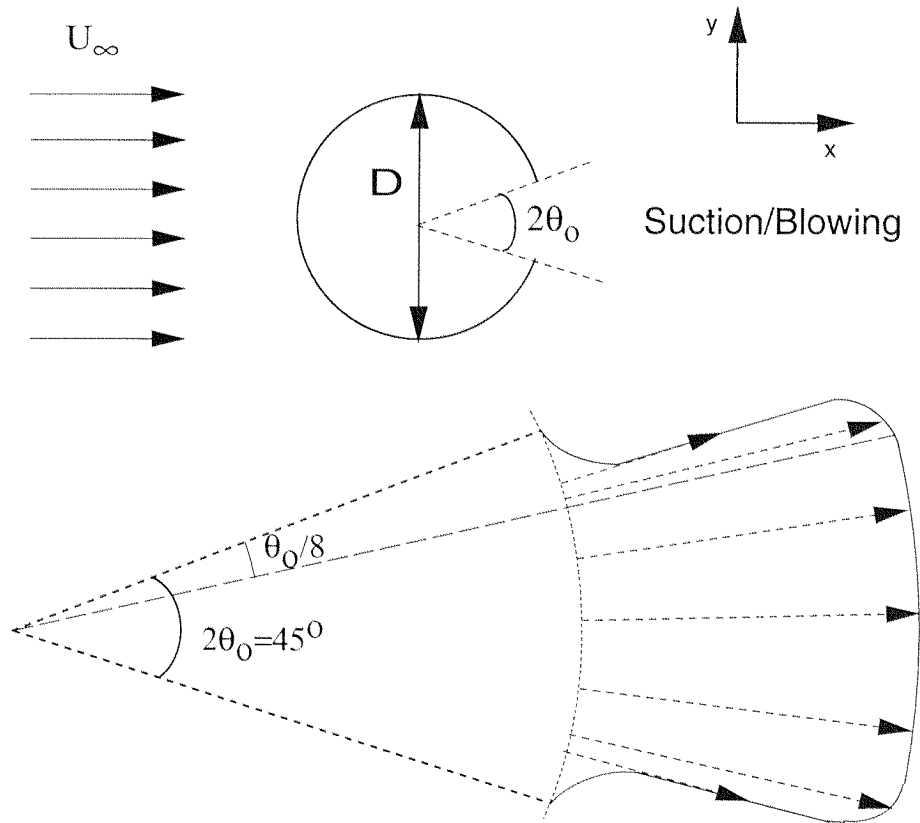


Figure 2.1: Sketch of the flow set-up with control action (here only the blowing case is illustrated).

in a cartesian coordinate system (x, y) , whose origin coincides with the cylinder center. Physical variables (length, time, velocity, and pressure differences) are non-dimensionalized with proper scales, based on the cylinder diameter D , the free stream velocity U_∞ , and the fluid density ρ . The Reynolds number is defined as

$$Re = \frac{U_\infty D}{\nu} \quad (2)$$

where ν is the kinematic viscosity of the fluid.

The system of equations (1a, 1b) is discretized in space and time, and solved within a finite-size computational domain using a spectral element method. The definition of domain size has been a major issue in this work. It is found to have non-negligible effects on the flow behaviour. Detailed results on domain size and external flow boundary effects are reported in a subsequent chapter. Most of the simulations have been performed on the computational domain shown in Figure 2.2. This domain is decomposed into 348 spectral

elements; particularly fine elements are prescribed near the region of control action (see Figure 2.2b), to resolve the high velocity and pressure gradients present. The computational domain extends $30D$ upstream from the cylinder center and $36D$ downstream. The lateral boundaries lie $34D$ away from the central axis; at this distance from the cylinder, and at moderate suction flow rates, the velocity is not affected by the presence of the bluff body, and can therefore be approximated by the free stream velocity. This domain size has been chosen due to the corresponding relatively small number of elements and because it yields reliable results until high enough suction flow rates. It is expected that increasing suction might affect the flow farther from the cylinder. Hence, the results obtained at very high suction flow rates with this domain should not be extrapolated to the infinite flow problem without careful investigation. The effect of suction far away from the cylinder, or inversely, the effect of domain size on flow solutions is the subject of an entire chapter.

Time-histories of velocity and pressure are recorded at five observation points during the simulations. These points are represented on the mesh (Figure 2.2), and their coordinates are given in Table 2.1.

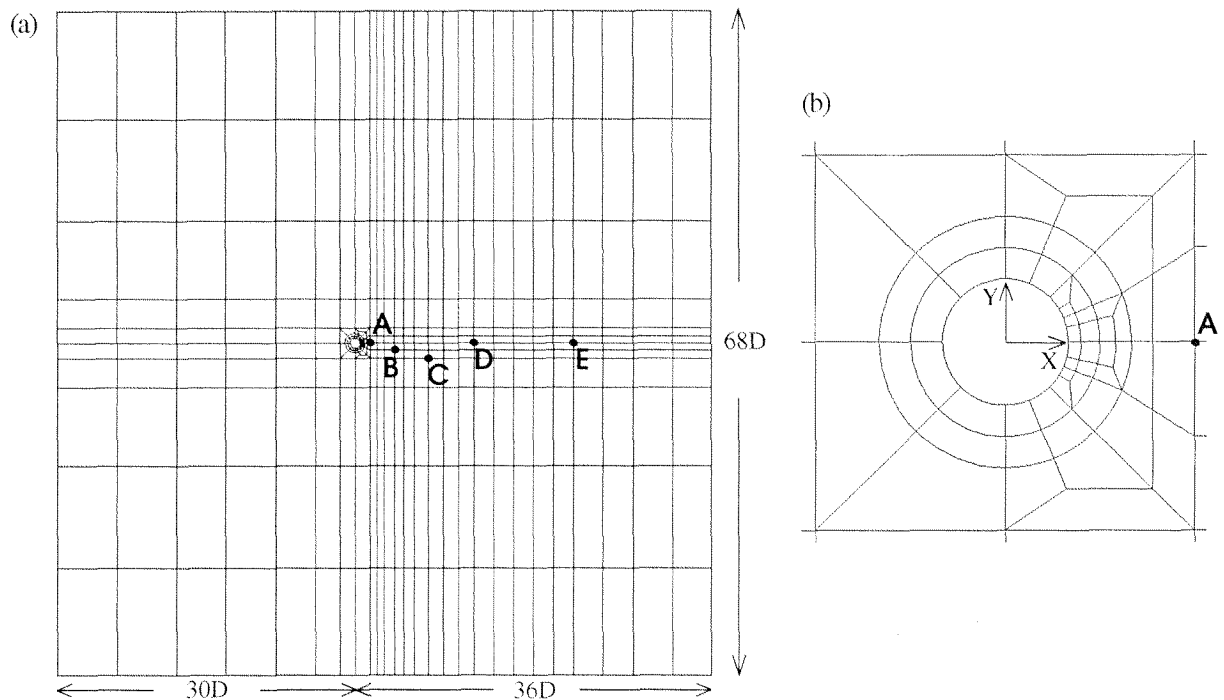


Figure 2.2: Spectral element skeleton used for the flow around a circular cylinder: (a) entire mesh, (b) elements close to the cylinder.

<i>Point</i>	A	B	C	D	E
<i>X</i>	1.50	4.0	7.50	12.0	20.0
<i>Y</i>	0.0	-0.75	-1.50	0.0	0.0

Table 2.1: Coordinates of the observation points.

The following conditions are imposed at the domain boundaries:

at the inflow and lateral boundaries, the velocity is approximated by the free stream:

$$U = 1, V = 0; \quad (3)$$

at the outflow boundary :

$$p = 0, \frac{\partial U}{\partial x} = \frac{\partial V}{\partial x} = 0, \quad (4)$$

velocity boundary conditions at outflow being only imposed in weak form.

A no-slip condition ($U=V=0$) is imposed on the wall part of the cylinder. Since the control action is applied locally, and is not spatially distributed in the entire flow, it appears in the system through a spatial boundary condition, and not in the governing equations. The suction or blowing velocity profile is specified on the cylinder boundary, i.e. on the circle, and the direction of the velocity vectors is radial. A uniform suction or blowing velocity amplitude is imposed on $\frac{\pi}{8}$ of the control arc used, in its central part; a smooth profile (cubic function of the angle, with zero derivatives at the two boundaries) is prescribed close to $\theta=\pm\theta_0$, bringing the velocity to zero at the cylinder wall (Figure 2.1). Based on the prescribed suction volume flow rate Q_{suc} (for unit cylinder length), and a reference flow rate $Q_{ref}=U_\infty D$, we define a suction coefficient as follows :

$$C_{suc} = \frac{Q_{suc}}{Q_{ref}} \quad (5)$$

Here, positive suction coefficient values correspond to suction, and negative values to blowing.

The dynamics of the full system under control depends on two independent parameters: the Reynolds number, Re , and the suction coefficient, C_{suc} .

2.3 Numerical method

The solution of the Navier-Stokes equations with the boundary conditions presented above is based on a spectral element code (Tomboulides 1993). Here, the spatial discretization

is based on a Legendre spectral element method (Patera 1984), while the time integration is based on a second-order accurate mixed stiffly stable scheme, with proper high-order boundary conditions for the pressure (Karniadakis et al. 1991). The numerical method used is briefly reviewed in the next subsections.

2.3.1 Temporal discretization

The time integration of equation (1a) is performed using the combination of a second-order accurate mixed stiffly stable scheme and the ‘splitting’ method, summarized below.

Mixed stiffly stable schemes

In a stiffly stable scheme, the ordinary differential equation

$$\frac{du}{dt} = f \quad (6)$$

is discretized by

$$\frac{\sum_{q=0}^{J-1} \alpha_q (u^{n+1} - u^{n-q})}{\Delta t} = f \quad (7)$$

where superscripts denote discrete time, J is the order of accuracy (in our case $J=2$), and $(\alpha_q)_{(q=0, J-1)}$ is a set of appropriate coefficients.

The mixed treatment of the right hand side term f consists in splitting it into an implicit and an explicit contribution ($f = f_i + f_e$). The explicit part is an extrapolation from previous time steps using a series of coefficients $(\beta_q)_{(q=0, J-1)}$. The final expression for the time discretization takes the form

$$\frac{\sum_{q=0}^{J-1} \alpha_q (u^{n+1} - u^{n-q})}{\Delta t} = f_i + \sum_{q=0}^{J-1} \beta_q f_e^{n-q}. \quad (8)$$

Application to the Navier-Stokes equations with the splitting method

The time integration of the incompressible Navier-Stokes equations is performed in three substeps, using the splitting method. The right hand side of the momentum equation (1a) is expressed explicitly for the convective term, and implicitly for the pressure and viscous terms. The full discretized Navier-Stokes equation takes the form:

$$\frac{\sum_{q=0}^{J-1} \alpha_q (\mathbf{v}^{n+1} - \mathbf{v}^{n-q})}{\Delta t} = - \sum_{q=0}^{J-1} \beta_q [\mathbf{N}(\mathbf{v}^{n-q})] - \nabla p^{n+1} + \nu \nabla^2 \mathbf{v}^{n+1}. \quad (9)$$

In a first step, the non-linear terms $\mathbf{N}(\mathbf{v}) = (\mathbf{v} \cdot \nabla)\mathbf{v}$ are treated, with the introduction of an intermediate variable $\hat{\mathbf{v}}$:

$$\frac{\hat{\mathbf{v}} - \sum_{q=0}^{J-1} \alpha_q \mathbf{v}^{n-q}}{\Delta t} = - \sum_{q=0}^{J-1} \beta_q [\mathbf{N}(\mathbf{v}^{n-q})] \quad (10)$$

For the integration of the pressure part, a second intermediate variable $\hat{\hat{\mathbf{v}}}$ is used, which also obeys the incompressibility condition:

$$\frac{\hat{\hat{\mathbf{v}}} - \hat{\mathbf{v}}}{\Delta t} = -\nabla p^{n+1} \quad (11)$$

$$\nabla \cdot \hat{\hat{\mathbf{v}}} = 0 \quad (12)$$

From the above system, the equation for pressure can be recombined in a Helmholtz equation:

$$\nabla^2 p^{n+1} = \nabla \cdot \left(\frac{\hat{\mathbf{v}}}{\Delta t} \right) \quad (13)$$

and can be solved with the following high-order boundary condition, proposed by Karniadakis et al. (1991):

$$\frac{\partial p^{n+1}}{\partial n} = \mathbf{n} \cdot \left[- \sum_{q=0}^{J-1} \beta_q \mathbf{N}(\mathbf{v}^{n-q}) - \nu \sum_{q=0}^{J-1} \beta_q [\nabla \times (\nabla \times \mathbf{v}^{n-q})] \right] \quad (14)$$

where \mathbf{n} is the unit normal to the boundary $\partial\Omega$ of the computational domain Ω .

In a last step, viscosity contribution and boundary conditions for the velocity are considered to solve \mathbf{v}^{n+1} :

$$\frac{(\sum_{q=0}^{J-1} \alpha_q) \mathbf{v}^{n+1} - \hat{\mathbf{v}}}{\Delta t} = \nu \nabla^2 \mathbf{v}^{n+1} \quad (15a)$$

$$\mathbf{v}^{n+1} = \partial \mathbf{v}^{n+1} \quad \text{on} \quad \partial\Omega. \quad (15b)$$

The decoupled equations for velocity (15a) and pressure (13) are both Helmholtz equations, and can be written in the form:

$$(\nabla^2 - \lambda^2)\phi(x, y) = g(x, y) \quad (16)$$

with ϕ denoting velocity \mathbf{v}^{n+1} or pressure p , where $\lambda=0$ for the pressure equation and $\lambda^2 = \frac{\sum_{q=0}^{J-1} \alpha_q}{\nu \Delta t}$ for the velocity equation. The numerical solution of equation (16) necessitates a spatial discretization, which is carried out using a spectral element method, outlined in the next subsection.

2.3.2 Spatial discretization

In this section, we illustrate the application of the spectral element method to solve the Helmholtz equation (16). In the general two dimensional case, the computational domain Ω is broken up into spectral elements, as illustrated in Figure 2.2. Each element is mapped isoparametrically to the canonical square. The spectral element method is based on the Galerkin variational statement of the equation (16) to be solved, which is written:

$$\int_{\Omega} \nabla \psi \nabla \phi \, dx dy = - \int_{\Omega} \psi g \, dx dy. \quad (17)$$

The test functions ψ belong to the standard Sobolev space H_0^1 with homogeneous boundary condition $\psi=0$. For the spectral element discretization, the variational form (17) is restricted to the discrete space $X_h \subset H_0^1$, relatively to the spectral element discretization parameters (K, N_1, N_2) , where K is the number of elements, N_1 and N_2 are the piecewise high-order polynomial degrees in the directions x and y , respectively local coordinate system. With the selection of appropriate Gauss-Lobatto points ξ_{pq}^k and corresponding weights $\rho_{pq} = \rho_p \rho_q$, the discrete form of equation (17) can be written as:

$$\sum_{k=1}^K \sum_{p=0}^{N_1} \sum_{q=0}^{N_2} \rho_{pq} J_{pq}^k [\nabla \psi \nabla \phi]_{\xi_{pq}^k} = - \sum_{k=1}^K \sum_{p=0}^{N_1} \sum_{q=0}^{N_2} \rho_{pq} J_{pq}^k [\psi g]_{\xi_{pq}^k}, \quad (18)$$

where J_{pq}^k is the Jacobian of the transformation from global to local coordinates $(x, y) \Rightarrow (r, s)$ for the quadrilateral element k . The Jacobian is calculated from the partial derivatives of the geometry transformation. Next, test functions $\psi_{m,n}$ are chosen in terms of Legendre-Lagrangian interpolants, such that $\psi_{m,n}(\xi_{pq}) = \delta_{mp} \delta_{nq}$, where δ is the Kronecker-delta symbol. It has been shown (Patera 1984) that this implementation makes the numerical solution converge spectrally to the exact solution, for a fixed number of elements K , and $N_1, N_2 \rightarrow \infty$. Increasing the polynomial orders N_1, N_2 corresponds to ‘p-refinement’, whereas increasing the number of elements K is the ‘h-refinement’. The test functions, also constituting a basis of X_h , being chosen, the approximation for ϕ^k referred to the element k can be written as:

$$\phi^k(r, s) = \sum_{m=0}^{m=N_1} \sum_{n=0}^{n=N_2} \phi_{mn} \psi_{r,s} \quad (19)$$

where ϕ_{mn}^k is the local nodal value of ϕ . The same basis functions are used to represent geometry:

$$(x, y)^k(r, s) = \sum_{m=0}^{m=N_1} \sum_{n=0}^{n=N_2} (x_{mn}^k, y_{mn}^k) \phi_{mn} \psi_{r,s} \quad (20)$$

where x_{mn}^k, y_{mn}^k are the global physical coordinates of the node mn in the k -th element. Finally, the matrix system corresponding to the discrete form of the Galerkin variational statement (18) takes the form:

$$\sum_{k=1}^K \prime \sum_{m=0}^{N_1} \sum_{m=0}^{N_2} (P_{ijmn}^{x,k} + P_{ijmn}^{y,k}) \phi_{mn}^k = - \sum_{k=1}^K \prime \sum_{m=0}^{N_1} \sum_{m=0}^{N_2} J_{ij}^k B_{im}^k B_{jn}^k g_{mn}^k, \quad (21)$$

where $\sum \prime$ denotes direct stiffness summation for the global system to ensure that the ensemble is performed in space H^1 .

Because of the large sizes of the matrices $P_{mn}^{x,k}$, using a direct solver for the entire system would be much too demanding in terms of CPU memory. Therefore, a direct solver is used for the pressure part only, and an iterative procedure is employed, based on a preconditioned conjugate gradient method (Golub and Van Loan 1983) for the velocity. It was found that convergence in pressure with the iterative solver could be reached at the same accuracy as with the direct solver after a large number of iterations only (one order of magnitude more than for the velocity), thus the direct solver solution has been chosen for the pressure (Tomboulides 1993).

Chapter 3

Resolution and validation tests

In this chapter, we perform several tests, to validate the computer code, as well as resolution tests, to investigate the effect of numerical resolution on the accuracy of results. In general, the quality of results depends on a number of parameters, mainly computational domain size, spatial and temporal resolution, and the tolerance prescribed in the velocity iterative solver. Our initial domain size choice is based on a previous study carried out by Barkley and Henderson (1996). The domain and grid adequacy will be illustrated here only for the uncontrolled system, by comparing our simulation results with literature data. For the system under control, the domain size is in fact a crucial parameter; its effect on the computed flow states results will be reported in detail in another chapter. The influence of all other parameters is studied in this chapter, for the entire range of system parameters of the present work, i.e. $Re \leq 90$ and $C_{suc} \leq 2.6$.

3.1 Basic validation tests

First, we compare results obtained for the uncontrolled flow to literature data. If not otherwise indicated, results reported below have been obtained with a 9×9 elemental resolution, and a time step $\Delta t = 0.01$.

The drag coefficient is an important element in bluff body flows, especially for aerodynamical applications, expressing a non-dimensional form of the force exerted by the fluid on the body, in the streamwise direction. The lift coefficient is the non-dimensional form of the force in the direction normal to the free stream. Here we follow the standard definitions for

the drag (C_D) and the lift (C_L) coefficients found in the literature (Zdravkovich, 1997). In the special case of flow around a circular cylinder, they obtain the form:

$$C_D = \frac{F_X}{\frac{1}{2}\rho U_\infty^2 D} \quad (1)$$

$$C_L = \frac{F_Y}{\frac{1}{2}\rho U_\infty^2 D}, \quad (2)$$

where F_X (resp. F_Y) is the x- (resp. y-) component of the total force per cylinder unit-length exerted by the fluid on the cylinder surface. In Figure 3.1, we present the computed drag coefficient values in the steady flow regime, and the time-averaged values in the unsteady regime, and compare them to the curve fits found by Henderson (1995). The Figure indicates a very good agreement between our computations and Henderson's data.

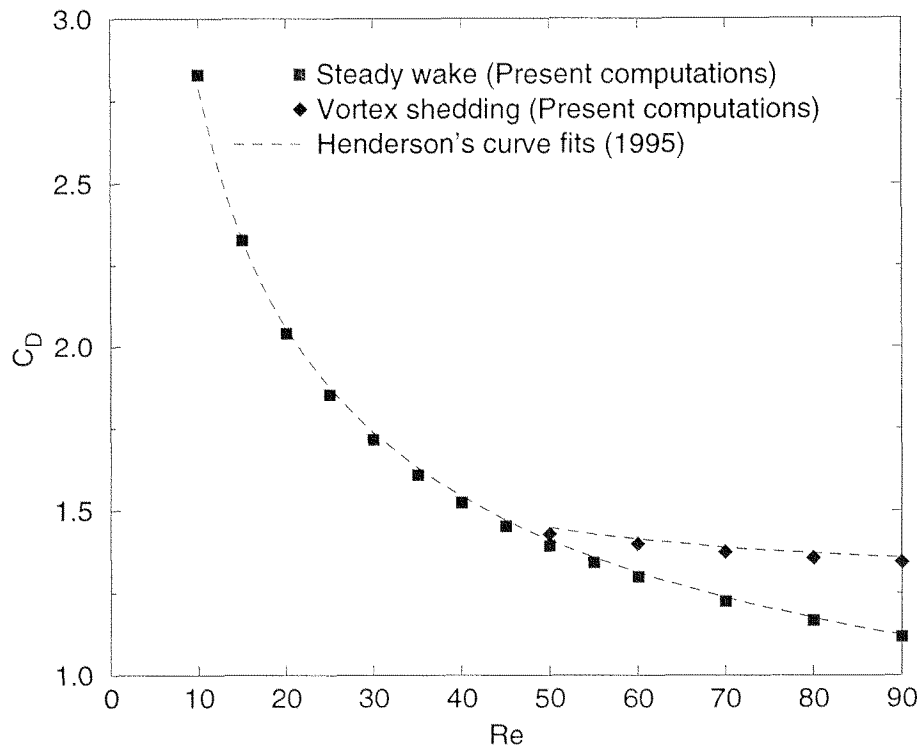


Figure 3.1: Time-averaged total drag coefficient versus Reynolds number (uncontrolled flow).

Another characteristic property of wake flows is the non-dimensional shedding frequency (Strouhal number, St). In the case of the circular cylinder flow, the Strouhal number is

defined as:

$$S_t = \frac{fD}{U_\infty}, \quad (3)$$

where f is the frequency of flow oscillations. In Figure 3.2, we report our computed Strouhal number values versus Reynolds number for the uncontrolled flow, and compare them to the empirical formulas of Roshko (1954), Williamson (1988), Fey et al. (1998) and to the 2-D simulation results of Barkley and Henderson (1996). Good agreement is found between the present results and the literature data.

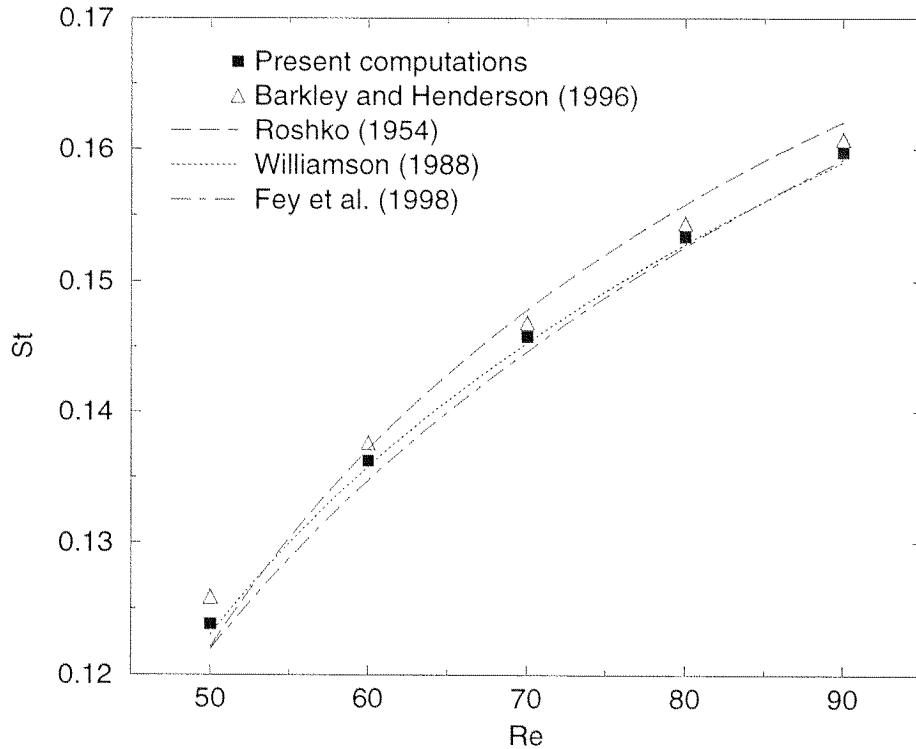


Figure 3.2: Strouhal number versus Reynolds number (uncontrolled flow).

A representative flow feature is the presence of two recirculation zones, extending over a length X_r , from the cylinder base at $(x, y) = (\frac{D}{2}, 0)$ to the stagnation point on the centerline, at $(x, y) = (\frac{D}{2} + X_r, 0)$. The recirculation zone length X_r can be precisely defined for both the steady and the time-averaged fields (in the unsteady regime). Regarding the steady flow solutions, it is well known that X_r is a linearly increasing function of the Reynolds number (also at supercritical values, $Re > 47$). On the other hand, in the vortex shedding regime,

the recirculation length of the time-averaged flow decreases with Reynolds number, because of the action of Reynolds stresses. In Figure 3.3, we present the computed values of the length of recirculation zones versus Reynolds number, corresponding to the solutions of the steady flow equations, and to the time-averaged solutions in the unsteady regime. Since we are solving the time-dependent Navier-Stokes equations, in order to converge to the solution of the steady equations at supercritical Reynolds numbers, we had to solve for half of the computational domain, imposing a symmetry boundary condition ($\frac{\partial U}{\partial y}=0$ and $V=0$) along the centerline.

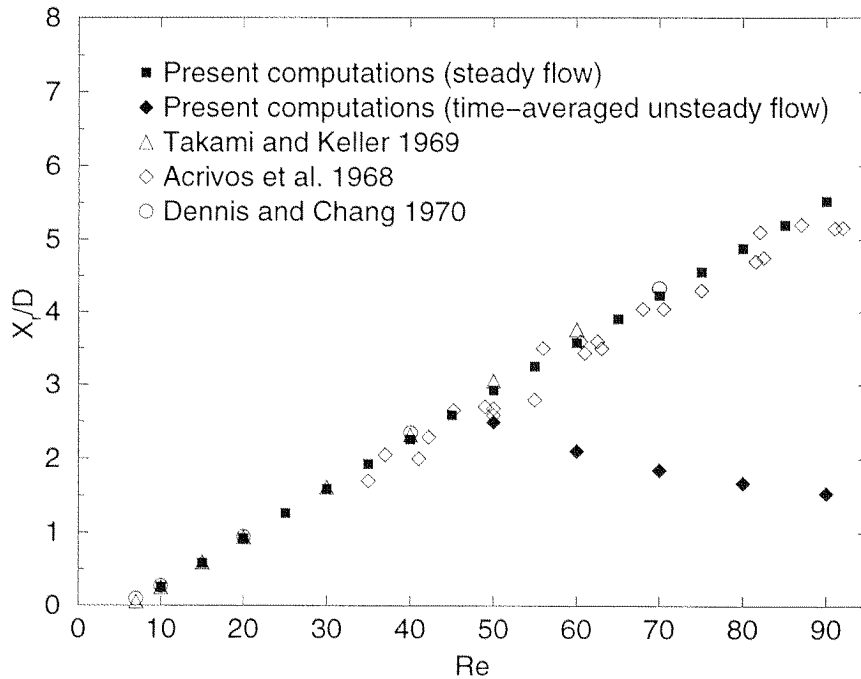


Figure 3.3: Recirculation length, normalized by cylinder diameter, versus Reynolds number (uncontrolled flow).

Our results accurately reproduce the linear dependence of the recirculation length with the Reynolds number, as already shown by Fornberg (1985) for a wide range of Reynolds numbers (Re up to 600). Also, they are in good agreement with the simulation results of Takami and Keller (1969) and Dennis and Chang (1970), and the experimental data of Acrivos et al. (1968). Regarding the time-averaged flows, we observe a decrease in X_r at supercritical Reynolds numbers. This decrease of X_r in the vortex shedding regime is due to

the Reynolds stresses (absent in the steady regime), which increase the momentum transfer through the process of “turbulent” diffusion. The rapid momentum transfer towards the centerline results in shorter recirculation zones, as well as in reduced wake thickness, the wake being limited laterally by the isocontours $U \approx 1$.

The above tests provide confidence in the computer code and basic resolution used, and also indicate the adequacy of computational domain. This is not surprising, as our domain is larger than the one suggested by Barkley and Henderson (1996), which was already optimized for the uncontrolled flow. We use a larger domain, as we expect that the control action affects the flow field farther away from the cylinder surface. This issue will be analyzed in detail in chapter (5).

3.2 Tolerance in velocity iterative solver and system stability

Applying the numerical approach outlined in chapter (2) to a specific problem requires building a numerical grid and specifying a time step value. As already mentioned in section 2.3, an algebraic equation of type $Ax = B$ is solved iteratively for the velocity at each time step, by means of a conjugate gradient method. Convergence depends on the prescribed tolerance level, denoted here by TOL . Compared to a direct method, which consists in inverting directly the system matrix A , yielding $x = A^{-1}B$, an iterative procedure has the advantage of being much less memory consuming, but also presents the drawback of being less accurate and slower. Indeed, a direct method produces a solution vector x with a relative error on each of its components of machine accuracy level (10^{-16} , for a code written in double precision), whereas the iterative method yields a solution with an averaged user-defined accuracy, controlled by TOL . The convergence criterion in the iterative solver is:

$$\frac{1}{N} \|Ax - B\| < TOL, \quad (4)$$

with $\| \cdot \|$ denoting the euclidian norm: $\|x\| = \sqrt{\sum x_i^2}$, and N the rank of the system matrix A . A common tolerance level in the Helmholtz solver is of single precision order, i.e. 10^{-8} . An initial guess x_0 for the solution at each new time step is also necessary. The most natural choice for x_0 is the converged solution of the previous time step. Therefore, if the time variation of the flow ever becomes extremely slow, it is possible that the condition

$\frac{1}{N} \|Ax - B\| < TOL$ is already verified at the first iteration of the iterative solver, which would result in a strictly saturated steady state. This scenario is practically impossible with a direct solver: the probability of the solutions to two distinct systems of algebraic equations being equal (even at machine accuracy level) is zero. In some cases discussed in detail in the next subsection, an unphysical saturation to steady flow is indeed computed. The problem can be overcome by decreasing the prescribed ‘*TOL*’ value, which naturally increases the CPU costs.

3.2.1 Instability suppression due to numerics

We begin our investigation of the effects of tolerance level in the velocity iterative solver on the computed flow states, by considering the development of global mode at supercritical Reynolds numbers (here $C_{suc} = 0$). In a first attempt, the steady flow solution (obtained with half the computational domain and a symmetry boundary condition on the centerline) is used as initial condition. Thus, regarding the flow development in the full domain, the initial perturbations are due to numerical errors only, and are thus of very low level. In the initial test runs, we prescribe a tolerance value $TOL = 10^{-8}$. We find that, for Reynolds numbers up to 90, after a short chaotic transient, the global mode starts growing exponentially in time, however, after a number of time units, oscillations stop abruptly, and a saturated time-independent flow state is reached! This behaviour is typically represented in signals as those in Figure 3.4, where we plot the time-history of the V-velocity offset from the steady (initial) values at $Re=70$, at points A, D, E, as the flow evolves from the base steady solution. Here, some induced initial random perturbations rapidly evolve into the least stable eigenmode (in less than 30 time units), which then starts growing exponentially. However, after approximately 50 time units, all oscillations stop, and the solution ‘freezes’ in time.

To further explore the issue, we test the effect of several variations in the prescribed tolerance level, described in the next subsection.

3.2.2 Instability triggered by a jump in the system parameter

An important test in calibrating numerical parameters is the confirmation of the critical Reynolds number value. No definitive conclusion has been arrived at in the previous subsection, since numerical errors were not amplified up to $Re=70$, which is well above the critical

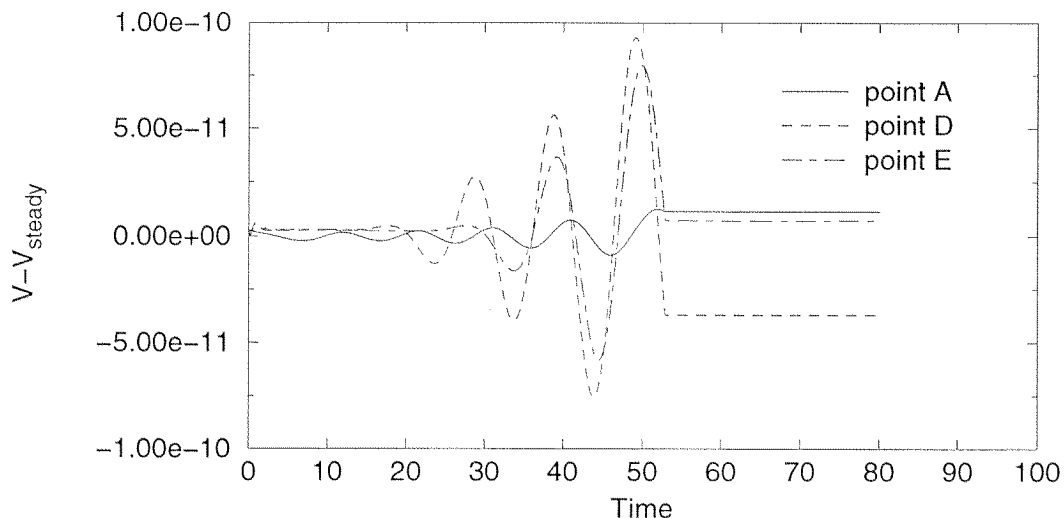


Figure 3.4: Time-history of V-velocity offset at points A, D and E, for $Re=70$, $C_{suc}=0$. The initial condition is the steady symmetric solution.

value $Re=47$.

A more promising procedure in triggering global instability consists in disturbing the steady flow solution with small physical (and not numerical) perturbations. For example, a discontinuous increase in Reynolds number produces a perturbation field in the entire domain, and is thus expected to disturb sufficiently the steady solution and lead to unsteadiness for $Re \geq 50$. We have proceeded as follows: starting from the steady solution at $Re=40$, we have increased the Reynolds number stepwise by an increment of 5, and computed the flow transient to the new saturated state. The process is iterated (Re further increased by a step of 5) until perturbations caused by the Re jumps are self-amplified and lead to sustained unsteadiness. Since the discontinuous increase in Reynolds number corresponds to finite global perturbations, one could expect amplification of the global mode for Reynolds numbers as low as $Re = 50$. Instead, with $TOL = 10^{-8}$, unsteady flow was first obtained at $Re=60$. In Figure 3.5, we plot the time histories of U- and V-velocity at point A during the above numerical experiment, indicating the saturation to steady flow for Reynolds numbers lower than 60. The initial exponential increase of V-velocity fluctuations at $Re=55$, and the subsequent saturation to a steady value, apparently due to the effect of tolerance in the velocity iterative solver is clearly illustrated.

Interestingly, at $Re=60$, at which the wake becomes unsteady (in this experiment), the

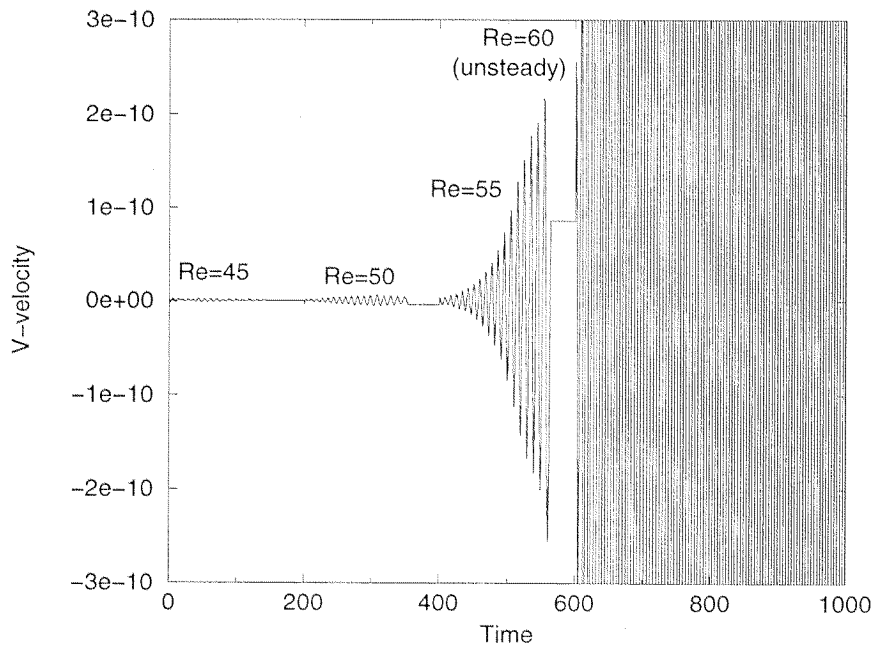
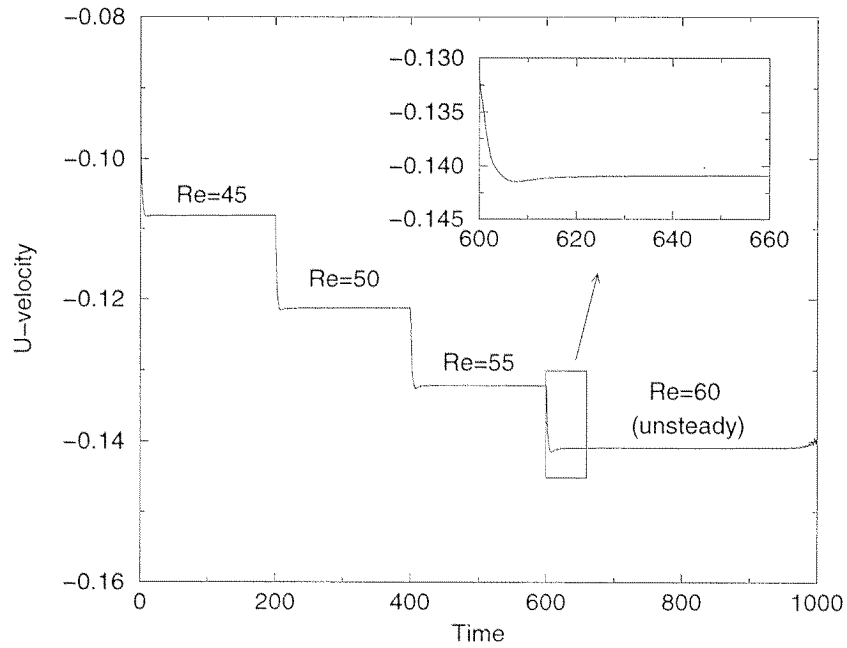


Figure 3.5: Time-history of U- and V-velocity at point A. $Re=45$ at $t=0$, Re is increased by an increment of 5 every 200 time steps. $TOL = 10^{-8}$.

transient U-velocity signal at early times is similar to those obtained at smaller Reynolds numbers: it tends initially and within a very short time scale to the steady solution value. After large times, the unstable mode can be observed, and the flow tends asymptotically to a limit cycle.

We focus now on the transient signal at $Re=60$, and attempt to interpret its different parts by considering the different factors that influence the system. Within about the first 60 time units after the jump of Re from 55 to 60, the flow has reached its new quasi-steady state in its upstream region (see Figure 3.5, U-velocity plot). This initial behaviour is not surprising, as the initial state of the system (steady solution at $Re=55$) has no fundamental differences in structure, compared to the new base flow, and because the growth of perturbations is rather slow at this low Reynolds number. The system is driven by two different physical processes, diffusion and convection, characterized by different time scales, τ_D and τ_C , respectively. The diffusion time scale is typically of order $\tau_D \approx \frac{D^2}{\nu}$, and the convective time scale of order $\tau_C \approx \frac{D}{U_\infty}$. In non-dimensional form, these time scales are respectively of order Re , and 1.0. At $Re=60$, the fastest process is therefore the convection. The time needed for the system to reequilibrate at a new quasi-steady state after initial perturbations (here caused by the Re jump), is given by the slowest process, i.e. diffusion. At $Re=60$, diffusion will equilibrate after the order of 60 time units, which can be well verified by the framed zoom in the U-velocity plot of Figure 3.5. The long time gap that follows the initial transient of about 60 time units (during which the new quasi steady state is reached), and precedes the visible growth of oscillations, results from the combination of various factors. At $Re=60$, perturbations are indeed expected to grow exponentially, but only when their spatial structure becomes close enough to the structure of the unstable eigenmode. Before being able to grow, the perturbation field must therefore rearrange itself into the global eigenmode, which might take a non-negligible time if its initial shape differs significantly from the eigenmode. This seems to be the case here: the initial perturbation field is related to the difference between the base flows at $Re=55$ and $Re=60$, and should not be structurally close to the unstable mode at $Re=60$. The time needed for the perturbation field to get the shape of the unstable mode is longer than the corresponding characteristic time of diffusion. As the perturbation field starts growing exponentially, the perturbations level is therefore very low, thus it will take a long time to become visible. Furthermore, the growth rate of disturbances at $Re=60$ is also small; Provansal et al. (1987) proposed the following relation between the temporal

growth rate and the Reynolds number for the circular cylinder wake at slightly supercritical Reynolds numbers:

$$\sigma_r = \frac{(Re - Re_{2D,cr})\nu}{5D^2}. \quad (5)$$

This formula yields a non-dimensional growth rate value of 0.043 at $Re=60$. Considering an initial perturbation level of the order of 10^{-8} , about 350 time units are necessary to multiply it by a factor of order 10^6 , which would bring it to a level of 10^{-2} , and make it visible. This corresponds to the gap of time during which the signal remains at a quasi steady state, and the oscillations at an invisible level (see U-velocity plot in Figure 3.5).

We now investigate the effect of prescribed tolerance in the velocity iterative solver. To this end, we focus on the plot of the V-velocity at point A. This enables a ‘clean’ observation of the unstable mode growth, since the steady state value (zero) of the V-velocity at point A is not affected by the consecutive jumps in Re . As can be seen in Figure 3.5 (V-plot), initial perturbations caused by the Re jumps are rapidly damped at the subcritical Reynolds number only ($Re=45$), whereas at $Re = 50$ and $Re = 55$ they grow exponentially until they abruptly saturate at a non-zero value. This behaviour is clearly unphysical, and caused by numerical factors, in particular the effect of the tolerance level in the velocity iterative solver. At a supercritical Reynolds number, e.g. $Re=50$, the expected physical U-velocity transient at point A would consist of three parts: the first two parts are present in Figure 3.5, and correspond to the fast initial convergence to the new steady solution, and a rather long time interval during which the flow remains at a quasi steady state. The third part, expected but missing in Figure 3.5, would be the growth of oscillations until a non-linear periodic state is reached. The sudden termination of exponential growth (see Figure 3.5) can only be attributed to the velocity iterative solver: due to the low level of perturbations in the entire flow field, the condition $\frac{1}{N}\|Ax - B\| < TOL$ already holds at a first solver iteration, and continues to be valid in the subsequent time steps.

To investigate more thoroughly the contribution of TOL and time step Δt on the computed stability states, we carried out flow simulations at $Re=50$ with three different TOL values ($TOL = 10^{-10}$, 10^{-14} and 10^{-16}) and four different time step values ($\Delta t=0.02$, 0.01 , 0.005 and 0.001), with the saturated steady flow field at $Re=45$ used as initial condition. Time histories of the corresponding V-velocity at point A are plotted in Figure 3.6. Some signals (at $TOL=10^{-14}$ and $TOL=10^{-16}$) are not drawn over the time range, because they tend asymptotically to a limit cycle, and their representation up to large times would hide the

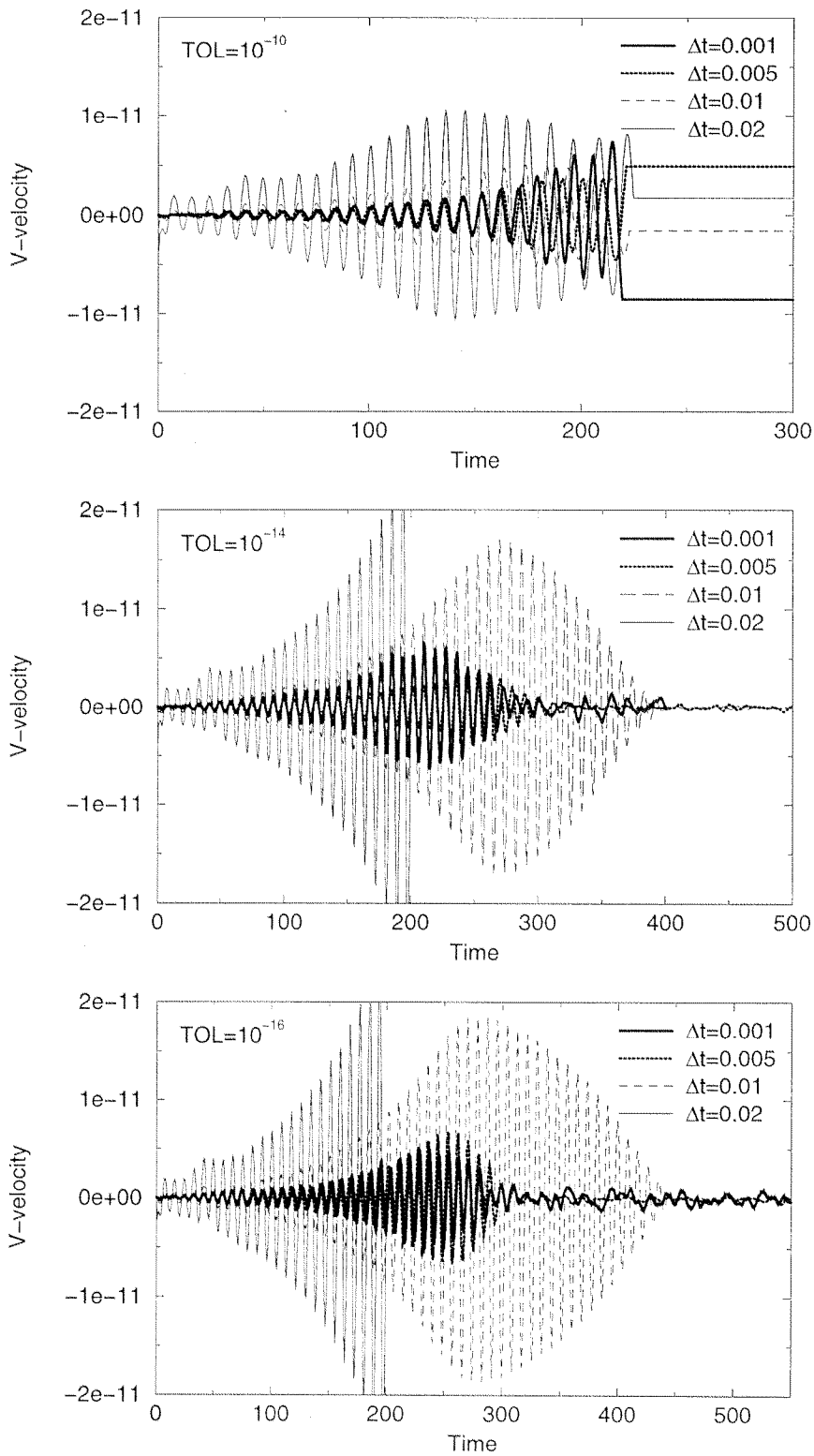


Figure 3.6: Transient signals of V-velocity at point A, illustrating the effect of time step (Δt) and tolerance (TOL) in the velocity iterative solver on global mode evolution. Here $Re=50$, while the initial condition is the steady field at $Re=45$.

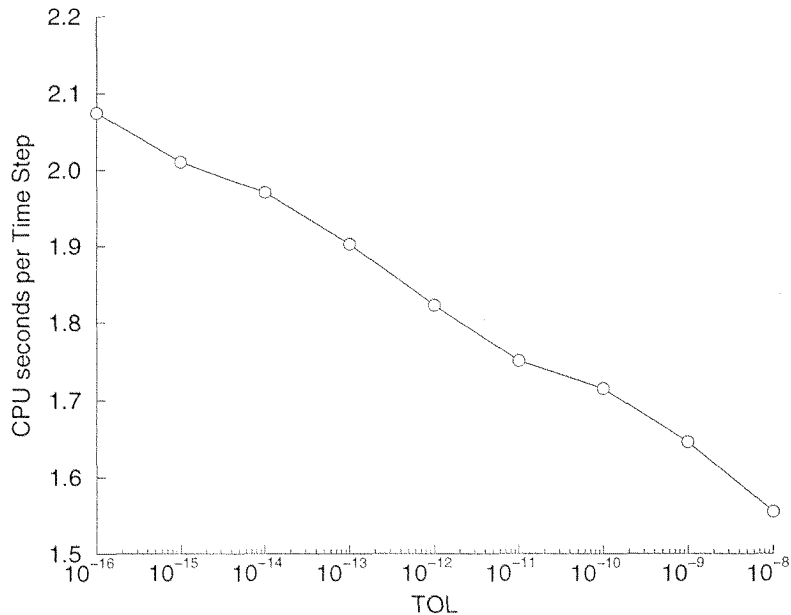


Figure 3.7: CPU seconds per time step, versus TOL value. $Re=80$, $C_{suc}=0.90$, 9×9 resolution.

other signals. Growth of the unstable eigenmode could be obtained for only $TOL \leq 10^{-14}$, although not for all time step values tested here. Interestingly enough, we find that at a given TOL value, instability growth is better predicted with large time step values. This can be attributed to the effective enhancement of perturbations by the larger temporal discretization errors, thus exceeding a threshold level to trigger global instability. At lower Δt values, the initial effective perturbation levels remain small at early times, being less enhanced by errors due to time discretization. This may inhibit the formation and growth of an unstable global mode. Thus, larger time steps are preferable, in terms of triggering the global mode.

We conclude that, to investigate the flow stability near the critical parameter value using DNS, one must not only impose a sufficiently strong initial perturbation on the steady flow field, but also decrease the tolerance value to very low levels, of machine accuracy order ($O(10^{-16})$). We expect that spatial resolution similarly affects flow stability. Since the onset of instability also depends on time step value, which may in turn depend on spatial resolution (due to the numerical stability constraints), it is not straightforward to study the effect of spatial resolution, independently of other numerical parameters, as time step. We

can, however, reasonably affirm that, as for time step, lower resolution introduces higher numerical errors and therefore higher perturbation levels to the steady base flow, which acts in the favor of instability growth. Thus the accuracy won by increasing spatial resolution may be a drawback in terms of tracking global instability growth. This confirms the assertion that the only measure for increasing the system sensitivity to small perturbations, without decreasing numerical accuracy, is to decrease the tolerance value TOL . In our simulations, we have used $TOL = 10^{-8}$ to compute flows evolving far enough from steady regimes. Flows evolving in the neighborhood of a steady state have been treated with $TOL = 10^{-14}$. The CPU time per time step is thereby increased by 27%. In Figure 3.7, we present some representative CPU times per time step versus the TOL value. These data were calculated from simulations performed on the limit cycle at $Re=80$, $C_{suc}=0.9$, on a HP Convex Exemplar SPP2000/X-32 machine, and the CPU times have been averaged over 100 time steps.

3.3 Spatial and temporal resolution tests

Spatial and temporal resolution are typical numerical factors affecting the quality of results. Having validated the computational domain for the uncontrolled flow, and the tolerance value in the velocity iterative solver, we also performed spatial resolution (p-refinement, i.e. increase of the order in polynomial expansions) and temporal resolution tests for the flow under control action. Results from the spatial resolution tests are reported in Table 3.1, for seven representative parameter sets. Here, we compare values of two global flow quantities, the non-dimensional shedding frequency and the time-averaged drag coefficient. We find that flows corresponding to parameter sets far from transitions (see the map of flow regimes, in next chapter) and at rather low suction coefficient values are typically well resolved using 7×7 elemental resolution. However, flows corresponding to parameter sets near critical lines or at high suction coefficients values ($C_{suc} > 1.0$) require 9×9 elemental resolution (for which discrepancies in Strouhal number and mean drag coefficient with 11×11 elemental resolution simulations fall below 2%). In all test runs, the time step is chosen small enough not to affect the computed fields. As will be shown, the time step value has practically no effect on the simulation results, except for flows evolving from a quasi steady state (see previous section); in this case the primary parameter to adapt in order to get physically correct results is the TOL value.

To check for temporal resolution, we have performed a number of tests at several time steps and system parameter values. Concerning saturated limit cycles, different Δt values result in practically indistinguishable signals. This is not surprising, as the large values of fluctuation intensities in a saturated limit cycle, accompanied by small Δt values and overall second order accuracy in time, result in negligible levels of relative error. To check for levels of relative error for cases with small fluctuation intensities, we have performed simulations corresponding to the growth of the global mode at four parameter sets, namely $(Re=30, C_{suc}=0.9)$, $(Re=50, C_{suc}=1.5)$, $(Re=90, C_{suc}=-0.1)$, and $(Re=90, C_{suc}=0.9)$. For each parameter set, two different values of Δt and two different elemental resolutions are used, in order to investigate the effect of Δt at different spatial resolutions. In each case, two different types of initial conditions are considered: the first is the steady field computed at the same Re - and C_{suc} - values and the same resolution. The second type of initial condition is obtained as follows: the base steady solution is obtained with low (5×5) elemental resolution; subsequently, a simulation is performed on the full flow domain, in order to obtain the initial stage of the global mode growth, and perturbations of single precision order. The resulting flow field was used as initial condition for the simulations with the various time steps and spatial resolutions. Simulations have been carried out with a very small TOL value, $TOL = 10^{-16}$, so that convergence in the iterative solver is not an additional factor affecting computations.

Results are plotted in Appendix A. For each parameter set, we display two separate figures, one for each elemental resolution. On each figure, we show the V-velocity at point A, indicating: (a) the growth of the global mode from the slightly disturbed steady solution to its non-linear saturated state, with a zoom on the linear and non-linear states; and (b) the initial growth of the global mode from the steady solution. When the slightly disturbed steady flow is used as initial condition, simulations with different time steps result in practically identical signals at the observation points, from the linear to non-linear states. This proves the adequacy of temporal resolution for the entire range of simulations performed in the present study. The differences in time histories when the strictly steady flow is used as initial condition can be explained by the fact that machine round-off and temporal discretization errors are of the same order (double precision simulation). From Figures (b), we can also identify the rearrangement of initial disturbances (caused by discretization errors) into the dominant eigenmode (unstable frequency). The effect of time resolution is

Re	C_{suc}	Resolution	Δt	St	C_D
20	1.60	7×7	0.001	0.0187	17.38
20	1.60	9×9	0.001	0.0187	17.21
20	1.60	11×11	0.001	0.0188	17.18
50	0.40	7×7	0.01	0.1029	2.81
50	0.40	9×9	0.01	0.1038	2.78
50	0.40	11×11	0.01	0.1039	2.78
50	1.00	7×7	0.001	0.0195	8.57
50	1.00	9×9	0.001	0.0196	8.46
50	1.00	11×11	0.001	0.0196	8.43
50	1.30	7×7	0.001	steady	11.9
50	1.30	9×9	0.001	steady	11.7
50	1.30	11×11	0.001	steady	11.6
80	0.80	7×7	0.001	0.0176	6.37
80	0.80	9×9	0.001	0.0171	6.32
80	0.80	11×11	0.001	0.0169	6.30
90	0.85	7×7	0.001	0.0105	6.35
90	0.85	9×9	0.001	0.00935	6.32
90	0.85	11×11	0.001	0.00958	6.26
90	1.80	7×7	0.0009	steady	22.72
90	1.80	9×9	0.0007	steady	22.20
90	1.80	11×11	0.0006	steady	21.80

Table 3.1: Spatial resolution tests: Strouhal number and drag coefficient values corresponding to seven parameter sets.

in all cases negligible, since it does not affect the basic flow state and its properties (St , C_D , etc) both in the linear and non-linear states (again for parameters choices not too close to transition points). In terms of discrepancies in time-asymptotic states, these are also kept at very low level. For example, in the case presented in Figure A.4(a) ($Re=50$, $C_{suc}=1.50$), the relative difference in asymptotic V-velocity values, after transients of 1500 time units, is about 10^{-4} .

In summary, spatial resolution tests have shown that a 9×9 elemental resolution yields accurate results for a wide range of the system parameters. Thus, for consistency, we will only report simulation results obtained with 9×9 elemental resolution. For the range of Δt values required to fulfill the numerical stability constraint, temporal resolution has practically no effect on results. The maximum Δt value used in the present work is 0.02 (used for uncontrolled flow cases).

3.4 Validation with the Stuart-Landau model

As has been shown by several experimental (Mathis et al. 1984, Provansal et al. 1987), and numerical and theoretical studies (Jackson 1987, Důšek et al. 1994, Noack and Eckelmann 1994), the von Kármán vortex street is a direct consequence of a supercritical Hopf bifurcation. This type of bifurcation is characterized by the continuous growth of an unstable global mode towards a limit cycle, at supercritical system parameter (here the Reynolds number). At slightly supercritical Reynolds number, the time variation of small disturbances superimposed on the steady solution can be divided into three parts. First, disturbances arrange themselves into the most unstable mode, whereby all but one discrete frequencies are being damped. In general, this initial step lasts for a short time, compared to the next step, where the dominant eigenmode, or unstable ‘global mode’ grows exponentially, at a rate referred to as the ‘global’ growth rate. The exponential growth of disturbances can be observed as long as they remain small (i.e. if the square of disturbance terms remains negligible with respect to the other terms in the governing equations) so that the system dynamics is in very good approximation linear around the steady solution. After some time, disturbances reach a non-negligible level, and non-linear effects (due to the quadratic terms of fluctuations) tend to moderate their growth until saturation (unsteady flow or steady state). The development of the global mode at Reynolds number $Re=60$ is illustrated in

Figure 3.8, where we present the time-history of the U- and V-velocity at point A (here the initial condition is the steady solution at $Re=60$). The initial exponential growth of the instability, as well as its non-linear saturation are clearly illustrated. On the U-velocity plot, notice that the steady solution (used here as initial condition) differs from the time-averaged value on the limit cycle. This characteristic of periodic flows is due to momentum transfer increase, caused by the action of Reynolds stresses.

As shown in the experimental studies on the circular cylinder wake (Mathis et al. 1984, Provansal et al., 1987), the dynamics of a single characteristic (complex) amplitude $A(t)$ of the unstable mode can be accurately modeled by the Stuart-Landau equation:

$$\frac{dA}{dt} = sA - lA|A|^2 + O(|A|^5) \quad (6)$$

This equation has been introduced by Landau (1944), who laid the foundations of the theory of non-linear hydrodynamic instability. Stuart (1958, 1971) further developed this theory, showed how Landau's equation can be derived, and applied his findings on the plane Poiseuille flow (Stuart and Watson 1960, Watson 1962). The amplitude A can represent any global quantity (e.g. the drag or lift coefficient) or a local quantity (e.g. the V-velocity at a given point). $s = \sigma_r + i\sigma_i$ is the global frequency, σ_r is referred to as the global growth rate, and σ_i is the linear frequency. The global frequency depends, of course, on the bifurcation parameter, which is here the Reynolds number, and is a global (i.e. spatially-independent) quantity. $l = l_r + il_i$ is the Landau constant, and in general depends on spatial location (i.e. the choice of A), but the ratio l_i/l_r is also a global parameter.

Experimentally, the development of global instability and its control in circular cylinder wakes has been studied by Schumm et al. (1994). To observe the unstable global mode from a steady state at supercritical Reynolds numbers, Schumm et al. first suppressed the flow unsteadiness using a certain control action (transverse oscillations or base blowing), and subsequently triggered the global mode by switching off the control action. They measured transient signals corresponding to the development of the global mode at several Reynolds numbers close to the critical, and analyzed them to compute the coefficients of the Stuart-Landau equation (6). As a general validation test of our simulations to experimental results, we followed the same signal analysis procedure outlined in Schumm et al. (1994), and computed the Stuart-Landau equation coefficients of the uncontrolled flows at $Re=50$ and $Re=60$. An advantage of simulation in this case is that the steady solution at exactly the

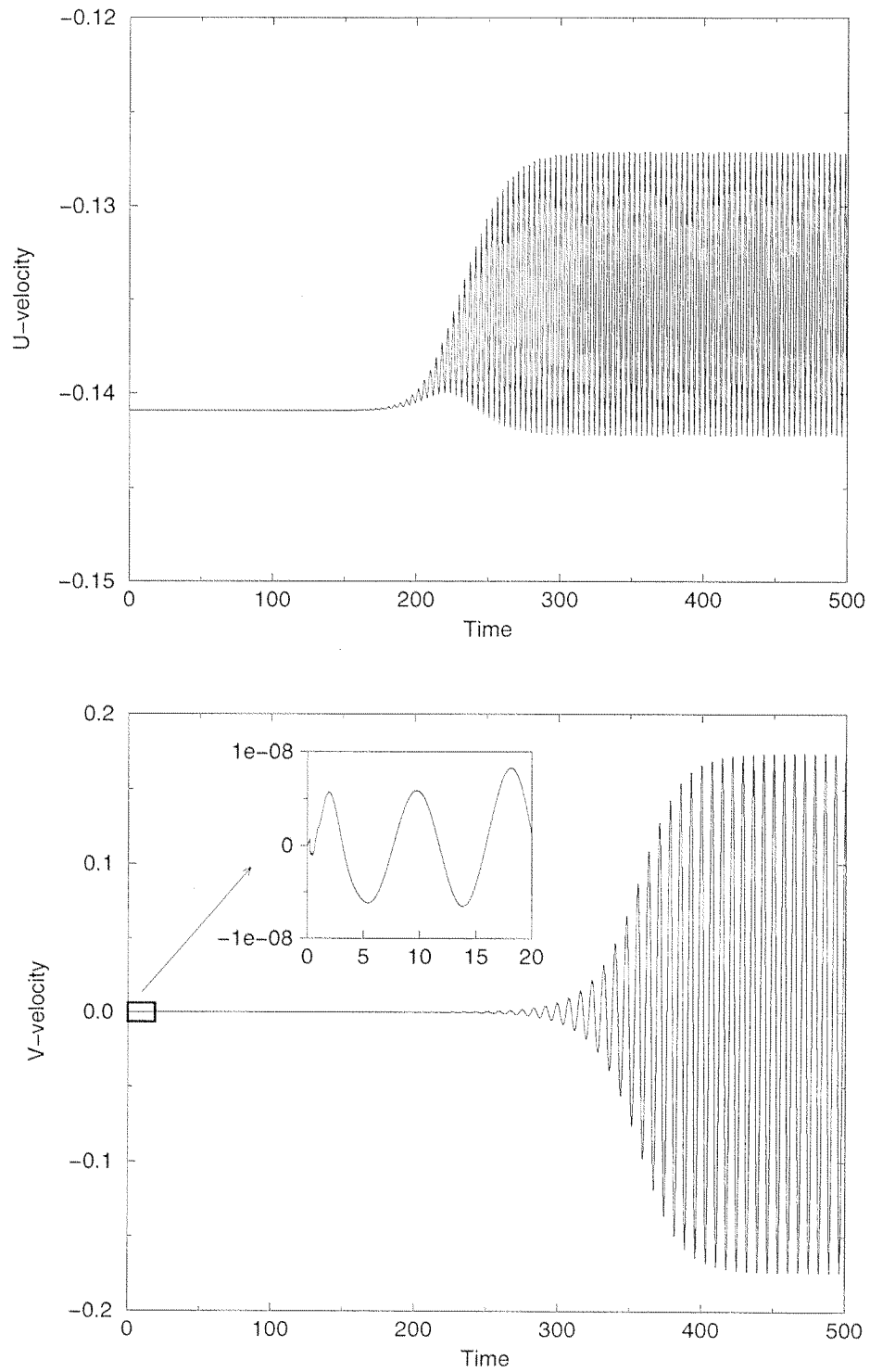


Figure 3.8: U- and V-velocity time-history at point A, illustrating the growth and saturation of global instability at $Re=60$.

same critical parameter value can serve as initial condition, which results in a smooth increase of disturbances from very small levels. Consequently, this is expected to yield more accurate values for the coefficients of the Stuart-Landau equation.

We now present the procedure for calculating these coefficients from a raw signal obtained from the simulation corresponding to the growth of an unstable mode at a given Reynolds number. Equation (6) governs the dynamics of any local amplitude of the dominant global mode. This can, for example, be the V-velocity at a point on the central axis, or the lift coefficient, the advantage of these choices being that the values oscillate around zero during the entire transient. The streamwise velocity at the same point or the drag coefficient have different values in the steady flow and in the time-average limit cycle (see Figure 3.8). Processing of such a signal would require more operations, in particular the extraction of the low frequency component (mean value) of the signal, and would make the entire procedure more complex and probably less accurate, since the corresponding filtering might introduce additional errors in the overall signal processing.

The computation of the coefficients requires a number of transformations to the original model. First, the dynamical behaviour of the magnitude $|A|$ of the chosen amplitude variable A can be easily derived from (6), by introducing complex conjugates, denoted by the *tilde* symbol:

$$\begin{aligned}
\frac{d|A|^2}{dt} &= \frac{d(A\tilde{A})}{dt} \\
&= A\frac{d\tilde{A}}{dt} + \tilde{A}\frac{dA}{dt} \\
&\approx A(\tilde{s}\tilde{A} - \tilde{l}\tilde{A}|A|^2) + \tilde{A}(sA - lA|A|^2) \\
&\approx (s + \tilde{s})A\tilde{A} - (l + \tilde{l})A\tilde{A}|A|^2 \\
2|A|\frac{d|A|}{dt} &\approx 2\sigma_r|A|^2 - 2l_r|A|^4 \\
\frac{1}{|A|}\frac{d|A|}{dt} &\approx \sigma_r - l_r|A|^2
\end{aligned} \tag{7}$$

Both equations (6) and (7) are commonly used to model non-linear instabilities, and are referred to as the Stuart-Landau model. Equation (7) yields an expression for the saturated magnitude $|A|_{sat}$ in the non-linear regime (limit cycle), since $\frac{d|A|_{sat}}{dt} = 0$:

$$|A|_{sat} \approx [\sigma_r/l_r]^{\frac{1}{2}}. \tag{8}$$

This last equation yields in turn a new form for equation (7):

$$\frac{1}{|A|} \frac{d|A|}{dt} \approx \sigma_r \left(1 - \frac{|A|^2}{|A|_{sat}^2}\right) \quad (9)$$

Finally, expressing the complex variable A by its modulus $|A|$ and phase α , $A(t) = |A|(t)e^{i\alpha(t)}$, and introducing this expression in equation (6) yields:

$$\begin{aligned} \frac{dA}{dt} &\approx sA - lA|A|^2 \\ \left(\frac{d|A|}{dt} + i|A|\frac{d\alpha}{dt}\right)e^{i\alpha} &\approx [\sigma_r + i\sigma_i]A - [l_r + il_i]|A|^2A \\ &\approx [(\sigma_r - l_r|A|^2) + i(\sigma_i - l_i|A|^2)]|A|e^{i\alpha} \end{aligned} \quad (10)$$

Equating real and imaginary parts on both sides of the above equation yields two relations, one for the quantity $\frac{1}{|A|} \frac{d|A|}{dt}$ (which represents an instantaneous growth rate), already derived in (7), and one for $\frac{d\alpha}{dt}$, which is proportional to the instantaneous flow frequency f :

$$\begin{aligned} \frac{d\alpha}{dt} = 2\pi f &\approx \sigma_i - l_i|A|^2 \\ &\approx \sigma_i - \left(\sigma_r \frac{l_i}{l_r}\right) \frac{|A|^2}{|A|_{sat}^2} \end{aligned} \quad (11)$$

From the latter equation, we find

$$\frac{l_i}{l_r} \approx \frac{\sigma_i - 2\pi f_{sat}}{\sigma_r} \quad (12)$$

where f_{sat} is the non-linear limit cycle frequency. This relation shows that the ratio l_i/l_r is indeed a global quantity, since all quantities on the right hand side are space independent.

We proceed further by following the signal analysis procedure outlined in Schumm et al. to construct the complex variable $A(t) = A_r + iA_i = |A|e^{i\alpha}$ from the raw signal A_r , e.g. the V-velocity transient at point A, as obtained from the simulations. To obtain the full complex signal $A(t)$, we just need to calculate its imaginary part A_i , by performing the Hilbert transform of the real part A_r :

$$A_i = Hilbert(A_r) \quad (13)$$

An ideal Hilbert transformer is an all-pass filter with a constant phase shift of $\frac{\pi}{2}$. Its transfer function in the frequency domain is:

$$H(F) = \begin{cases} -i & \text{if } F > 0 \\ +i & \text{if } F < 0 \end{cases} \quad (14)$$

Knowing the real and imaginary part of the signal, we can then obtain its magnitude $|A|(t) = \sqrt{A_r^2 + A_i^2}$ and its phase $\alpha(t) = \arctan(\frac{A_i}{A_r})$. Time derivatives of $|A|$ and α can then be approximated by finite differences. The coefficients σ_r and σ_i are obtained by extrapolating the functions $\frac{1}{|A|} \frac{d|A|}{dt}$ and $\frac{d\alpha}{dt}$ as $|A|^2 \rightarrow 0$ (see equations (9) and (11)). The remaining global coefficient $\frac{l_i}{l_r}$ follows immediately from equation (12).

Schumm et al. filtered their experimental raw signal with a band-pass filter, centered on the non-linear frequency f_{sat} , of bandwidth $\Delta f \approx f_{sat}$. This was necessary in their case, because an experiment is not free of external high frequency noise. In our case, signals obtained directly from the simulations are not contaminated by any high frequency noise source and therefore do not need any preliminary filtering.

We have analyzed V-velocity signals at point A. In Figures 3.9 and 3.10, we show the variations of the instantaneous growth rate $\frac{1}{|A|} \frac{d|A|}{dt}$ and the instantaneous frequency $f(t) = \frac{1}{2\pi} \frac{d\alpha}{dt}$ versus $|A|^2$, at $Re=50$ and $Re=60$, respectively. On both the growth rate and frequency plots, we show the data obtained from our signal processing (circles) and the prediction of the Stuart-Landau model, represented by the straight line joining the points corresponding to the linear state and the saturated limit cycle data (see equations (9) and (11)). Each circle corresponds to a local maximum of $|A_r|$ in the transient signal. Since the growth rate at $Re=60$ is about 4 times larger than at $Re=50$ (equation (5)), while frequencies do not differ significantly (by less than 10%), the data spacing is wider at $Re=60$. The extrapolation of data as $|A| \rightarrow 0$ yields accurate values for the linear growth rates and frequencies; the non-linear frequencies are also readily obtained from the data. The same processing of V-velocity signals at other points on the central axis (situated between the streamwise coordinates $X=1.5$ and $X=22$) yields very close values for the growth rates and frequencies, with a maximum discrepancy of the order of 0.1%. From the frequency data, we can identify the frequencies of the limit cycles f_{sat} at $|A|^2 = |A|_{sat}^2$, and thus the Strouhal numbers. They are in very good agreement with those of numerical simulations (see Figure 3.2): $St(50)=0.1239$, $St(60)=0.1362$, which is another validation of the signal processing procedure used here. The precise evolution of the instantaneous growth rates and frequencies with amplitude can serve as an indication of the adequacy of the Stuart-Landau model. The model is clearly more accurate at $Re=50$ than at $Re=60$, since the former value is closer to the critical Re value. The deviation from the critical Reynolds number can be evaluated by $\frac{Re-Re_{2D,cr}}{Re_{2D,cr}}$; it is about 6% at $Re=50$ and 30% at $Re=60$.

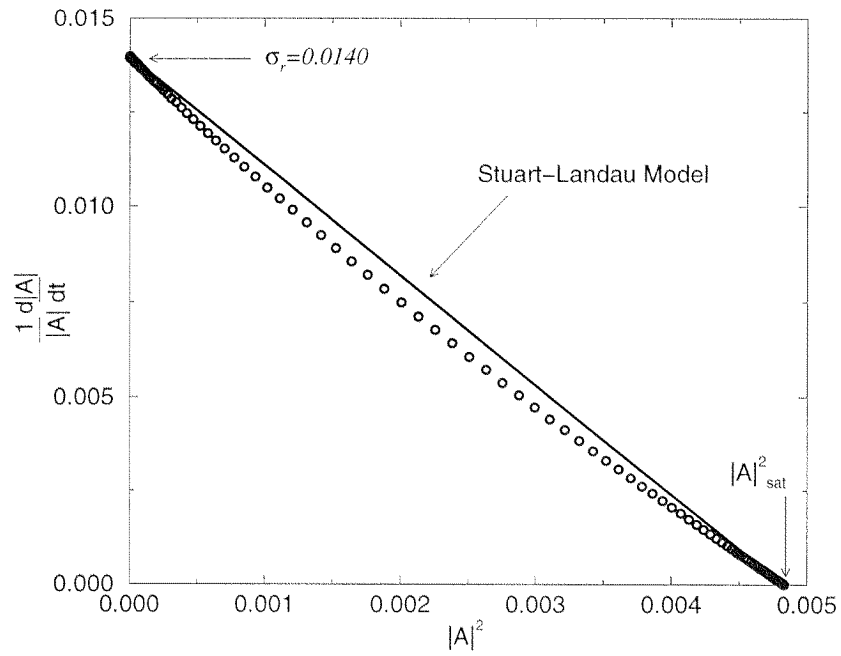
As we have noticed, the curves representing the instantaneous growth rate and frequency as functions of the amplitude $|A|^2$ do not perfectly follow the linear function prediction of the Stuart-Landau model, in particular at $Re=60$. These curves are much better approximated by square functions of $|A|^2$, i.e. functions of $|A|^4$. This suggests that, to better approximate the flow dynamics for $Re \geq 60$ with a model of the Stuart-Landau type, one should expand the Stuart-Landau model to higher order terms, i.e. $|A|^5$ instead of $|A|^3$ in equation (6).

In Table 3.2, we report the computed Stuart-Landau coefficients σ_r and σ_i , nondimensionalized by the time scale D^2/ν , as well as the ratio l_i/l_r (obtained from relation (12)), at $Re=50$ and $Re=60$. The results of Schumm et al. are also included in the table for comparison. We find good agreement between numerical and experimental results. As previously indicated, Schumm et al. used a controlled steady flow as initial condition and triggered the global mode by turning off the control action. As also seen in our numerical experiment (Figure 3.5), the process consists in an initial convergence to the new quasi steady state, and the subsequent formation and amplification of the global mode. Evidently, Schumm et al. have excluded the initial transients from their signal analysis.

	$Re=50$	$Re=60$
$\sigma_r D^2/\nu$ (present work)	0.70	2.9
$\sigma_r D^2/\nu$ (Schumm et al.)	0.69 ± 0.08	2.8 ± 0.1
$\sigma_i D^2/\nu$ (present work)	37.1	45.0
$\sigma_i D^2/\nu$ (Schumm et al.)	35.7 ± 0.6	42.1 ± 0.8
l_i/l_r (present work)	-2.51	-2.00
l_i/l_r (Schumm et al.)	-2.90 ± 0.45	-2.90 ± 0.45

Table 3.2: Coefficients of the Stuart-Landau equation at $Re=50$ and $Re=60$, corresponding to the present (computational) and previous (experimental) studies.

(a)



(b)

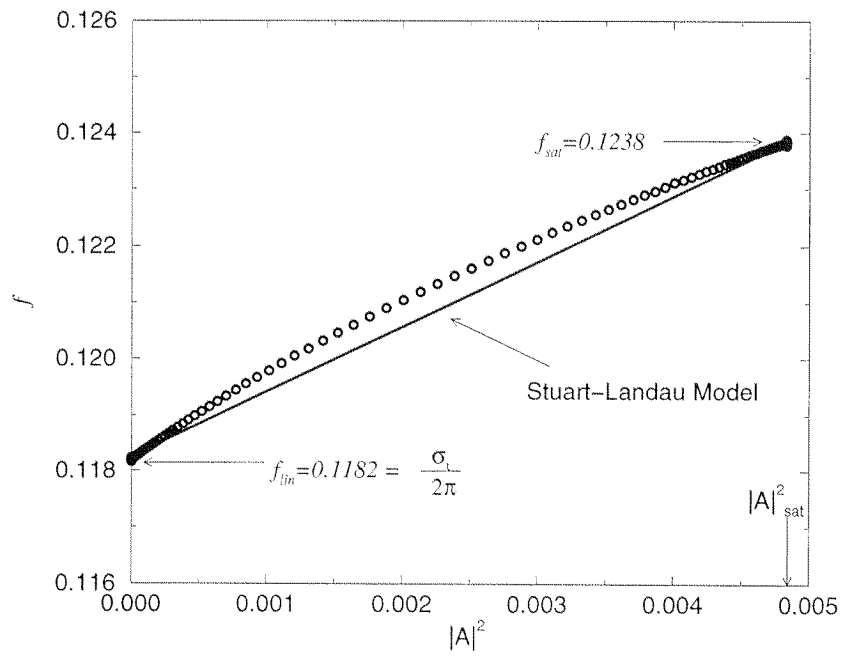
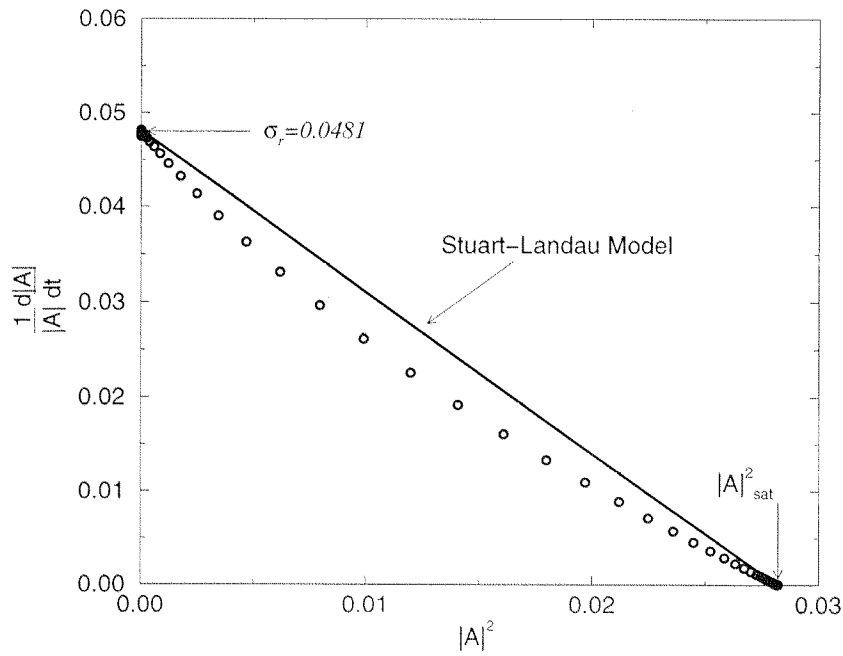


Figure 3.9: (a) Instantaneous growth rate $\frac{1}{|A|} \frac{d|A|}{dt}$ and (b) instantaneous frequency f of the uncontrolled flow at $Re=50$, versus global mode amplitude $|A|^2$. The data are obtained from the analysis of V-velocity signal at point A.

(a)



(b)

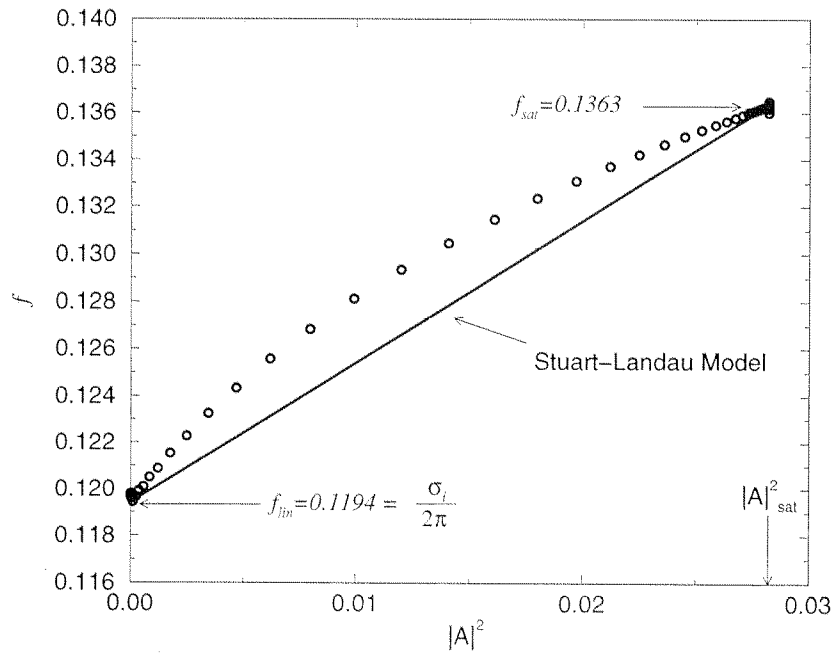


Figure 3.10: (a) Instantaneous growth rate $\frac{1}{|A|} \frac{d|A|}{dt}$ and (b) instantaneous frequency f of the uncontrolled flow at $Re=60$, versus global mode amplitude $|A|^2$. The data are obtained from the analysis of V-velocity signal at point A.

3.5 Mass conservation

In incompressible flow simulation, the divergence of the computed velocity field must remain at a very low level, to satisfy mass conservation (equation 1b, section 2.2), and is thus a good indicator of computational accuracy. Note that, in the splitting scheme used in the present work, incompressibility is not directly imposed on the final velocity field \mathbf{v}^{n+1} , but on the intermediate field $\hat{\mathbf{v}}$ (equation 12, section 2.3). Evidently, in an open flow, as the one of this study, global mass conservation should also be verified. Fulfillment of the integral form of mass conservation equation, taking the computational domain as the control volume, has been confirmed with accuracy of the order of 0.01%, for the entire range of system parameters investigated. On the other hand, the divergence field $DIV(x, y) = \frac{\partial U}{\partial x} + \frac{\partial V}{\partial y}$, while always being very close to zero far from the cylinder, can get high values close to the control action region, especially at high suction coefficients. At $Re=90$, $C_{suc}=0.2$ (corresponding to a maximal suction velocity of $0.55 U_\infty$), the divergence of an instantaneous velocity field reaches a maximum of $|DIV|_{max}=O(1)$ close to the cylinder base, whereas for the uncontrolled flow at the same Reynolds number, $|DIV|_{max}=O(10^{-2})$, compare Figures 3.11(a) and (c). At the same suction coefficient $C_{suc}=0.2$, but at lower Reynolds number, $Re=40$, the maximum of the divergence field is also $O(1)$, and located close to the cylinder base (Figure 3.11b).

The reason for high divergence errors is spatial underresolution. Therefore, spatial refinement of p- or h-type is necessary. For very high gradients present in the flow field, obtaining a divergence-free solution can be a tedious task. In all cases, one should make sure, with proper grid refinement studies, that basic flow properties and flow transitions are grid-independent. Note that, in the presence of a discontinuity in the boundary conditions, local refinement can increase the local divergence value. Spectral element solutions, while being very accurate for smooth fields, can be characterized by high-amplitude oscillations in discontinuous regions (Gibbs problem). Increasing the number of expansion functions corresponds to a p-refinement, and increases the accuracy of computations; however, in the presence of a pure discontinuity, p-refinement concentrates the errors closer to the discontinuity, with growing amplitude and frequency.

In our case, the suction velocity imposed on the cylinder surface is smoothed out at the two boundaries, but nevertheless, induces very high velocity gradients for $C_{suc} > 0.2$. To check for the effect of the suction profile on the divergence field, we also used a parabolic

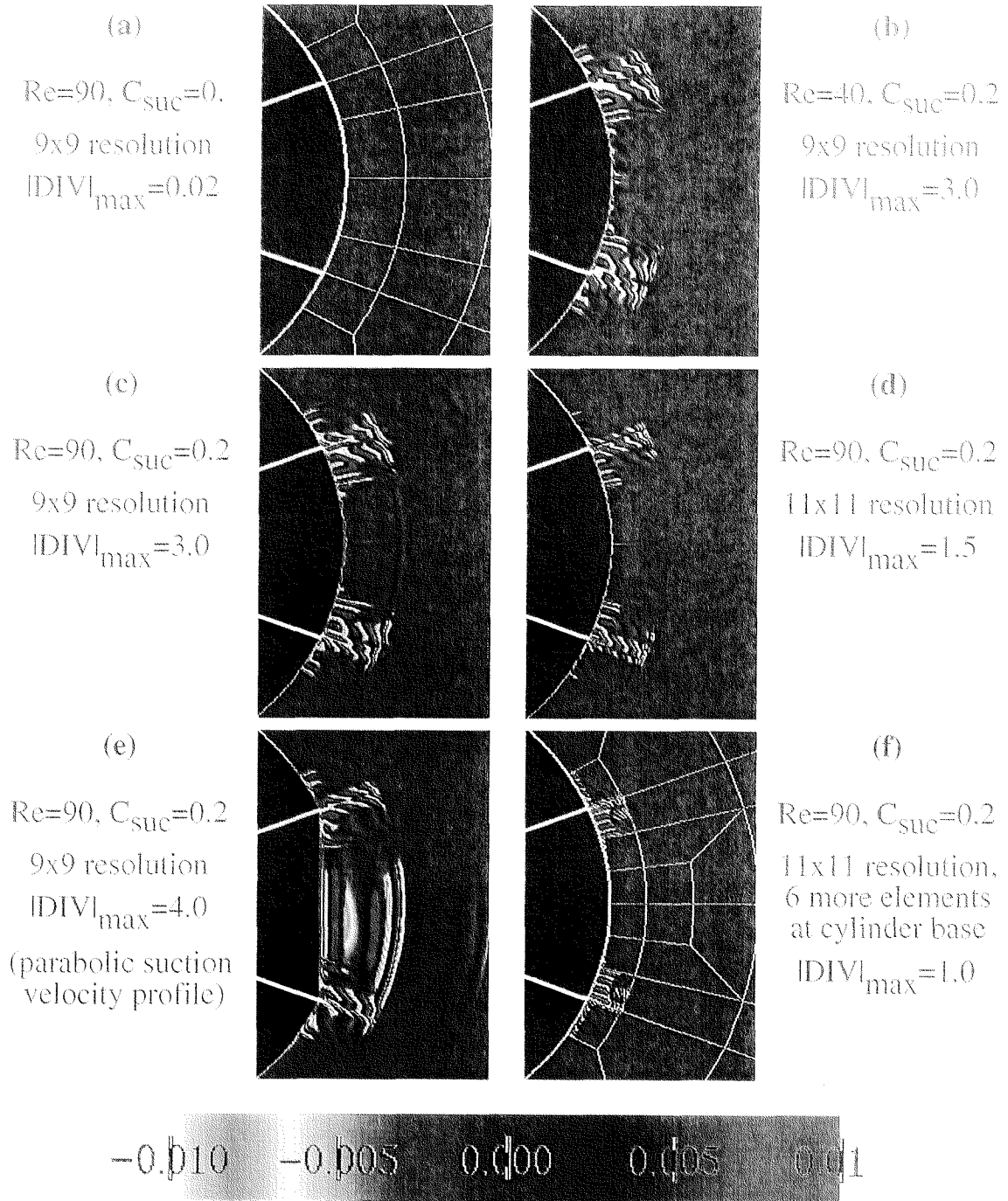


Figure 3.11: Instantaneous divergence fields at different system parameter values and spatial resolutions. The region of suction is delimited by the two white lines. The structure of the grid near the cylinder base is shown for (a) the original grid and (f) the h-refined grid.

profile along a straight line, joining the two edges of the suction hole. This profile is smoother than our standard one, sketched in Figure 2.1, as its maximum suction velocity gradient is smaller. We find that, with the new suction profile, divergence errors are slightly increased, and, moreover, are spread along the boundary (compare Figure 3.11c and 3.11e).

To investigate in more detail the dependence of divergence errors on resolution, we have performed p- and h- refinement tests, using the same flow parameter values ($Re=90$, $C_{suc}=0.2$). In Figure 3.11, we present the divergence field obtained with 11×11 elemental resolution on the original spectral element skeleton (Figure 3.11d), and with 11×11 elemental resolution on a skeleton refined near the cylinder base by the introduction of six supplementary elements (Figure 3.11f). We observe that the particular p-refinement performs better in decreasing the level of divergence errors, while h-refinement performs better in terms of increasing the region of divergence-free solution. Note that, despite the local high levels in divergence errors, we have complete control over their effects using resolutions tests. For example, in all computations with the standard suction profile, the non-dimensional shedding period is $T = 6.84$. The shedding period corresponding to the parabolic suction profile is $T = 6.80$. More extensive resolution tests (performed within the range $C_{suc} < 2.0$), including combined h- and p-refinement up to 13×13 elemental resolution, show that transitions and major flow properties are practically independent of the spatial resolution used in the present work (see also discussion on spatial resolution effects, section 3.3).

In Figure 3.12, we plot the V-velocity profile along the centerline, corresponding to the saturated steady flow at $Re=90$ and $C_{suc}=1.4$, for two elemental resolutions (9×9 and 11×11), and two spectral element skeletons: the original one, and the one corresponding to refinement by the addition of six elements in the region of suction. The Figure is a good representation of the Gibbs problem. We have encountered the Gibbs problem in simulations with the original skeleton, for $C_{suc} > 1.1$. At these high suction flow rates, and for locally underresolved domains, the velocity boundary condition is equivalent to a discontinuity. Refining the grid with both h- and p-refinement shows the continuous character of the boundary condition, and may significantly reduce the amplitude of oscillations near the boundary. Note that the Gibbs problem is only present in the first element next to the cylinder base, and that for $X > 0.6$ the V-velocity profile is smooth and accurately predicted for all grids tested. The drag coefficient differs by 3% between the coarsest and finest grid, a very reasonable value, given the sensitivity of drag to velocity gradients close to the

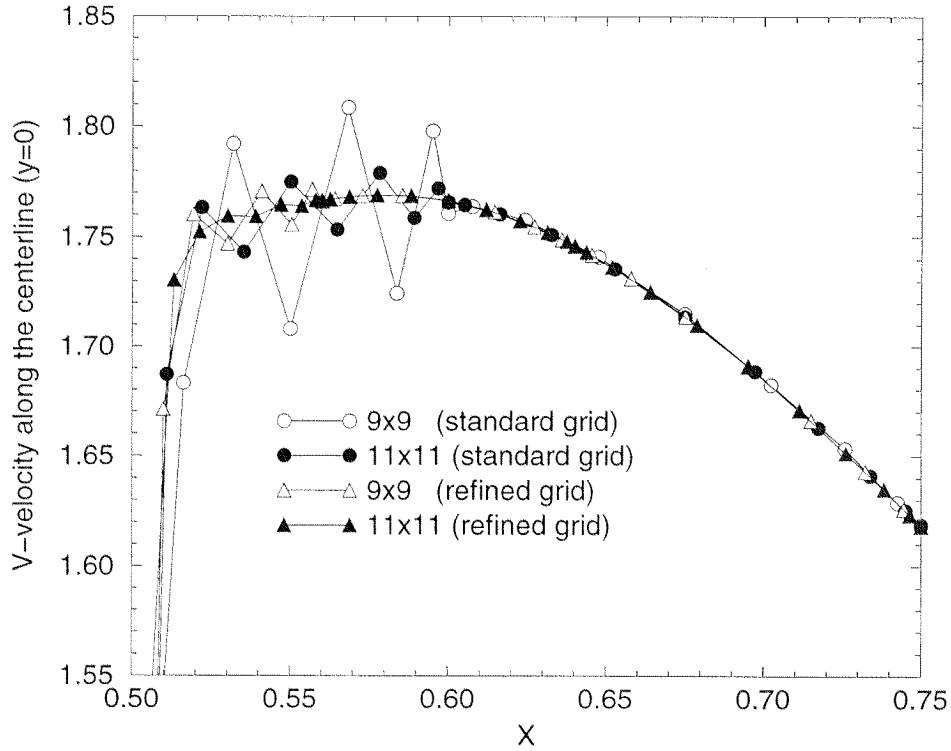


Figure 3.12: V-velocity profile along the centerline ($y = 0$) at $Re=90$, $C_{suc}=1.4$.

cylinder surface. The improvement in maximum divergence error with a combined h- and p-refinement is an order of magnitude, however divergence errors remain still high. The reduction of divergence errors in the suction region to levels characteristic of the far wake would require extremely fine local h-refinement. Because of the numerical stability constraint, this would result in such small Δt values, making simulations impossible with present computer resources. In summary, despite local high levels of divergence, there are no effects on flow transitions and only slight effects on the accuracy of major flow quantities. Based on these conclusions, and unless otherwise indicated, we will be using the original spectral element skeleton (348 elements), with 9×9 elemental resolution, in the detailed simulations reported in the following chapters.

3.6 Summary

The detailed tests reported in this chapter have shown that, for a number of combinations in flow parameters and initial conditions, the solution can be very sensitive to several numerical parameters. For supercritical system parameters, the linear evolution from (steady) base flow is strongly affected by the tolerance level in the velocity iterative solver; in the non-linear regime (e.g. on the limit cycle), the flow dynamics is insensitive to tolerance, if this is of the order of 10^{-8} and lower. Thus, we use $TOL = 10^{-8}$ for flow parameters far from transitions, and $TOL = 10^{-16}$ close to critical states. For flows evolving from a base state, instability can often be successfully triggered by either increasing the time step, or decreasing the tolerance level, the former being evidently less expensive computationally. Based on the tests performed, we choose a 9×9 elemental resolution for the detailed studies of the next chapters. Finally, the type of control action used here (suction/blowing) can result in high levels of divergence errors in the proximity of cylinder base. Based on spatial resolution tests, we have shown that divergence errors decrease at increased resolution and, most importantly, that their presence does not affect flow transitions and overall accuracy in computed basic flow parameters (drag and lift coefficients, Strouhal numbers, etc).

Seite Leer /
Blank leaf

Chapter 4

Flow control simulations

4.1 The flow under control action

As previously mentioned, we expect that the wake stability is affected by suction and blowing, both at supercritical and subcritical Reynolds numbers. Our first objective is to calculate asymptotic states for a large number of parameter sets (Re, C_{suc}) . To this end, we proceed as follows: uncontrolled flows ($C_{suc} = 0$) are first calculated for several Reynolds numbers. Subsequently, the control action is progressively increased, i.e. C_{suc} is increased (suction) or decreased (blowing), until a transition occurs. Then, the precise value of critical suction coefficient is approximated by a dichotomy approach, until a precision of 0.005 in absolute or 1% in relative value is achieved.

Simulations have been performed over a wide range of the system parameters, including high suction coefficient values, for which experimental data are hard to get. Figure 4.1 summarizes the computed flow states in the system parameter plane (Re, C_{suc}) , obtained with the standard domain. The flow states corresponding to uncontrolled flow are indicated by the dashed horizontal line, which crosses the critical curve at $Re = 47$.

For a given Re , we report (squares) a value corresponding to the mean C_{suc} of the computed two closest flow states, separated by a critical line. The circles correspond to the critical parameter sets observed experimentally by Schumm et al. (1994) in a similar flow configuration. As illustrated in Figure 4.1, in the subcritical Reynolds number regime ($Re < 47$), we find that suction leads first to unsteadiness, and then again to a steady flow at high enough suction coefficient values (over 1.80 or so). In this regime, blowing has no effect

on the wake stability. For $Re < 17$, no control action can render the wake unsteady. At supercritical Reynolds numbers ($Re > 47$), even small blowing flow rates stabilize the wake, whereas much stronger suction is necessary to achieve this goal. In spite of the differences in the details of flow setup, the computed critical suction coefficient values are in good agreement to the ones found by Schumm et al. (1994).

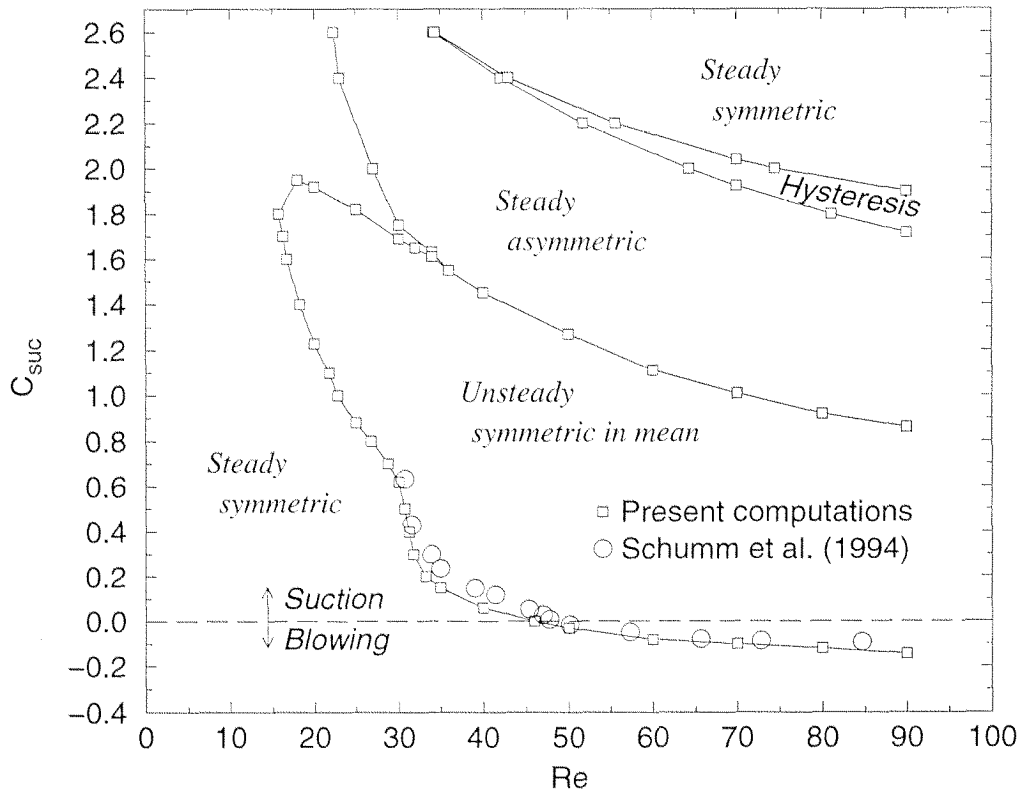


Figure 4.1: Flow states and critical curves in the parameter plane, $Re - C_{suc}$.

Based on their data, Schumm et al. report a higher threshold value ($Re = 27$), below which the wake cannot become unsteady. This threshold value is slightly higher, compared to the observations of Berger (1964), and Nishioka and Sato(1978), who report a corresponding value of $Re = 20$. This limit in Re given by Schumm et al. is based on observations at rather low suction coefficient values (around 0.6-0.7). The highest suction coefficient they tested is about 0.62 at $Re \approx 30$, which is very close to the critical value for C_{suc} we also find at $Re = 30$. To further explore the issue, we also performed simulations with a suction velocity

profile defined on a straight boundary, corresponding to an angle $\theta_0 = 30^\circ$ (see Figure 2.1), to approximate more closely the experiment of Schumm et al. With this new set-up, we could also destabilize the wake for Reynolds numbers below 20.

The value of critical suction coefficient at which the wake is stabilized is much higher in the case of control by suction than by blowing. This suggests that blowing is a much more efficient method for stabilizing the wake. For the Re range considered here, the minimal critical suction coefficient rendering the wake steady is equal to 0.855, and is obtained at the highest Re value studied, $Re = 90$. This is surprising, as one expects the control effort to increase with Reynolds number. We present a possible explanation for this trend in a subsequent paragraph, based on further results. We expect that the critical curve will tend to an asymptote for Reynolds numbers increasing beyond 90.

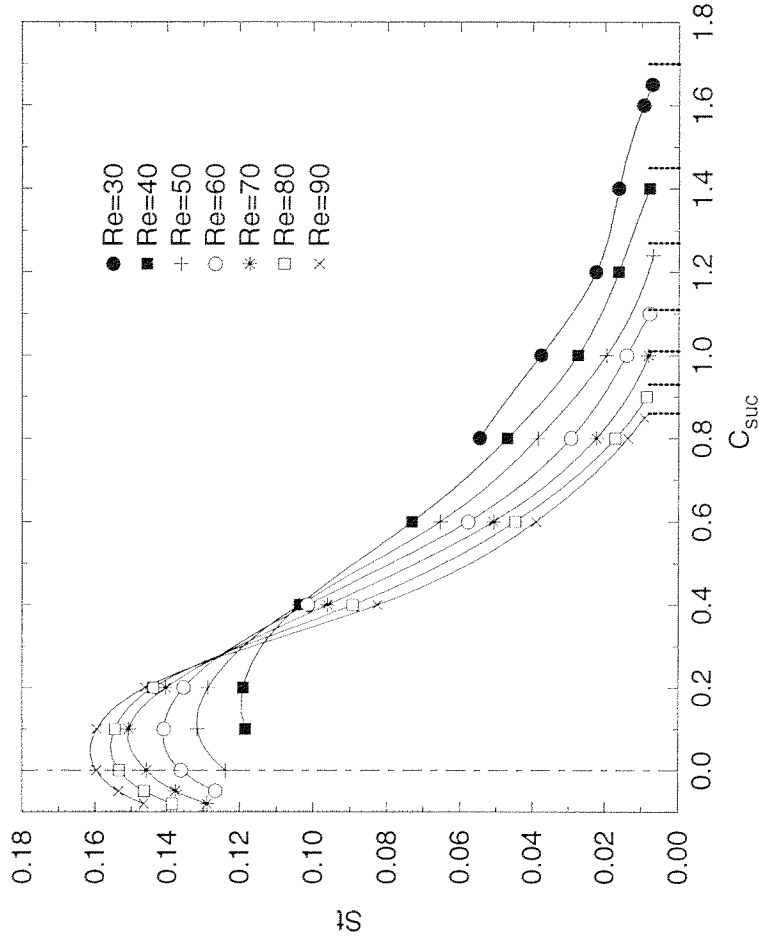
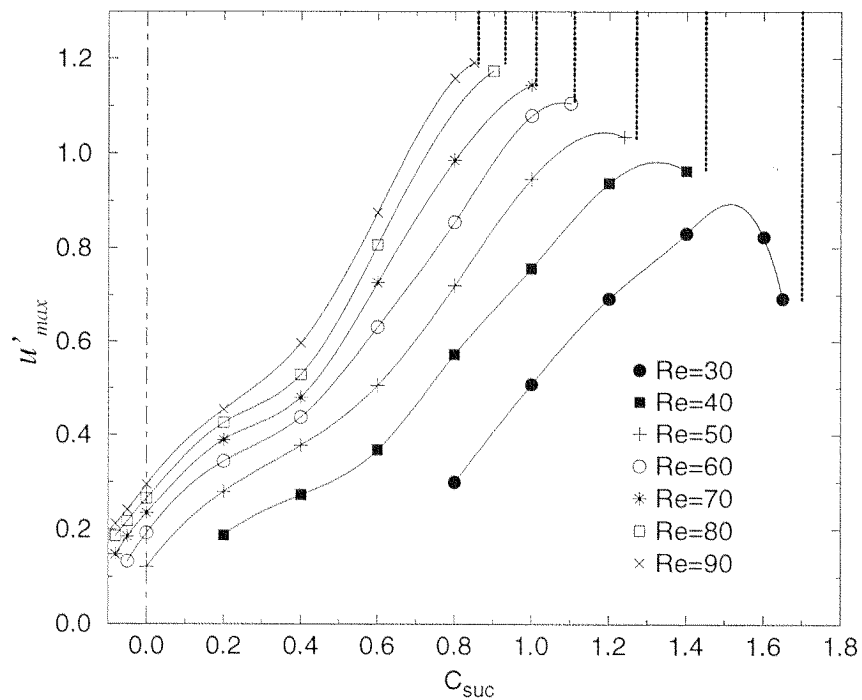


Figure 4.2: Strouhal number versus suction coefficient at different Reynolds numbers.

We now report flow properties in the unsteady regime. Figure 4.2 illustrates the effect of suction on the wake, in terms of the non-dimensional frequency (Strouhal number) of the

(a)



(b)

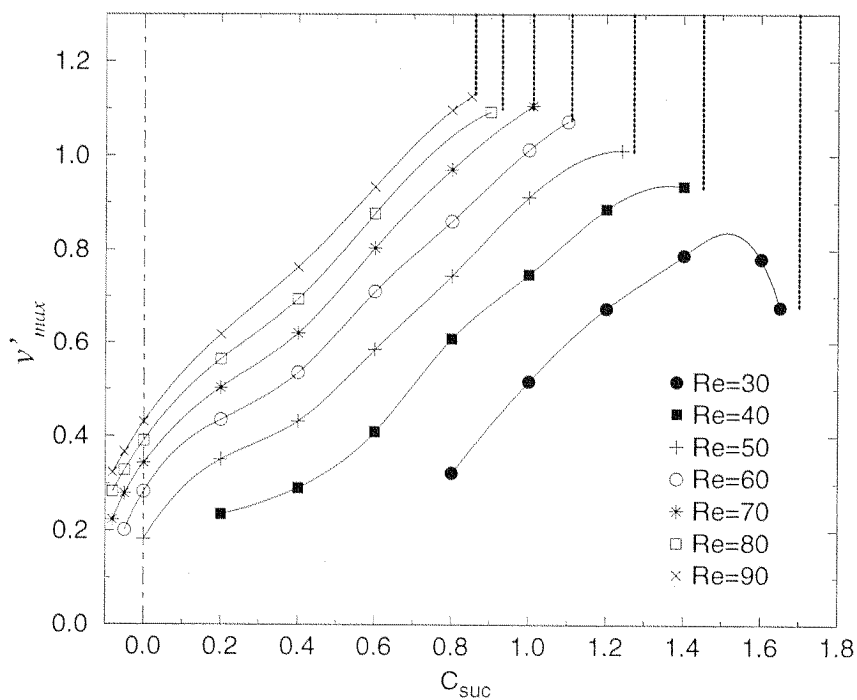


Figure 4.3: (a) u'_{max} and (b) v'_{max} versus suction coefficient at different Reynolds numbers.

vortex shedding limit cycle. For all Re , the critical suction coefficient is indicated by the dashed line at the right end of the curve. The dotted-dashed line stands for the uncontrolled flow. At supercritical Re , the Strouhal number first increases and then decreases quite rapidly with increasing suction. The decrease of Strouhal number with suction is steeper at higher Re , and the function $St(Re)$ becomes decreasing at high suction coefficients, whereas it is increasing for the uncontrolled flow. These values confirm the dramatic effect of suction on the flow structure and dynamics, and also indicate that the flow is more sensitive to suction at higher Reynolds numbers; this results in the previously mentioned earlier stabilization of the wake at higher Reynolds numbers.

To better understand the unsteady flow patterns at subcritical suction coefficients, in addition to St , the amplitude of velocity fluctuations is also an important parameter. A global intensity of flow oscillations can be expressed in terms of the maximum value of the RMS fluctuation intensities (u'_{max} and v'_{max}) over the whole domain. In Figure 4.3, u'_{max} and v'_{max} values are presented as function of the suction coefficient, for different Reynolds numbers. Clearly, the fluctuation intensities increase with C_{suc} , reaching a maximum close to the critical suction coefficient. Fluctuation intensities are also increasing functions of Re , as would have been intuitively expected.

Figure 4.4 shows the maximum values of u' and v' RMS fluctuation intensities along lines of constant x , as functions of the streamwise coordinate x , at $Re = 90$. The figure provides more precise information on the effects of suction and blowing in the near and far wake. Suction tends to increase the velocity fluctuations in the entire wake, but most in the very near wake. On the other hand, with blowing, the fluctuations are smoothly damped to zero in the near wake, from an almost constant non-zero level farther downstream. Thus, blowing displaces the fluctuation maxima downstream (see Figure 4.4). This can be interpreted on the basis that blowing naturally tends to ‘blow away’ flow patterns from the near wake. Consequently, vortex formation and shedding appear at increasing streamwise location with increasing blowing flow rate. This phenomenon is clearly illustrated on Figure 4.5, showing colour-coded instantaneous vorticity isocontours at $Re=90$ and $C_{suc}=-0.14$.

Based on Figures 4.2, 4.3 and 4.4, we expect that, at (positive) suction coefficient values close to the critical, the flow structure is very different from that in the uncontrolled case. Note that here an increase in RMS fluctuations can be accompanied by an increase in flow intermittency: the time-history of V-velocity at point A, for $Re = 90$ and $C_{suc} = 0.85$,

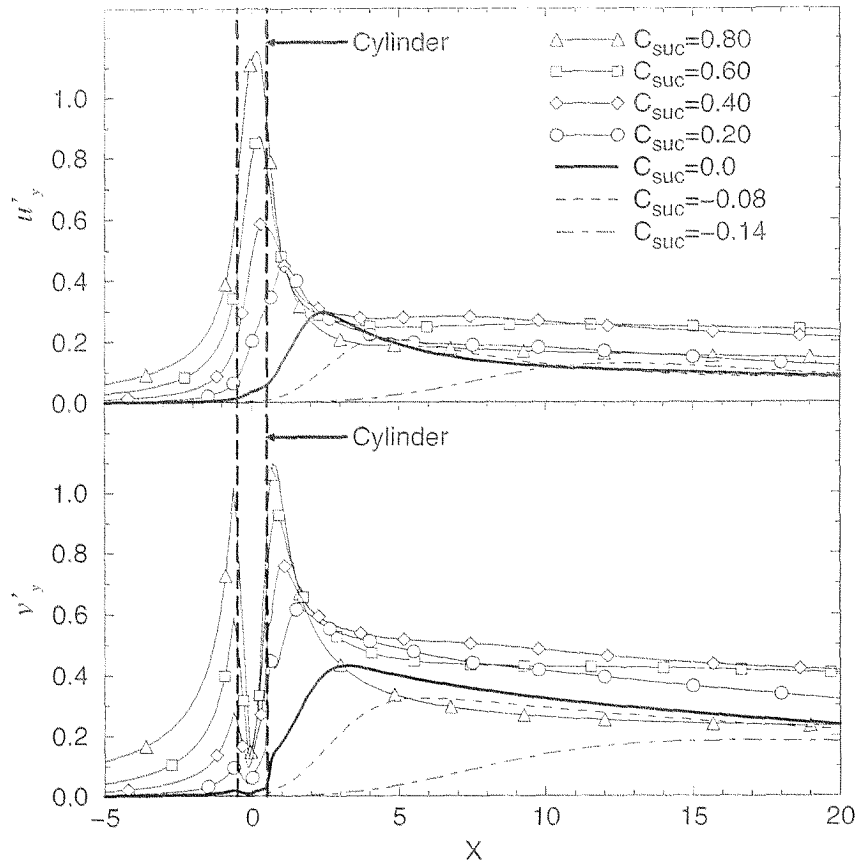


Figure 4.4: $Re=90$: maximum RMS fluctuations along lines of constant x , u'_y and v'_y , versus streamwise abscissa, for different suction coefficients.

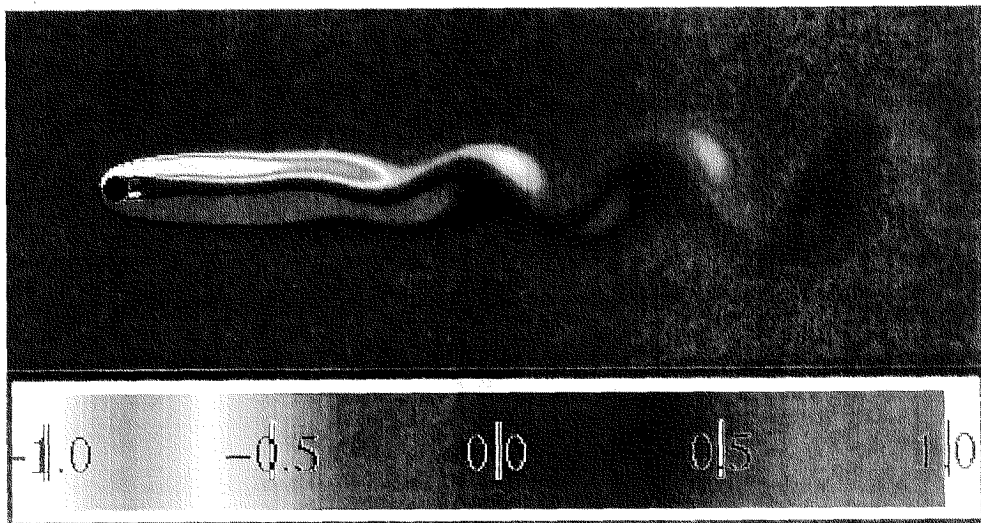


Figure 4.5: $Re=90$, $C_{suc}=-0.14$: colour-coded instantaneous vorticity isocontours.

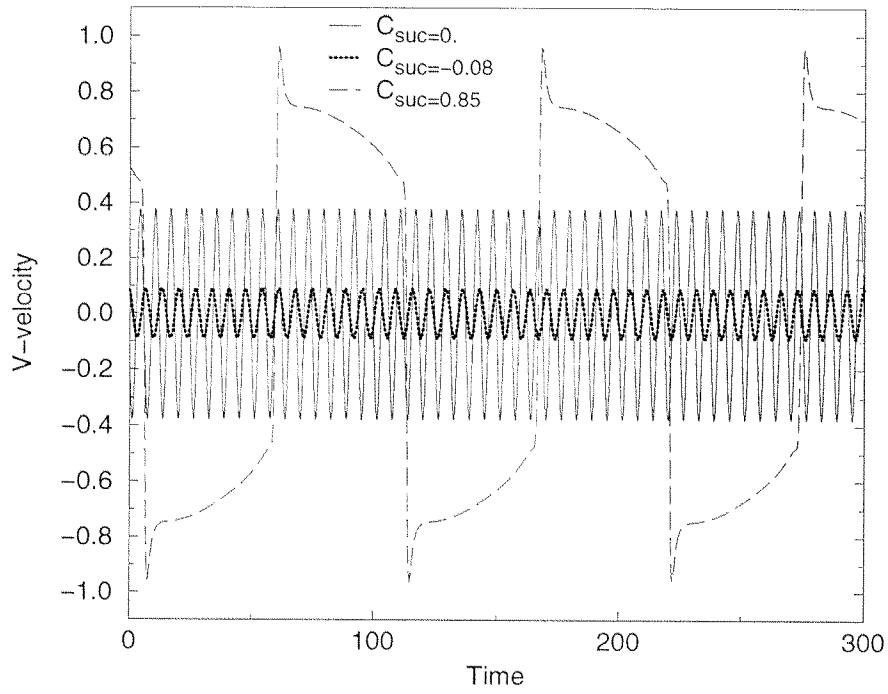


Figure 4.6: $Re=90$: time history of the V-velocity on the limit cycle at point A, for different suction coefficient values.

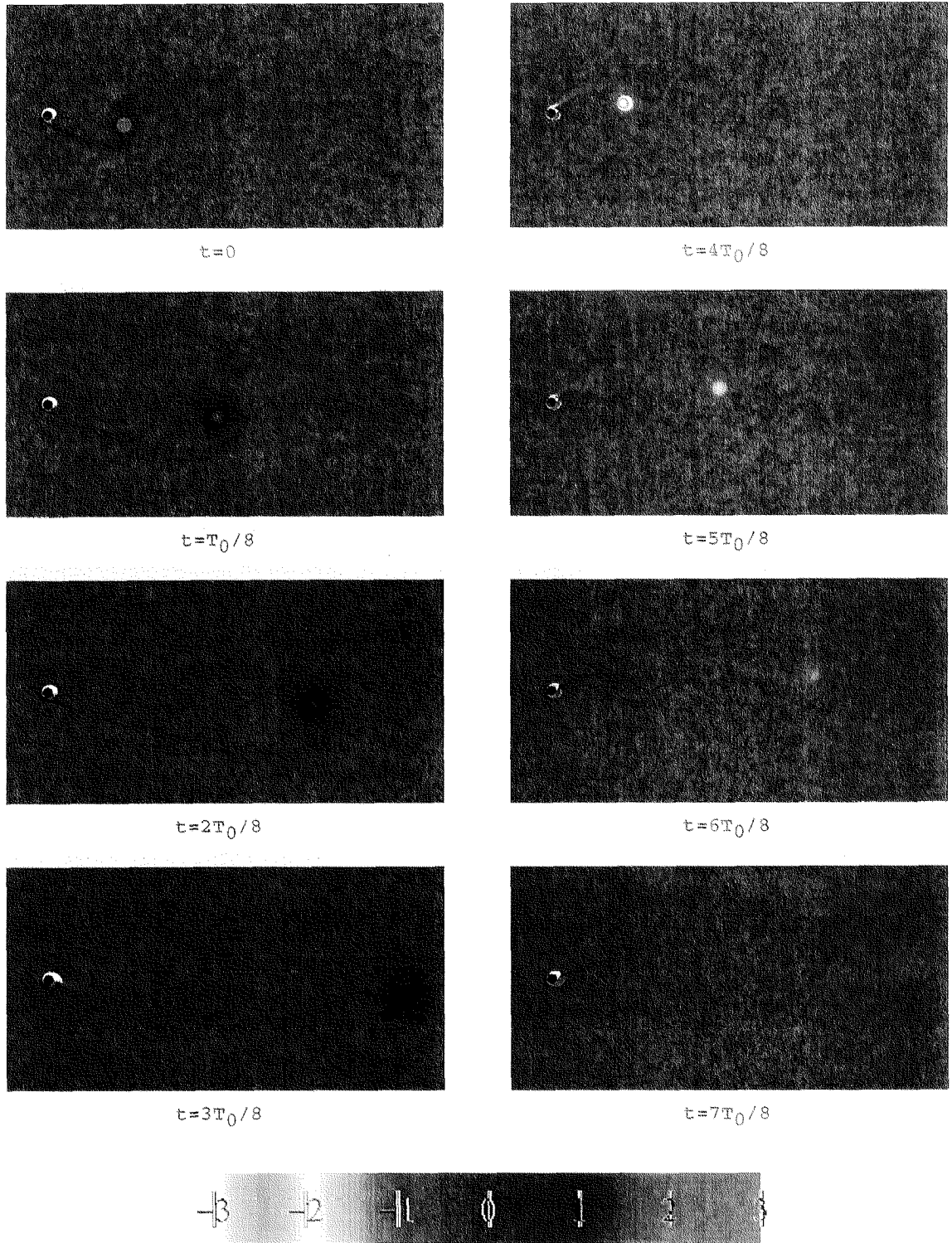


Figure 4.7: $Re=90$, $C_{suc}=0.8$: time evolution of vorticity over one shedding period ($T_0=72.8$).

corresponding to a point slightly below the critical curve, shows that suction indeed tends to make the flow intermittent and to amplify fluctuations (see Figure 4.6). Time histories at lower C_{suc} values confirm the the high differences in amplitudes and frequencies at different C_{suc} values (Figure 4.6). The strong modification of vortex shedding with large suction is illustrated in Figure 4.7, where we present a sequence of instantaneous vorticity isocontours over one shedding period, for $Re=90$ and $C_{suc}=0.8$. The large increase in shedding period results in the formation of distinct vortices in the flow domain. Here the shape of each vortex is not affected by the presence of other vortices, as in the uncontrolled flow; thus the vortices acquire a circular form.

The time variation of V-velocity at the centerline point A, as C_{suc} is impulsively increased from 0.85 to the supercritical value 1.0 at $Re=90$ is presented in Figure 4.8. The sudden increase of C_{suc} (indicated by the dashed line) results in suppression of flow unsteadiness, with the V-velocity at the centerline converging to a steady non-zero value, representative of flow asymmetry.

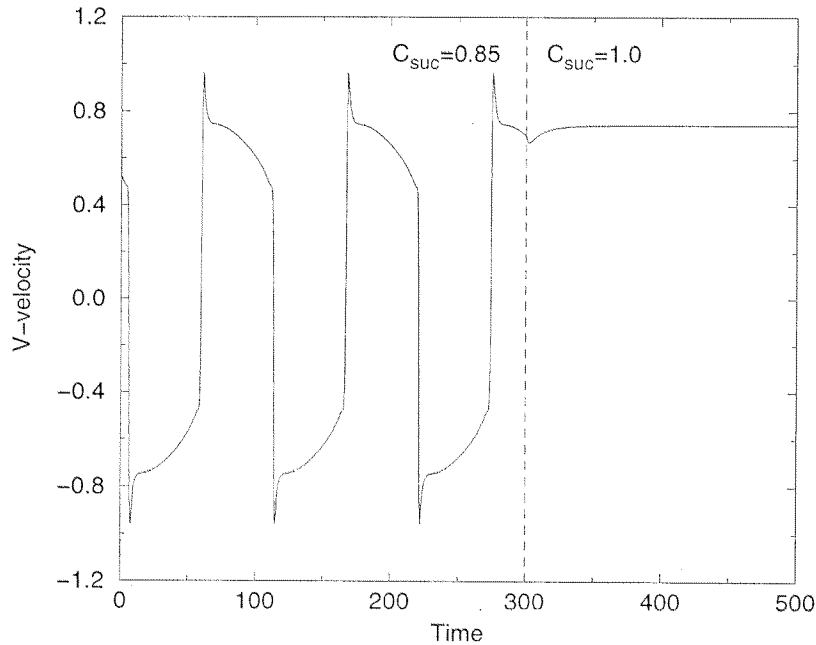


Figure 4.8: $Re=90$: wake transient (V-velocity at point A) as the suction coefficient is impulsively increased from $C_{suc}=0.85$ to $C_{suc}=1.0$.

The transition from unsteady to steady flow by means of suction control is characterized by a simultaneous transition to asymmetry only for $Re \geq 36$, and to symmetry for $Re < 36$. The previous discussion on RMS and intermittency helps in understanding the transition from a limit cycle to a steady asymmetric flow at high enough Reynolds numbers. As indicated, just below the critical curve and for all Reynolds numbers, the unsteady flows exhibit very low frequencies, associated with long wavelengths, and high values of RMS fluctuations; moreover, at high enough Re values, the flows are intermittent. In an intermittent case, the combined effect is an instantaneous flow structure characterized by strong asymmetry over a significant streamwise extent, for long time-periods (due to the low shedding frequency). It has been observed (Hammond and Redekopp 1997b), that wakes exhibiting stronger asymmetry are by nature more stable (or stabilizable with less control effort). From Figures 4.2 and 4.3, it is clear that flows attain higher levels of asymmetry and intermittency at increasing Reynolds numbers. This is consistent with our results indicating that stabilization is accompanied by transition to asymmetry only at high enough Re values, and that the critical C_{suc} value is a decreasing function of Reynolds number.

In Figure 4.9 we present the V -velocity time-history at point A, for $Re=30$ and $C_{suc}=1.65$, just below the critical curve separating unsteady and steady symmetric flow regimes. By comparing it with Figure 4.6, we find that the normal velocity fluctuation amplitude is not as large as for higher Reynolds numbers; in addition, fluctuations are regular and not intermittent in nature. In this case, the observed transition at a slightly higher C_{suc} is to a *symmetric* steady flow. Figure 4.10 presents instantaneous vorticity fields at $Re=30$, for two suction coefficient values, $C_{suc}=1.2$ and $C_{suc}=1.4$, within the unsteady regime. Note the different form of vortices, compared to the case represented in Figure 4.7, as well as the corresponding decrease in the intensity of vorticity. The figure indicates that, at subcritical Reynolds numbers, an increase in suction coefficient results in the displacement of vortex shedding farther downstream, which is accompanied by reduced vorticity magnitudes. As shown in Figure 4.10, at $C_{suc}=1.2$, two distinct vortices evolve within the computational domain, whereas at $C_{suc}=1.4$, only one vortex is present; at $C_{suc}=1.6$, the outflow length of the standard domain is not sufficient to visualize vortex shedding. These combined effects of suction on the dynamics of vortex shedding at subcritical Reynolds numbers clarify the smooth transition to steady symmetric flow at a critical suction coefficient.

We now emphasize on the transitions that the flow undergoes at $Re=90$, with increasing

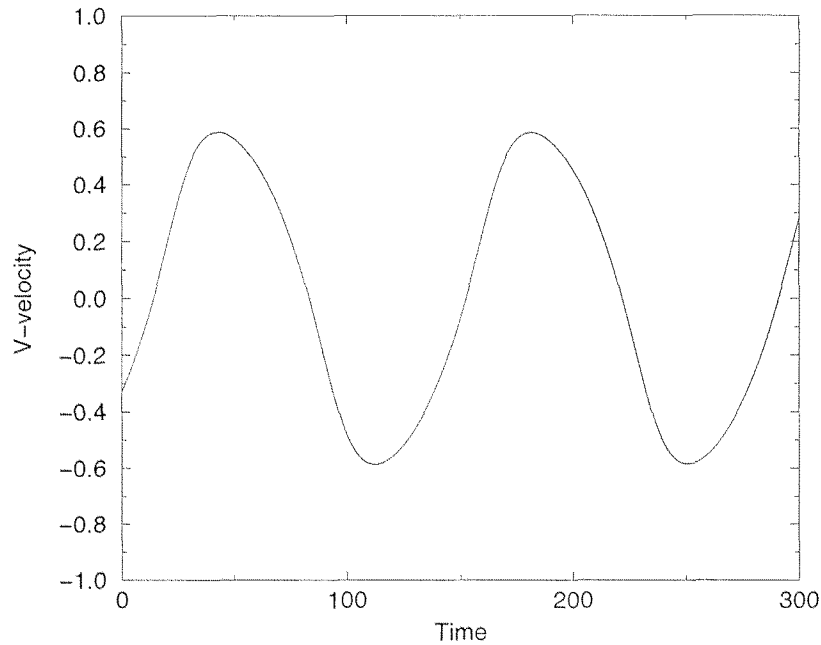


Figure 4.9: $Re=30$, $C_{suc}=1.65$: time history of V-velocity at point A on the limit cycle.

C_{suc} within the suction regime. Figure 4.11 is a bifurcation diagram at $Re=90$, showing the absolute value of the time-averaged V_A (V-velocity at point A) of the flow in the asymptotic state, as a function of the bifurcation parameter C_{suc} . We now consider the Reynolds number fixed at this value until otherwise stated, so the system depends on only one bifurcation parameter, C_{suc} . For steady flows, ($C_{suc} > 0.855$), the time-averaged value coincides with the asymptotic value. The flow is unsteady and symmetric in the mean for subcritical values of the suction coefficient ($C_{suc} < 0.855$), so the time-averaged V-velocity along the centerline is zero.

After the first bifurcation, occurring at $C_{suc,1}=0.855$, two stable, steady asymmetric solutions exist (they are mirror-image of each other), and the centerline V-velocity can be positive or negative. Convergence to either one of the two solutions depends on the initial condition. In this regime, the steady symmetric flow solution is unstable. These properties are typical of a pitchfork bifurcation. Figure 4.12 shows the streamline pattern corresponding to one of the two asymmetric solutions for the parameter set ($Re=90$, $C_{suc}=1.0$), indicating a strong deflection of the front stagnation point and overall flow asymmetry. No separation

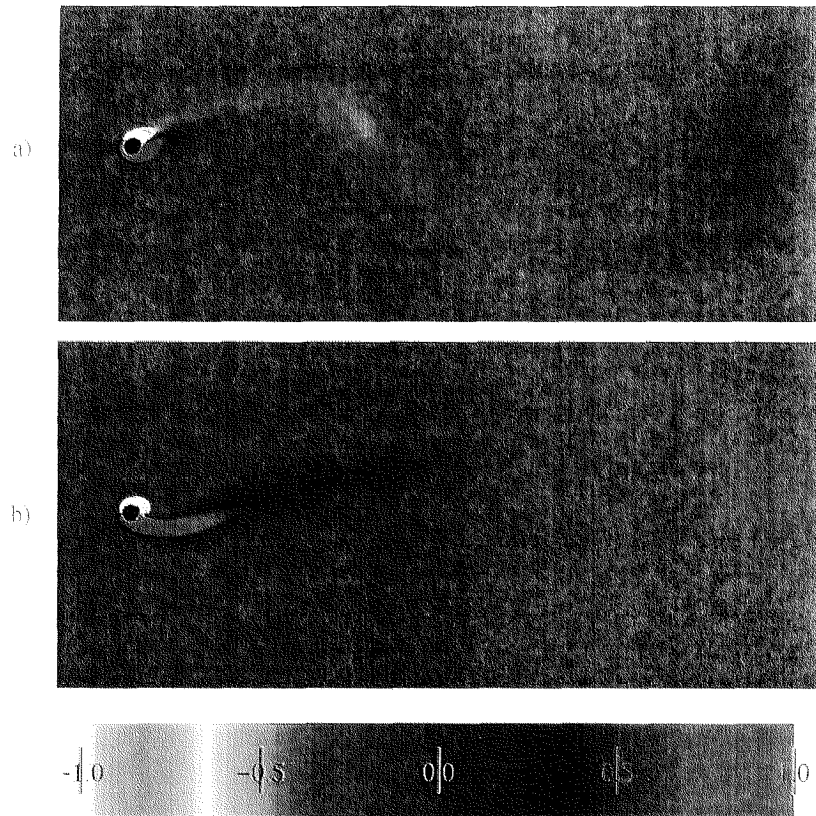


Figure 4.10: $Re=30$: colour-coded instantaneous vorticity contours. (a) $C_{suc}=1.2$, (b) $C_{suc}=1.4$.

from the cylinder surface is present. Note that streamlines are convergent in the region below the cylinder and slightly divergent above the cylinder. This indicates that the flow is accelerated below the cylinder and is slightly decelerated above it. As a consequence, the streamwise velocity field is strongly asymmetric around the cylinder, with much higher values below than above the cylinder (see Figure 4.13). Therefore, the steady pressure field around the cylinder is also highly asymmetric, with much lower values in the region of high velocity. This is also illustrated on Figure 4.13, where we see a large region of strongly negative pressure below the cylinder, especially near the region of suction, where velocity gets high amplitude. This flow configuration is therefore characterized by a high lift coefficient value, in this case negative, which corresponds to a force directed downward (towards the low pressure region). Quantitative data of the drag and lift coefficients are presented below.

At a second critical value, $C_{suc,2}=1.72$, the flow bifurcates again and the steady symmetric solution becomes also stable. Above a third critical value, $C_{suc,3}=1.90$, only the symmetric

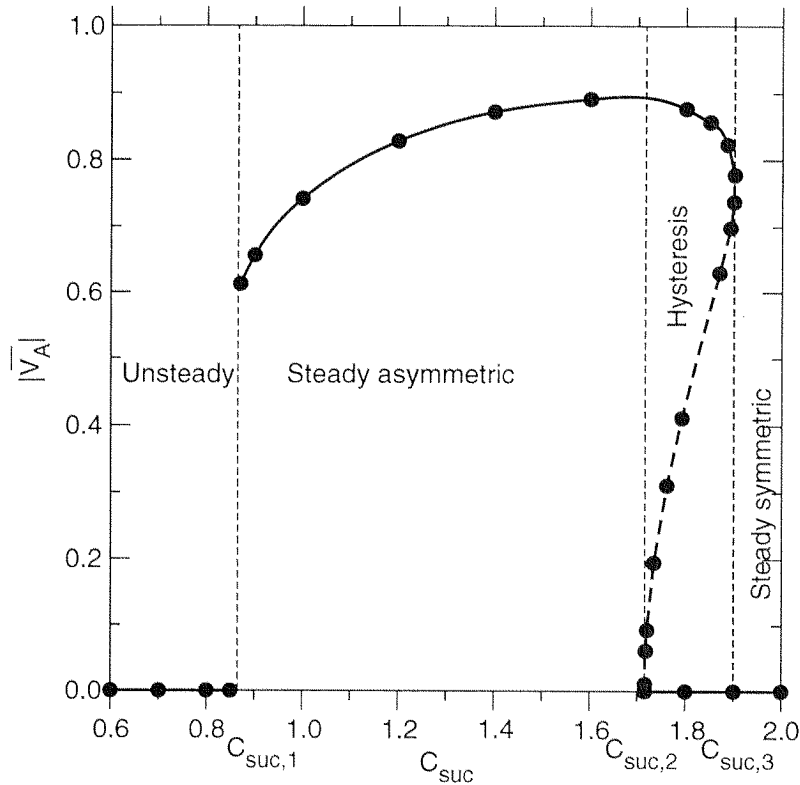


Figure 4.11: $Re=90$: absolute value of time-averaged V_A value versus C_{suc} .

solution remains stable. Thus, at $Re=90$, the second bifurcation is characterized by a hysteresis regime in the range $C_{suc,2} < C_{suc} < C_{suc,3}$. Hysteresis is characteristic of subcritical bifurcations. Within this narrow range of the bifurcation parameter C_{suc} , both the symmetric and asymmetric solutions are stable and can be realized physically. Again, convergence to either the symmetric or to the strongly asymmetric solution depends on the initial condition. For example, a flow evolving at $C_{suc}=1.75$ will either converge to a symmetric state if the initial flow state is slightly asymmetric (or symmetric), or to a strongly asymmetric flow if the initial state is more asymmetric. The hysteresis region is also indicated in the map of flow states (Figure 4.1).

Subcritical bifurcations are also characterized by the existence of a branch of unstable solutions in the hysteresis regime, connecting the two stable branches. The branch of unstable solutions is represented by the dashed part of the curve in Figure 4.11. These unstable solutions are steady and slightly asymmetric. Since we use a time-dependent Naviers-Stokes

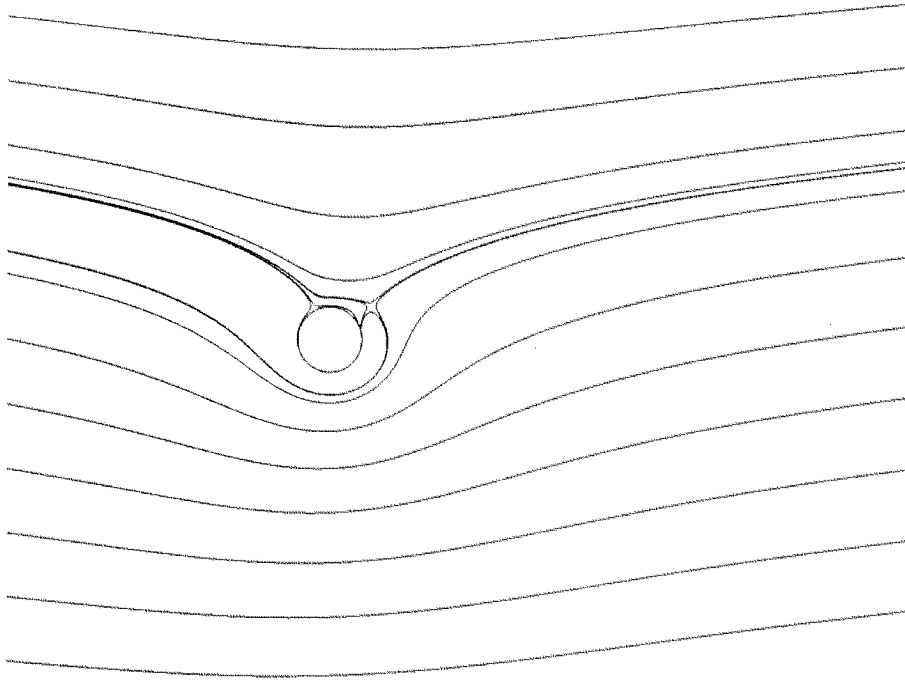


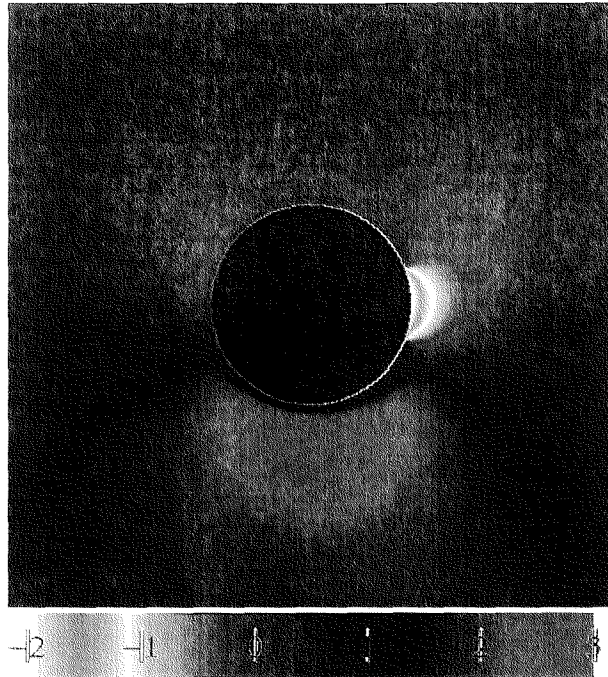
Figure 4.12: $Re=90$, $C_{suc}=1.0$: streamline pattern of the time-asymptotic flow state.

solver and thus cannot solve for unstable steady flows, we have implemented a feedback control module in the numerical code, to stabilize these unstable flow solutions. The feedback control strategy is presented in detail in the next section.

The overall flow asymmetry can be expressed in terms of the deflection of the front stagnation point, with respect to the centerline. The precise location of the stagnation point can be determined from the pressure maximum on the cylinder surface. In Figure 4.14, we plot the angle (in degrees) formed between the centerline and the line connecting the stagnation point and the cylinder center, as function of C_{suc} ($Re = 90$). The transitions are indicated by dashed vertical lines. This figure clearly illustrates the abrupt transition to asymmetric flow, as well as the multiplicity of solutions within the hysteresis regime. Note the very high values of the deflection angle in the asymmetric regime, especially for $C_{suc} \geq 1.2$.

We emphasize now on the force exerted by the fluid on the cylinder via viscous stresses and pressure. The total force is expressed in non-dimensional form by the drag (streamwise component) and lift (normal component) coefficients, both defined in chapter (3). We calculate drag and lift by integrating the local force over the full cylinder surface, i.e. we consider

(a)



(b)

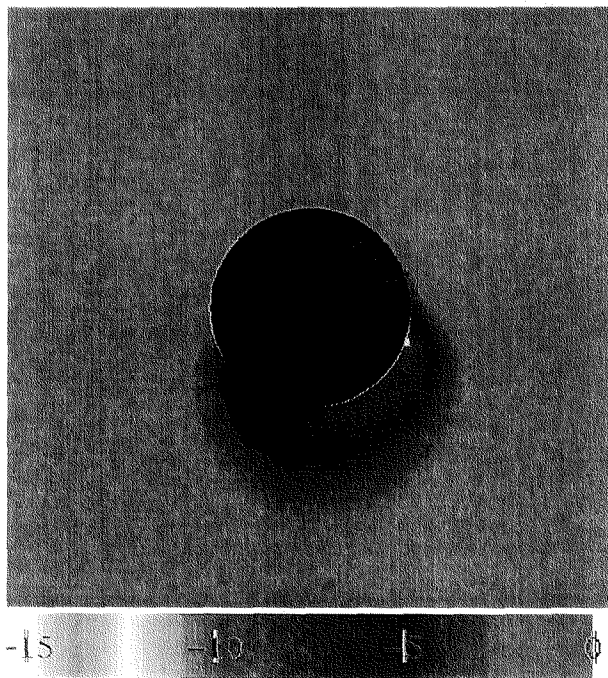


Figure 4.13: $Re=90$, $C_{suc}=1.0$: (a) streamwise velocity and (b) pressure fields in the region close to the cylinder.

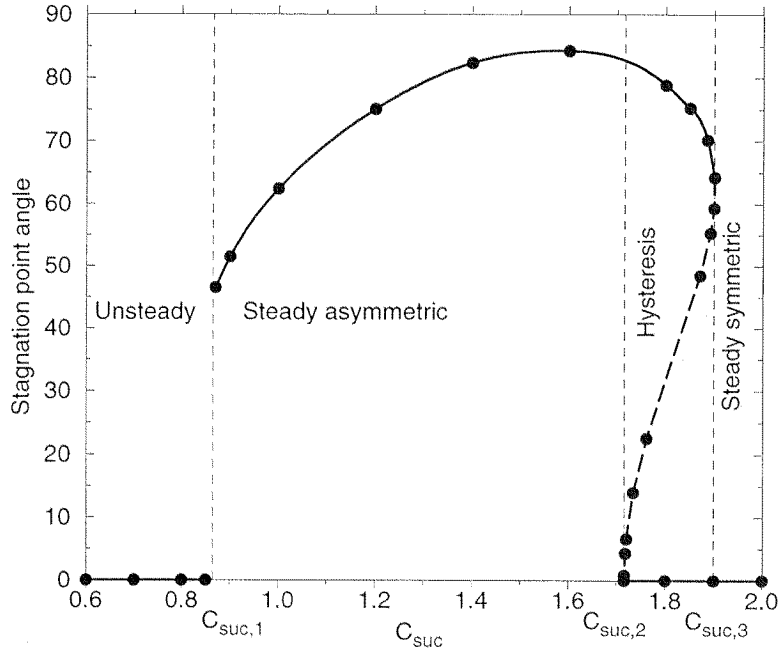


Figure 4.14: $Re=90$: deflection of front stagnation point (angle in degrees) with respect to the centerline, versus suction coefficient.

the case of a porous cylinder. Computed values at $Re = 90$ (pressure and viscous components, and total values) are presented in Figure 4.15 as functions of C_{suc} . Here, we report time-averaged values of the drag coefficient; since the time-averaged lift coefficient is zero in unsteady flow around a cylinder, the reported lift coefficient for (saturated) unsteady flow corresponds to its amplitude, i.e. half the difference between its maximum and minimum values.

As shown in Figure 4.15, the drag coefficient is minimal at the critical blowing flow rate ($C_{suc} = -0.145$). Compared to the uncontrolled flow, there is a decrease in drag coefficient by 14%. Both the pressure and viscous components increase monotonically with suction coefficient in the unsteady and in the steady (asymmetric and symmetric) regimes, with the pressure component contributing most in total drag. Around the transition from steady asymmetric to steady symmetric flow, the value of total drag coefficients exceeds that of the uncontrolled flow by an order of magnitude.

The lift coefficient is also monotonically increasing with C_{suc} , both in the unsteady and

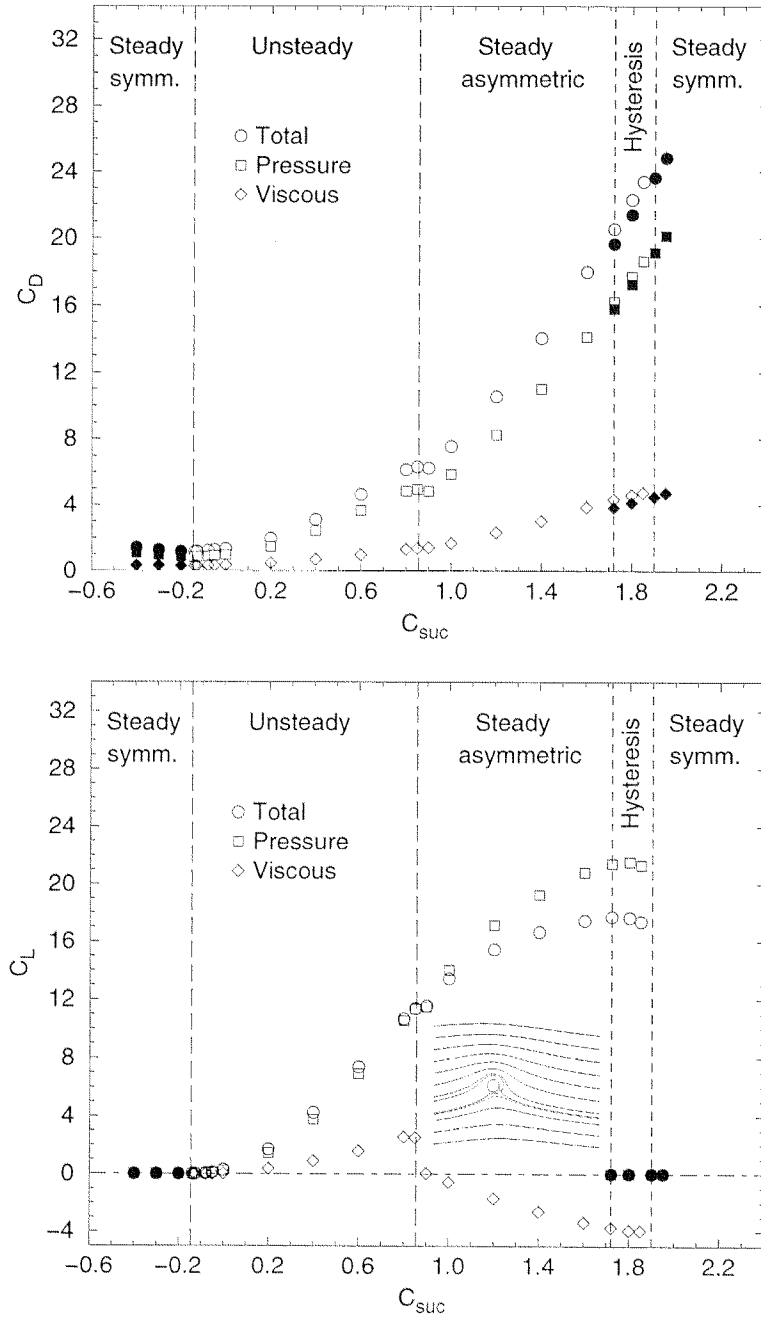


Figure 4.15: $Re=90$: drag and lift coefficients versus C_{suc} ; full symbols correspond to steady symmetric solutions. In the unsteady regime, the time-averaged value of the drag, and the amplitude of the lift coefficients are reported. Also sketched: flow structure (streamlines) in the asymmetric regime.

in the steady asymmetric flow regimes (Figure 4.15). In all cases, the pressure component is most significant. In the unsteady flow regime, due to the phase shift between the instantaneous pressure and viscous lift, the sum of the two component amplitudes does not equal the amplitude of total lift (see Figure 4.15). We emphasize the pronounced effect of suction on the lift coefficient: in the steady asymmetric regime, for example, the values of lift and drag coefficients are similarly high.

4.2 Feedback control method

The concept of the control strategy used to track unstable asymmetric solutions can be related to Landau's theory on non-linear hydrodynamic stability.

As already described in chapter (3), Landau proposed a dynamical model for the amplitude A of the dominant global mode about a steady ('base') flow (see equation 7, section 3.4). Depending on the sign of σ_r and l_r , four different cases can be classified. The combination $\sigma_r < 0$, $l_r < 0$, corresponds to a subcritical bifurcation. In this case, there exists a hysteresis regime, with a threshold value for the amplitude of initial perturbations $|A|_e = \sqrt{\frac{\sigma_r}{l_r}}$. If at $t = 0$ $|A| < |A|_e$, then $|A|$ decreases with time and tends asymptotically to zero. If at $t = 0$ $|A| > |A|_e$, then $|A|$ grows continuously and tends to infinity (to account for saturation and convergence to the second stable branch, higher order terms should be considered in the model equation (6) of chapter (3)). The evolution of $|A|$ as a function of time is sketched in Figure 4.16 for two different initial values, one smaller and one larger than $|A|_e$.

A combination of the Stuart-Landau equation (7) with a first order Taylor expansion of the growth rate σ_r around the critical value R_c of a system parameter R ,

$$\sigma_r = k(R - R_c) + O((R - R_c)^2), \quad (1)$$

yields the approximation $|A| \propto \sqrt{|R - R_c|}$ for the saturated amplitude $|A_{sat}|$. This result has been verified in this study for the variable $|V_A|$: the function $1.45\sqrt{C_{suc} - C_{suc,2}}$ accurately fits the unstable branch in the range $0 < |V_A| < 0.35$, with a maximal relative error of less than 1% at the computed points.

Thus, there should be a threshold value $|V_A|_e$ for the variable $|V_A|$, below which $|V_A|$ decreases and above which $|V_A|$ increases (after a short oscillatory transient, depending on initial conditions). This has been observed on flows evolving in the hysteresis regime at

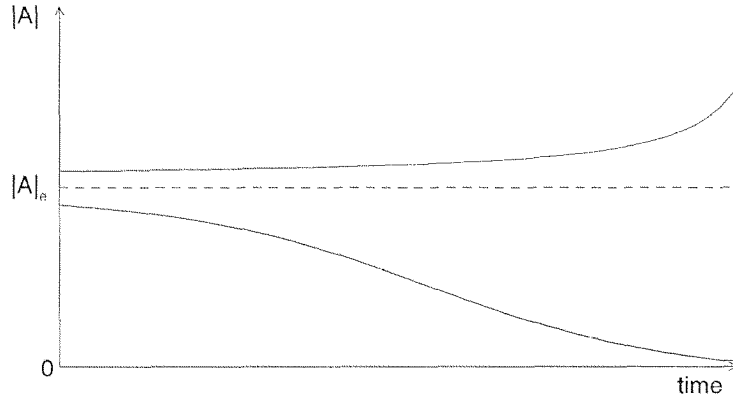


Figure 4.16: Sketch of the time evolution of the dominant global mode for two levels of initial perturbation, in the case of a subcritical bifurcation ($\sigma_r < 0$, $l_r < 0$).

various C_{suc} and $|V_A|$ levels. We have also observed that small disturbances superimposed on these flows always resulted in a short ‘chaotic’ transient of maximum 30 time units, followed by a very long and regular variation in $|V_A|(t)$. In general, shortly after the perturbation (for example due to a small jump in C_{suc}), the flow development is in very good approximation linear in time during at least $O(10^3)$ time units (see Figure 4.17, note the very slow system dynamics). At very large times, the flow approaches either the symmetric or the stable asymmetric solution and finally tends to it exponentially.

Based on the previous remarks, and assuming that the unstable branch joining the two stable branches at $C_{suc,2}$ and $C_{suc,3}$ is a bijection, we could derive a control strategy to track the unstable flow solutions. In feedback control, one needs to define a control goal, an actuator, and a measurement signal. We do not attempt to track unstable steady flows at fixed C_{suc} values, but rather to drive flows to an asymptotic unstable steady state, thus with $\frac{d|V_A|}{dt}=0$, by tuning C_{suc} at discrete times. Hence, our control goal is $\frac{d|V_A|}{dt} \rightarrow 0$ as $t \rightarrow \infty$, C_{suc} is used as actuator, and the sign of $\frac{d|V_A|}{dt}$ serves as feedback signal, which decides how the actuator must be updated to reach the fixed goal. Asymptotically the procedure gives $V_A \rightarrow V_{A,target}$ and $C_{suc} \rightarrow C_{suc,sought}$, both $V_{A,target}$ and $C_{suc,sought}$ being unknown a priori.

The very slow dynamics of the flow after the short irregular transient (caused by a small C_{suc} jump within the hysteresis regime) implies infinitesimal variation of all flow variables during $O(10)$ time units. The initial flow field for the control simulation thus verifies $V_{A,initial} \approx V_{A,target}$, and in general $V_{A,target}$ does not differ from $V_{A,initial}$ by more than 5%.

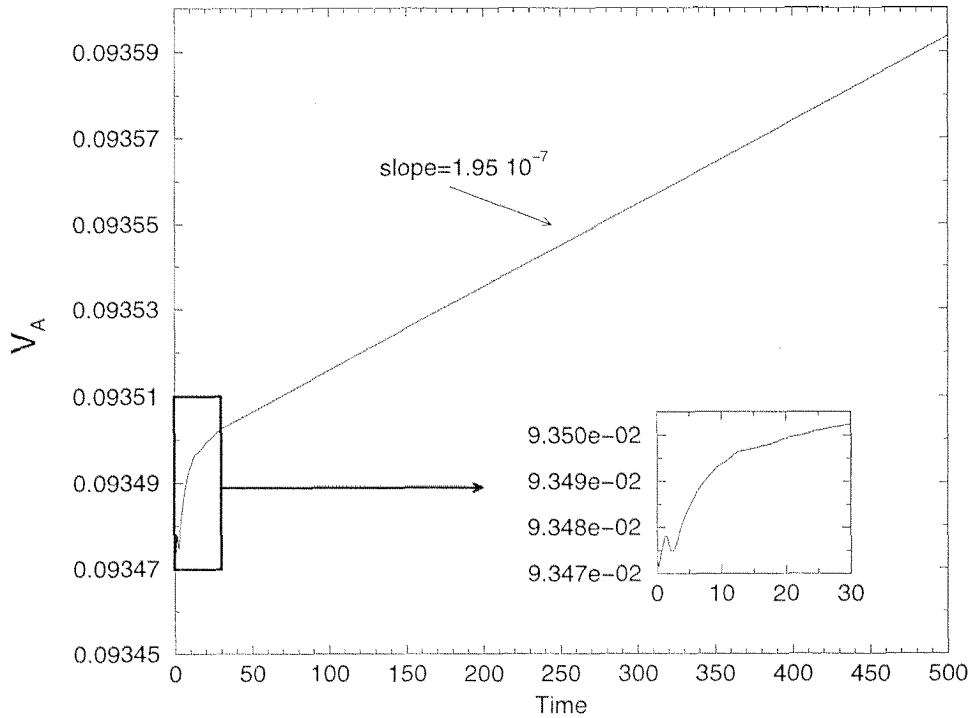


Figure 4.17: $Re=90$: time history of V-velocity at point A, indicating the response of a non-saturated flow to a small C_{suc} jump (from 1.7 to 1.72 at $t=0$).

This enables a rather good approximation of the value of the state variable V_A for the target flow, if the initial field is well chosen. A suitable initial condition can be an instantaneous field of a flow evolving from its unstable symmetric solution to its stable asymmetric solution at a suction coefficient just below $C_{suc,2}$, as V_A crosses the desired value for $V_{A,target}$. Doing so, the initial flow state is not fundamentally different from the ‘target’ unstable steady state, which also has the advantage of short and small amplitude initial oscillations. As initial suction coefficient, a random value can be taken in the range $[C_{suc,2}, C_{suc,3}]$, or, possibly, a better guess for $C_{suc,sought}$.

The control algorithm is sketched in Figure 4.18. Every 30 time units, the quantity $\frac{d|V_A|}{dt}$ is measured. If this quantity is positive, the flow is necessarily evolving above the unstable branch (Figure 4.11) towards the stable asymmetric solution corresponding to the current C_{suc} value; if $\frac{d|V_A|}{dt}$ is negative, then the instantaneous flow state corresponds to a point below the unstable branch, and the flow tends asymptotically to the stable symmetric solution. In the former case, C_{suc} must be increased to resist the growth of $|V_A|$; in the latter case C_{suc}

must be reduced. Note that the approach assumes that the unstable branch represents a one-to-one function from C_{suc} to $|V_A|$ (Figure 4.11).

Considering the case of decreasing $|V_A|$, at the first control iteration (after 30 time units), C_{suc} is decreased by 2% and its previous value is stored to define an upper limit $C_{suc,max}$, not to exceed in the following iterations. This is repeated until the first occurrence of increasing $|V_A|$, where the current C_{suc} value defines a lower limit $C_{suc,min}$, and the new value of C_{suc} is obtained by taking the mean of the current limits $C_{suc,min}$ and $C_{suc,max}$. At each subsequent iteration, depending on the sign of $\frac{d|V_A|}{dt}$, either $C_{suc,min}$ or $C_{suc,max}$ takes the current C_{suc} value, and the new value of C_{suc} is obtained by taking the mean of $C_{suc,min}$ and $C_{suc,max}$.

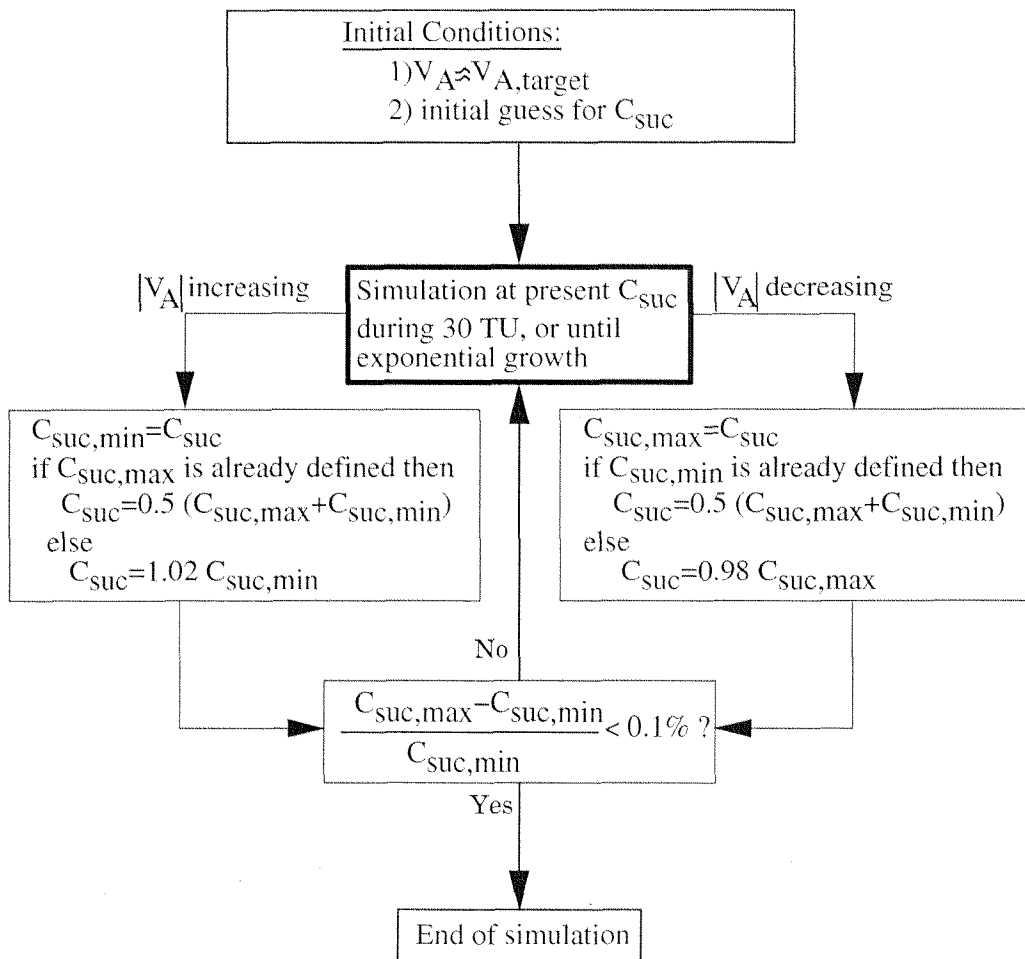


Figure 4.18: Control algorithm used to compute unstable asymmetric solutions.

As the flow approaches an unstable state after a few control iterations, small perturbations in C_{suc} naturally result in the growth of the dominant mode corresponding to this unstable solution. In this case, the exponential growth of the perturbation field usually manifests itself in less than 10 time units after implementing the control action. This suggested that the control algorithm could be improved, by updating C_{suc} more frequently than every 30 time units. It is important to note here that the dominant eigenmodes of the unstable steady solutions have zero frequency (see section on stability analysis), and thus do not oscillate around the base flow. In order to capture the exponential growth of an unstable mode, we perform an online curve fitting of $|V_A|(t)$ with the exponential function $y=A_0 + A_1 \exp(A_2t)$ on 35 values computed at equal intervals over the past 9 time units. As soon as the correlation coefficient between $|V_A|(t)$ and the fitting function is larger than 0.999, we consider that an unstable eigenmode mode is growing, and C_{suc} can be updated accordingly. The control action is thus updated either 30 TU (time units) after the previous control action (at the latest), or as soon as the growth of an unstable eigenmode is justified (earliest: 9 time units).

A further improvement to the controller has been implemented: instead of updating C_{suc} based only on the sign of $\frac{d|V_A|}{dt}$, we have also taken into account the absolute value of $\frac{d|V_A|}{dt}$, which allows for a more accurate approximation of $C_{suc,sought}$. Indeed, when the flow approaches a steady state, $|\frac{d|V_A|}{dt}|$ tends to zero. Therefore, the control algorithm has been improved as follows: the values of $\frac{d|V_A|}{dt}$ corresponding to the limiting values $C_{suc,min}$ and $C_{suc,max}$ are also stored ($(\frac{d|V_A|}{dt})_{min}$ and $(\frac{d|V_A|}{dt})_{max}$, respectively) at each control update, and C_{suc} is updated by the value which would correspond to $\frac{d|V_A|}{dt} = 0$, based on the linear interpolation between the points $(C_{suc,min}, (\frac{d|V_A|}{dt})_{min})$ and $(C_{suc,max}, (\frac{d|V_A|}{dt})_{max})$, see Figure 4.19.

Simulations were stopped when $C_{suc,min}$ and $C_{suc,max}$ differed by less than 0.1%. In all cases, the error made on $V_{A,target}$ was less than 0.1%. In Figure 4.20, the time history of $|V_A|$ is represented for the last time units of a simulation with control switched on. The corresponding time history of the controller output C_{suc} is represented on the same graph. The figure clearly illustrates the control process, with the update of C_{suc} depending on the slope of $|V_A|(t)$.

Intuitively, one could expect that results are more sensitive to spatial resolution on the unstable branch than on the stable branches; we have compared several points on this branch, obtained from simulations with 9×9 and 11×11 elemental resolution. The two branches obtained very well superimpose at four computed points. This further confirms the adequacy

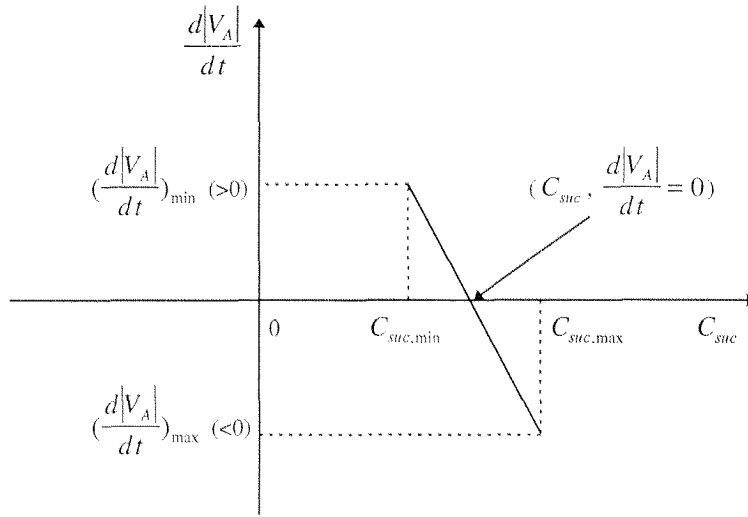
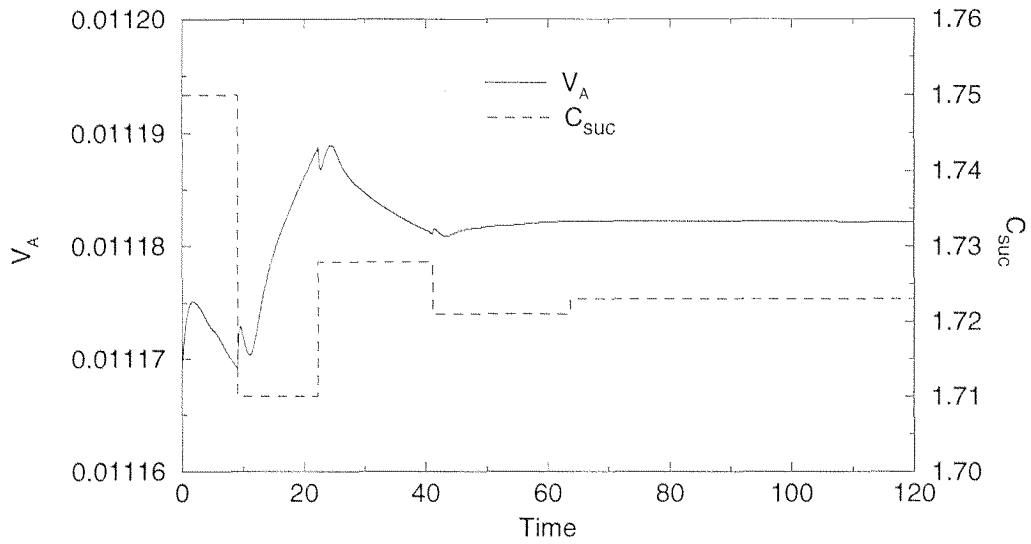


Figure 4.19: Sketch of the improved C_{suc} update. The “new C_{suc} ” corresponds to $\frac{d|V_A|}{dt}=0$, in the linear interpolation between $(C_{suc,min}, (\frac{d|V_A|}{dt})_{min})$ and $(C_{suc,max}, (\frac{d|V_A|}{dt})_{max})$.

of the 9×9 elemental resolution over the entire range of the system parameters investigated here. The computations of unstable asymmetric solutions with the control module have been performed with $TOL=10^{-8}$. Because of the very slow system dynamics near steady states (Figure 4.17), saturation of the flow variables was often obtained after few control iterations. To investigate the effect of tolerance in the velocity iterative solver, we have computed a few unstable points with $TOL=10^{-14}$. We find that these points also lie on the same curve as the ones computed with $TOL=10^{-8}$.

(a)



(b)

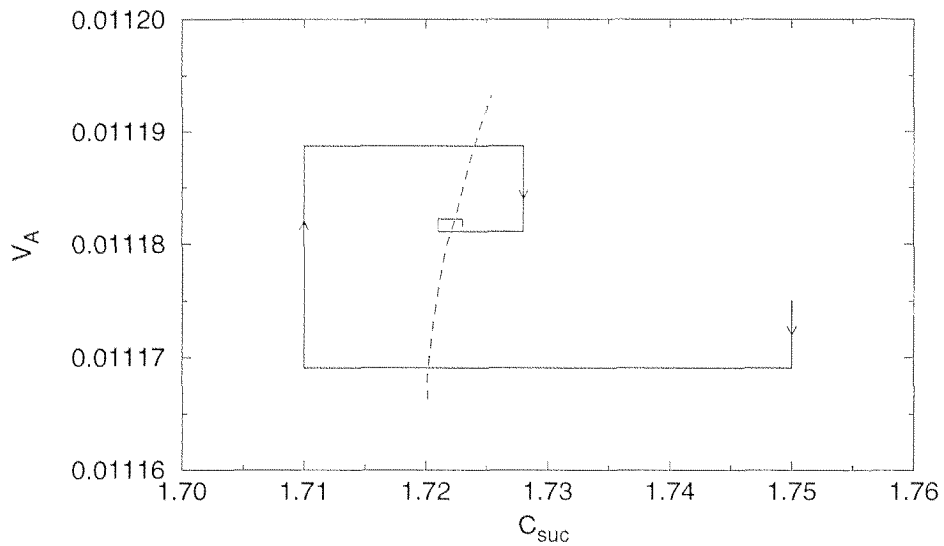


Figure 4.20: $Re=90$: (a) time histories of V -velocity at point A and C_{suc} , while the flow is subject to feedback control, with $V_{target}=0.011$, (b) Phase-portrait in the $C_{suc} - |V_A|$ plane (the dashed curve represents the unstable branch).

Chapter 5

Domain size and boundary conditions effects

5.1 Domain size effects

In contrast to *wall-bounded* flows, for which physical boundaries are well-defined, wake flows, like all *free shear flows*, must be computed in a truncated finite domain. The domain truncation is a supplementary source of errors, in addition to the other types of numerical errors present in numerical flow computation. (Note, however, that finite domain effects are also present in the experimental study of free shear flows). Evidently, increase of computational domain size results in reduced truncation errors, while increasing computer memory and CPU time requirements. All results of the previous chapter correspond to the domain presented in Figure 2.2. The size of this domain exceeds literature suggestions for the uncontrolled flow (Barkley and Henderson 1996), as we expect that the use of base mass transpiration affects the flow field many diameter lengths away from the cylinder.

In the case of uncontrolled flow around a cylinder, the deviation from an infinite (in cross-flow direction) domain is expressed in terms of the *blockage ratio*, D/DY , DY being the total domain width. Domain size effects vanish for very small blockage ratio values. In the case of flow controlled by means of base mass transpiration, the *suction ratio*, defined here as the ratio of suction flow rate to the domain total flow rate, may be a more appropriate parameter to express domain size (width) effects:

$$R_{suc} = \frac{Q_{suc}}{U_{\infty}DY} = C_{suc} \frac{D}{DY} \quad (1)$$

Note that $R_{suc} = 0$ is reached in the limits of either infinite domain width, or uncontrolled flow (where domain size recommendations are available (Barkley and Henderson 1996)). The results presented in the previous chapter correspond to suction ratio values up to 0.038 (domain width is $68D$, maximum suction coefficient value is 2.6).

To investigate the effects of domain size on computational results, a number of computational domains of different inflow and outflow length, and width, have been used. The main domains used are sketched to scale in Figure 5.1, including characteristic names and total element numbers. The cylinder is also represented. The domain dimensions are summarized in Table 5.1. Domains ‘OUT’, ‘W’, ‘L’ and ‘LW’ were constructed by adding elemental rows and columns at the boundaries of the basic domain ‘MAIN’ presented in Figure 2.2, i.e. the spatial resolution of the coinciding part is the same in all cases. Domains ‘XL’ and ‘XLW’ have comparatively bigger elements in the region defined by $X < -30$ and $-1.5 < Y < 1.5$.

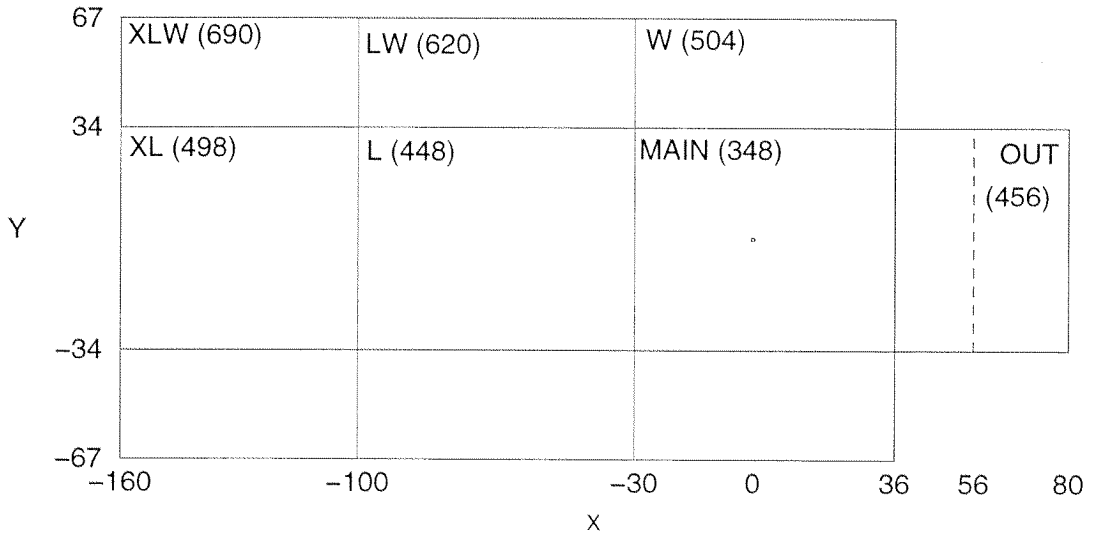


Figure 5.1: Computational domains used, and corresponding numbers of elements. The cylinder is also represented (to scale).

At fixed parameter sets (Re, C_{suc}) , we compare the computed values of flow frequency - equivalently: period- for different flow domains. We also compare the critical values obtained

	OUT	MAIN	W	L	LW	XL	XLW
DX_{IN}	30	30	30	100	100	160	160
DY	68	68	134	68	134	68	134
DX_{OUT}	80	36	36	36	36	36	36

Table 5.1: Domain names and characteristic dimensions in terms of diameter lengths: DX_{IN} and DX_{OUT} stand for the distances from the cylinder center to the inflow and outflow boundaries, respectively; DY stands for the total domain width.

for one of the system parameters (Re or C_{suc}) when fixing the value of the other system parameter.

5.1.1 Effects on shedding period

The period of vortex-shedding is a sensitive parameter to the domain width. Decreasing DY results in a local increase of the Reynolds number close to the cylinder due to local velocity increase (so that total mass is conserved), and thus, in an increase of the Strouhal number (see Figure 3.2). This is known as the ‘blockage’ effect. Flow periods obtained with different computational domains are compared at representative parameter sets (Re, C_{suc}). The corresponding points in the parameter plane are represented by the crosses in Figure 5.2; here the critical curve separating steady and unsteady flow regimes corresponds to domain ‘MAIN’. Results are reported in Table 5.2. At a parameter set ($Re=90, C_{suc}=0.85$) corresponding to flow conditions particularly sensible to domain size (in terms of oscillations period and stability state), the difference in flow period between ‘MAIN’ and ‘OUT’ is about 4%. The difference in flow period between ‘OUT’ and a domain with a shorter outflow distance ($DX_{out} = 56$, i.e. 28 diameters shorter than ‘OUT’, and 20 diameters longer than ‘MAIN’) falls below 1%. The outflow boundary only has a very small effect on the flow period in the unsteady regime, for the entire range of (Re, C_{suc}) corresponding to unsteady flow. The discrepancies between periods obtained with ‘MAIN’ and ‘OUT’ are always below 5% (see Table 5.2). The discrepancies fall below 1%, when comparing the results obtained with ‘OUT’ and a domain with an outflow distance of $DX_{out} = 56$. We conclude that the outflow length has a negligible effect on the period of unsteady flows.

In contrast to outflow length, the effect of inflow length and domain width on the flow

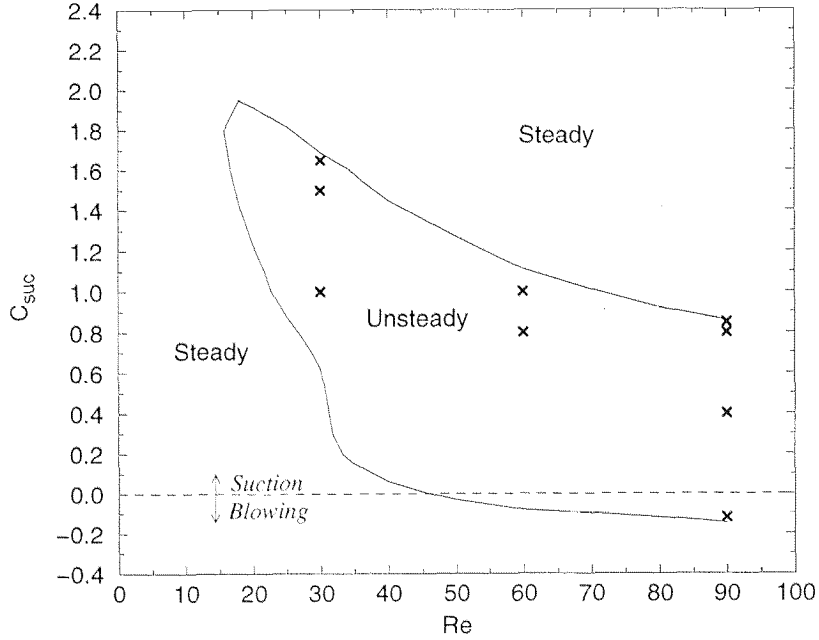


Figure 5.2: Boundary of unsteady flow regime in the parameter plane (Re , C_{suc}). Parameter sets (crosses) chosen for frequency comparison tests are also indicated.

frequency and stability can be very substantial. According to our results, the choice of domain width can drastically affect flow frequencies and fluctuation amplitudes, close to the transition from unsteady to steady asymmetric flow. At ($Re=90$, $C_{suc}=0.85$), for example, the shedding period corresponding to domain ‘XLW’ is about 5 times larger than the period corresponding to domain ‘XL’ (see Table 5.2). At $C_{suc}=0.80$, the difference falls to 5%, and becomes negligible at $C_{suc}=0.40$.

In addition to the equality of the flow frequency at ($Re=90$, $C_{suc}=0.4$) for all grids used, the phase space plot of velocity components (U, V) at points A and E confirms that the flow dynamics is identical for domain sizes from ‘MAIN’ to ‘XLW’ at this suction level (see Figure 5.3). The huge period of oscillations ($T=726$) found with the largest domain at ($Re=90$, $C_{suc}=0.85$) suggests that, in the limit of infinite flow domain, the transition to steady asymmetry may be viewed as a convergence to a state of zero shedding frequency.

Domain width can also (slightly) affect the precise position of the limiting curve: for $C_{suc}=0.85$, the asymptotic flow state is unsteady with ‘MAIN’, and steady asymmetric with

Re	C_{suc}	MAIN	W	XL	XLW	OUT
90	0.85	107	Steady	150	726	103
90	0.80	72.8	76.3	87.1	91.6	71.9
90	0.40	12.1	12.1	12.1	12.1	12.1
90	-0.12	7.56	7.59	7.59	7.66	7.55
60	1.00	71.01	73.5	81.5	85.0	70.1
60	0.80	34.0	34.0	33.1	33.1	34.0
30	1.65	139	178	153	178	132
30	0.65	13.65	13.65	13.68	13.68	13.66

Table 5.2: Flow oscillation period at different parameter sets.

‘W’.

Interestingly enough, we find that inflow length can also drastically affect shedding frequencies, in the vicinity of the critical curve in the suction regime. For all Reynolds numbers used in this test, the shedding period is dramatically increased near the transition to asymmetry, for increasing domain size (from ‘MAIN’ to ‘XLW’). On the other hand, the dynamics of flow controlled by blowing appears rather unaffected by the domain sizes used here. For example, at $Re=90$ and $C_{suc}=-0.12$ (a point close to the critical curve in the parameter plane), the maximum difference in flow period for all combinations of domains used, is less than 2%.

In summary, domain size can significantly affect the shedding period, especially the inflow length and domain width.

5.1.2 Effects on flow transitions

In the present subsection, we investigate the effect of domain size on flow transitions. We perform a number of tests to check the influence of the domain size on the location of the critical curve delimiting the region of unsteady flow. We find a maximum discrepancy on the critical suction coefficient delimiting the unsteady regime of about 6%; this occurs at $Re=30$, near the triple point (see Figure 4.1), in comparing ‘MAIN’ to all other domains. The discrepancy decreases at lower and higher Reynolds numbers, it is about 2% at $Re=20$ and for $Re \geq 40$. We conclude that the curve delimiting the unsteady flow regime is accurately

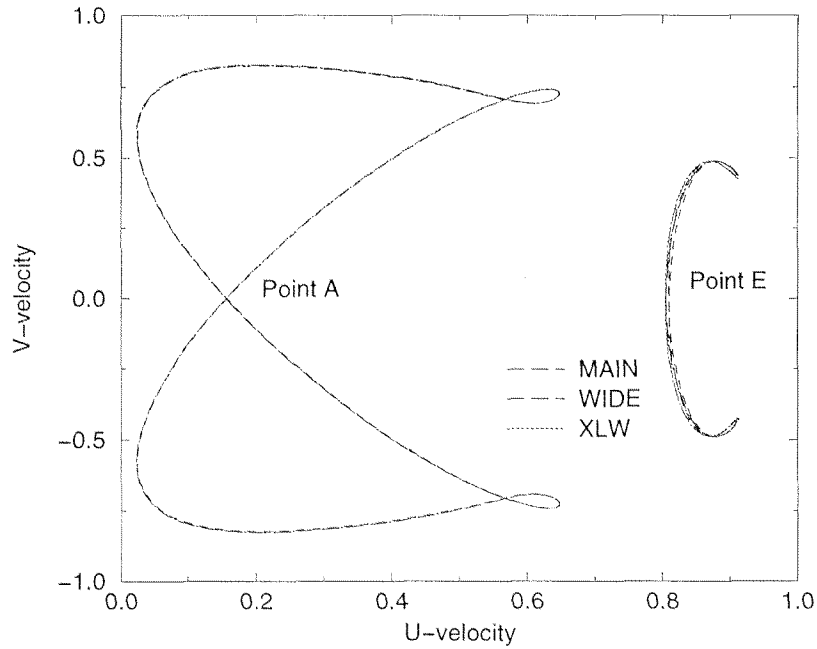


Figure 5.3: $Re=90$, $C_{suc}=0.4$: phase space plot at points A and E: V-velocity vs. U-velocity.

sketched in Figure 4.1, and only slightly depends on the domain size in the region around the triple point.

We now emphasize on the transition between the steady symmetric and steady asymmetric regime at low Reynolds numbers and high C_{suc} values. This transition corresponds to a supercritical bifurcation. Thus, there is no hysteresis, and the amplitude of saturated perturbations at a fixed point continuously grows with the critical parameter (Re , or C_{suc}), as this is increased above the critical value. Figure 5.4 presents a bifurcation diagram, similarly as Figure 4.11; here the amplitude $|V_A|$ is represented versus the Reynolds number, at a fixed C_{suc} value ($C_{suc}=2.0$). The graph shows that the critical Reynolds numbers obtained with the smallest ('MAIN') and the largest ('XLW') domains differ by less than 2%. We can conclude that this bifurcation is accurately represented on Figure 4.1 for the infinite problem, as it is not influenced by the extension of the domain 'MAIN' in all directions.

The last transition studied in detail in the previous chapter was the subcritical bifurcation from steady asymmetric to steady symmetric flow; we will show that it depends strongly on inflow length and domain width. Figure 5.5 represents $|V_A|$ versus C_{suc} in the steady regimes

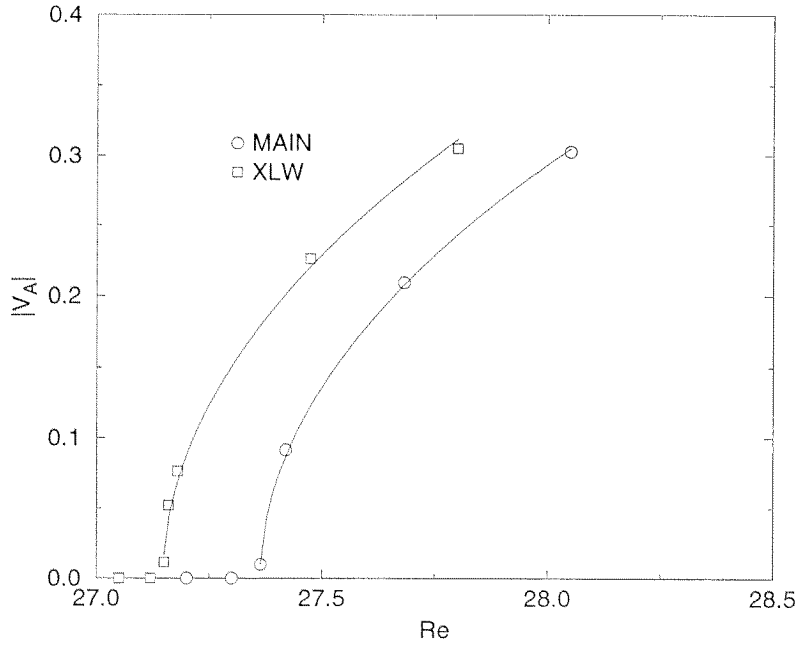


Figure 5.4: $C_{suc}=2.0$: bifurcation diagram for the transition from steady symmetric to steady asymmetric flow: V_A versus Re .

at $Re=90$ for six different domains. All these domains have the same outflow length. They constitute all possible combinations from three different inflow and two lateral boundary locations. We observe that the effects due to inflow length are very strong. Note that, at a given C_{suc} value, the suction ratio corresponding to the wide domains ('W', 'LW', and 'XLW') is about half the ratio of the thin domains ('MAIN', 'L', 'XL'). Irrespective of the influence of suction ratio, we find that the difference in the critical suction coefficient $C_{suc,2}$ (and also $C_{suc,3}$) between the two domain types is mainly influenced by DX_{IN} . In particular, the difference in $C_{suc,2}$ between the thin and wide domains increases with DX_{IN} as follows: it is about 2% between 'MAIN' and 'W', 5% between 'L' and 'LW', and 8% between 'XL' and 'XLW' (see Figure 5.5). Moreover, with increasing DY , the critical suction coefficients increase for small DX_{IN} values (compare 'MAIN' and 'W'), whereas they decrease at higher DX_{IN} values. We can therefore not conclude on the effect of DY independently of DX_{IN} , but can confidently assess that the transition mainly depends on DX_{IN} , which acts in this case as a limiting factor. Indeed, it seems that low values of DX_{IN} can limit the effects

caused by increased DY values.

As shown in Figure 5.6, the critical suction coefficient values $C_{suc,2}$ and $C_{suc,3}$ increase very significantly with inflow length. Thus, at high values of DX_{IN} , the corresponding critical curves exceed the range of Figure 4.1 ($C_{suc} > 2.6$). In spite of the use of the very long inflow length of 160 diameters, much longer than in any literature simulations of cylinder flow we are aware of, we are still unable to assess critical suction coefficients, for the (higher Reynolds number) transition from steady asymmetric to steady symmetric flow, in the limit of infinite flow domain. This is clearly indicated in Figure 5.6, where the critical values $C_{suc,2}$ and $C_{suc,3}$ are plotted versus DX_{IN} , for $DY=34$ and $DY=67$, at $Re=90$. This particularly strong effect of the inflow length on the subcritical bifurcation can be explained by the fact that the inflow boundary condition imposes a symmetric velocity profile ($U = 1, V = 0$). At a given suction coefficient, decreasing DX_{IN} tends to impose a symmetric flow pattern closer to the cylinder, and therefore acts in favour of transition to a symmetric steady state. On the other hand, increasing DX_{IN} tends to delay transition to symmetry, as shown in Figure 5.5. Figure 5.7 shows the V -velocity profile versus y -coordinate at $X = -30$, of the saturated asymmetric flow obtained with ‘XLW’. At this streamwise coordinate, the V -velocity on domain ‘MAIN’ is imposed as a boundary condition, and is equal to zero; this is qualitatively different from the profile in ‘XLW’, which takes a non-negligible value close to $-0.04U_\infty$ at the centerline. The comparison illustrates the strong effect of inflow length on the symmetry properties of the flow, which can explain the fact that asymmetric solutions are more stable in longer domains.

5.2 Boundary conditions effects

As a final test, we check the effect of different velocity boundary conditions on the computed flow fields. All computations are performed using the smallest computational domain ‘MAIN’, for which different boundary conditions are expected to affect the flow field most. Three new types of velocity boundary conditions are implemented:

- (a) Symmetry on the lateral boundaries.
- (b) Periodic boundary conditions for the two lateral boundaries.
- (c) Potential flow solution for the inflow and lateral boundaries; due to the relative large domain dimensions, this is very close to the standard freestream velocity boundary condition.

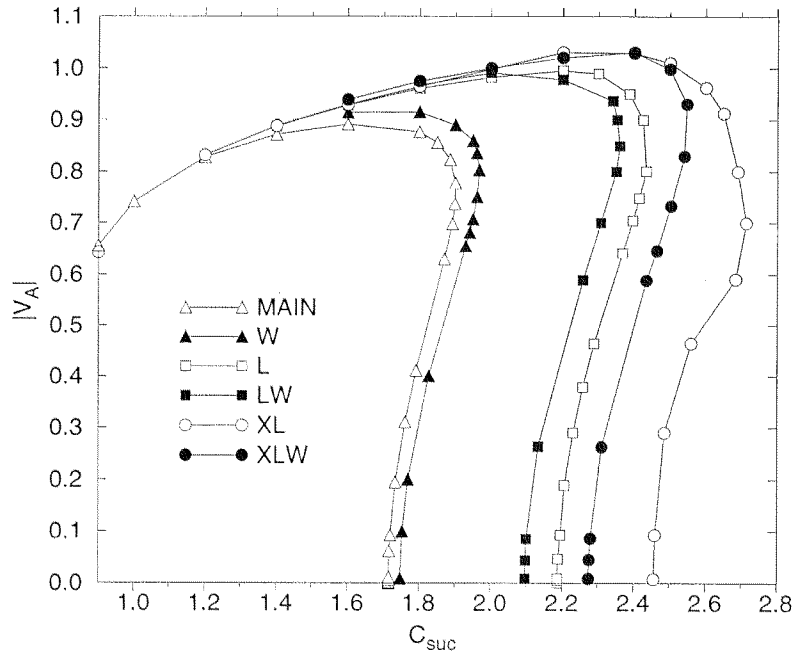


Figure 5.5: $Re=90$: Bifurcation diagram: $|V_A|$ versus C_{suc} .

We perform several computations at high suction coefficient values. We find that the sub-critical bifurcation is very slightly affected by the new boundary conditions. In Table 5.3, we report the values of the critical suction coefficients $C_{suc,2}$ and $C_{suc,3}$ computed with the standard and the three different boundary conditions. Here, we also report the values obtained with the domain ‘OUT’ and the standard boundary conditions, to confirm that the outflow length also has a negligible effect on $C_{suc,2}$ and $C_{suc,3}$.

Clearly, all boundary conditions implemented have practically no effect on the flow transitions. This has been further verified for various domain sizes. Hence, regarding the sub-critical bifurcation, the problem of domain size dependency is still present, irrespective of the boundary conditions.

Another form of velocity boundary condition, with the advantage of corresponding CPU savings, has been proposed and used by Hannemann and Oertel (1989), for the simulation of the wake behind a flat plate. They conducted computations in two steps using two different domains: one full domain, with the plate centered on the central (symmetry) axis, and one ‘half domain’, corresponding to half of a full domain, truncated at the central axis,

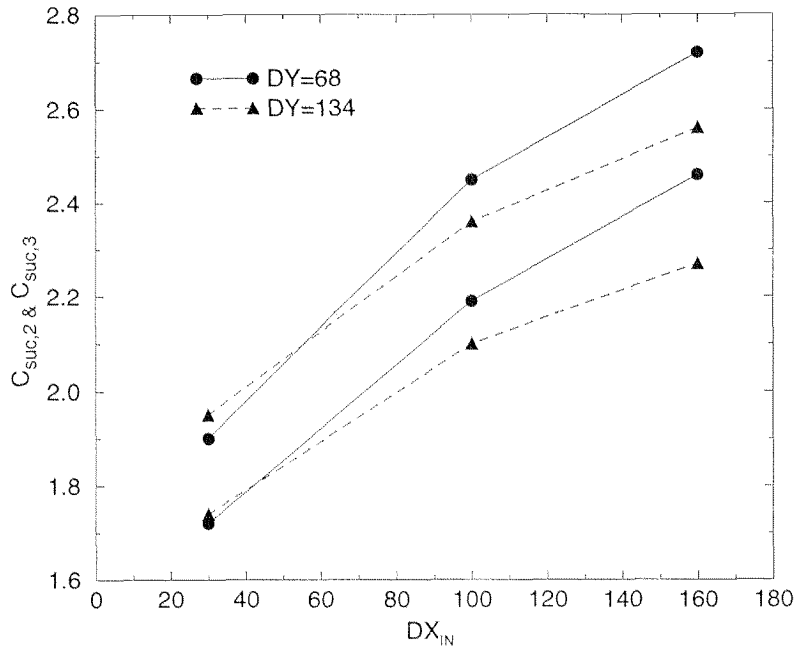


Figure 5.6: $Re=90$: critical suction coefficients $C_{suc,2}$ and $C_{suc,3}$ versus DX_{IN} .

and further extended upstream and laterally, in comparison to the full domain. They first computed the steady symmetric flow on the ‘half domain’, implementing free stream velocity on the inflow and lateral boundaries, and a symmetry boundary condition on the centerline. After convergence to the steady symmetric solution, they restarted the computation on the full domain, using the velocity computed with the ‘half domain’ as boundary condition at the new inflow and lateral boundaries. The two discretized domains may have the same order of nodes, while the flow field far from the plate end is better approximated by the steady symmetric solution than by the free stream velocity. Although we have not tested this procedure, we can assess that it would not have been effective for our simulations. Indeed, we have extended our standard domain far upstream and laterally from the cylinder, without coming up with any asymptotic behaviour of the subcritical bifurcation. The procedure proposed by Hannemann and Oertel is in essence equivalent to increasing domain size without increasing the computational cost. In extending ‘MAIN’ to ‘XLW’, we have followed the same basic idea, while also increasing CPU requirements. Also note that the full domain boundary conditions of Hannemann and Oertel are symmetric with respect to the centerline.

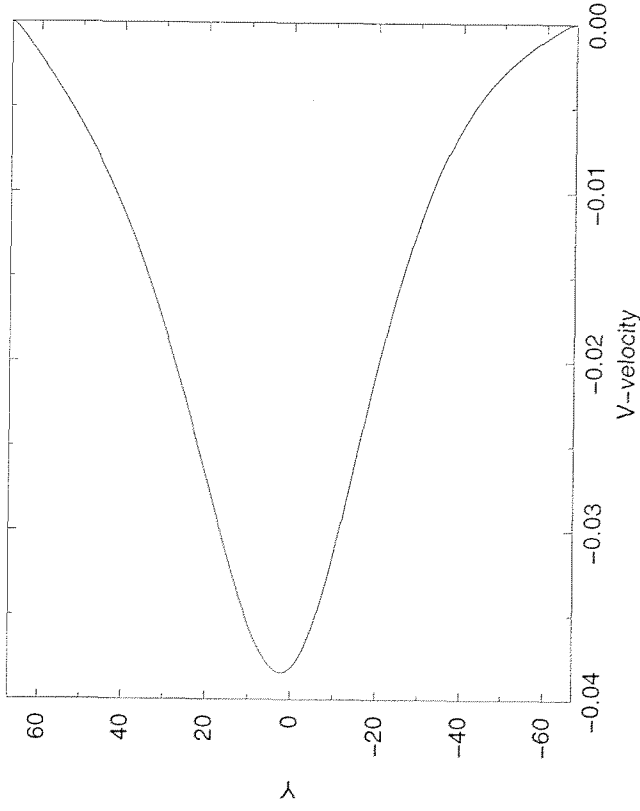


Figure 5.7: $Re=90$, $C_{suc}=1.8$: V-velocity profile along the y axis at $X = -30$ in the ‘XIW’ domain.

As previously indicated, imposition of symmetric boundary conditions can be the cause for the return to symmetric flow structure at high suction coefficient values.

5.3 Summary

In this chapter, we have investigated the effects of domain size and boundary conditions on the computed flow fields. According to our results, in the unsteady flow regime, discrepancies in flow frequencies obtained with different domain sizes are maximum close to the critical curve. Both the increase of the upstream distance DX_{IN} and of the domain width DY increase the non-dimensional flow period. The transition from steady asymmetric to steady symmetric flow is much affected by domain size, in particular by inflow length. The domain parameter with negligible influence on flow stability and dynamics is the outflow length, if it is longer than 36 non-dimensional units.

Moreover, no evidence of the existence of the transition from steady asymmetric to steady symmetric flow at infinite domain can be deduced from the present computations, performed

	MAIN	Potential	Symmetry	Periodicity	OUT
$C_{suc,2}$	1.72	1.72	1.72	1.72	1.71
$C_{suc,3}$	1.90	1.89	1.89	1.90	1.89

Table 5.3: Critical suction coefficient values obtained with the domain ‘MAIN’ and four different types of velocity boundary conditions on the lateral boundaries (the velocity imposed at the inflow boundary is the free stream velocity, if not otherwise stated): free stream, potential (also at the inflow boundary), symmetry boundary condition, and periodic boundary conditions. Also reported: values obtained with the domain ‘OUT’, whereby the free stream boundary condition is applied.

with very large, but still finite domains. The earlier transition to steady symmetric flow at shorter inflow domain lengths can be explained by the fact that inflow boundary condition imposes a symmetric velocity profile ($U = 1, V = 0$); shorter inflow lengths impose a symmetry condition closer to the cylinder, and this favours transition to a steady symmetric flow state.

If the above subcritical bifurcation is actually present at infinite flow domain, one can expect that the two critical curves separating steady symmetric and asymmetric flow states (see Figure 4.1) either have a vertical asymptote as C_{suc} tends to infinity, or join forming a single curve. In the latter case, there would exist a threshold value for C_{suc} , above which all asymptotic flow states are steady symmetric. We believe however that the subcritical bifurcation is a consequence of domain truncation, and thus is not present in the limit of infinite flow domain. At present, for a given Reynolds number, we can merely identify a suction coefficient value below which our results are insensitive to domain size (for example, at $Re = 90$, results are insensitive to present domains for $C_{suc} \leq 1.5$, see Figure 5.5).

Note that, in all simulations, while the range of Reynolds numbers is arbitrarily limited to $Re \leq 90$, C_{suc} is, instead, less than 2.6 for reasons related to the numerical stability constraint. At $C_{suc}=2.0$ and $Re=90$, a time step as low as $\Delta t=0.0005$ is necessary to satisfy numerical stability, which is much smaller than the value $\Delta t=0.01$ used for the uncontrolled flow. Given the very large integration times, even higher suction coefficients than the ones already used would result in prohibitively expensive simulations.

Implementation of different types of boundary conditions has shown that the flow transitions are practically insensitive to boundary conditions, for the domain sizes used in the

present work. Indeed, it appears that the subcritical bifurcation is always present for finite domains, and depends strongly on domain size.

Seite Leer /
Blank leaf

Chapter 6

Stability analysis

To characterize in more detail the flow stability properties in the various regimes, we have performed global stability analysis calculations at $Re = 90$, for a wide range of suction coefficient values. Global stability analysis can also serve as an additional test for DNS results.

In this chapter, we first present the numerical algorithm utilized by the stability code, which was kindly provided to us by R. Henderson and D. Barkley. Then, we report stability analysis results, at $Re=90$.

All types of steady solutions have been analyzed: symmetric (stable and unstable), strongly asymmetric (stable), and slightly asymmetric (unstable) flows within the hysteresis regime. The steady symmetric base flows have been obtained with time-dependent simulations on half the domain, implementing a symmetry boundary condition on the centerline. The unstable slightly asymmetric flows within hysteresis have been computed by means of the feedback control presented in section 4.2.

To perform global linear stability analysis, the discretized Navier-Stokes equations must be linearized about a steady base flow U . This yields a linear dynamical system for the evolution of small disturbances u' superimposed on the steady base solution U , that can be expressed by means of a linear operator A_U , as follows:

$$\frac{du'}{dt} = A_U \cdot u' \quad (1)$$

A primary task in linear stability analysis consists in finding the leading eigenmode (i.e. the one corresponding to the largest growth rate) of the steady solution U , or, equivalently,

the leading eigenpair (eigenvalue, eigenvector) of the linear operator A_U . Indeed, in the frame of linear stability theory, infinitesimal disturbances superimposed on the steady solution evolve exponentially at the rate corresponding to the eigenvalue with the largest real part, $s = \sigma_r + i\sigma_i$, which is therefore of particular interest. If the leading eigenvalue, now also referred to as the global linear frequency, has a positive real part, then the steady flow solution is unstable, and infinitesimal disturbances increase at a growth rate of σ_r , while oscillating with a frequency equal to $\frac{\sigma_i}{2\pi}$; for negative values of σ_r , disturbances decay with the corresponding values of decay rate and frequency.

To reduce the high computational effort in solving the full eigenvalue problem $A_U X = \lambda X$, since only the leading eigenmode is sought, the stability code used exploits the efficiency of an iterative Krylov method (Edwards et al. 1994) to accurately compute the dominant mode. A series u_n is constructed as follows:

$$u_{n+1} = A_{U,T} \cdot u_n, \quad n \geq 0, \quad (2)$$

starting from an initial guess u_0 for the dominant eigenmode. $A_{U,T}$ is the integration operator associated with the linear system (1) over a sampling period T :

$$A_{U,T} \cdot u'(t) = u'(t) + \int_t^{t+T} A_U \cdot u' dt; \quad (3)$$

In equation (2), u_n actually represents the solution of (1) at time $t=nT$, with the initial condition u_0 . From this series of perturbation fields, a series of Krylov subspaces $X_k = [u_k, u_{k+1}, \dots, u_{k+M-1}]$ of dimension M is constructed, which can also be defined recursively:

$$X_0 = [u_0, u_1, \dots, u_{M-1}]$$

$$X_{n+1} = A_{U,T} \cdot X_n, \quad n \geq 0, \quad (4)$$

$$(5)$$

Hence, only a single matrix-vector operation is necessary to compute X_{n+1} from X_n . The eigenpairs of X_n tend to those of A_U as $n \rightarrow \infty$, convergence being fastest achieved for the dominant eigenpair. The series of the dominant eigenvalue λ_n and the dominant eigenmode e_n of X_n is considered to accurately approximate the leading eigenvalue and eigenmode of

A_U when the residual $r=||A_U \cdot e_n - \lambda_n e_n||$ falls below 10^{-5} . In all cases, a Krylov subspace dimension $M=40$ appears sufficient to reach this level of accuracy. This is consistent with the stability calculations of Taylor-Couette flow reported in Edwards et al. (1994); they obtained fast convergence with a subspace of dimension 30. The sampling period T depends on the base flow and has been chosen in the range $[0.5, 5]$: for base flows characterized by very low growth rates, T should be high enough to give the eigenmode enough time to grow, whereas for high growth rates, T should be chosen small enough so that the series u_n does not get too high values due to fast eigenmode growth. In general, for $M=40$, convergence is already achieved with the first computed Krylov subspace X_0 .

As a validation test, we compare stability analysis results to Stuart-Landau equation coefficients, obtained by analyzing DNS data, in terms of global growth rates and linear temporal frequencies. In Table 6.1, we present the global linear frequencies (growth rates and temporal frequencies) computed by global stability analysis at $Re=50$ and $Re=60$, for uncontrolled flow. Results corresponding to the Stuart-Landau model are also reported. At both Reynolds number values, the agreement is excellent.

	$\sigma_r(SL)$	$\sigma_r(SA)$	$\sigma_i(SL)$	$\sigma_i(SA)$
$Re=50$	0.0140	0.0140	0.742	0.742
$Re=60$	0.0483	0.0481	0.750	0.751

Table 6.1: Uncontrolled flow: global linear growth rates and temporal frequencies, based on the Stuart-Landau model (SL), and on stability analysis calculations (SA).

It has been shown for the uncontrolled cylinder wake (Barkley and Henderson, 1996) that computation of the eigenmodes can be performed with equal accuracy on a much smaller domain than the one used for base flow computation, because these eigenmodes vanish rather close to the cylinder. We have verified this with few test-calculations. At $Re=90$ and $C_{suc}=0.0$, the steady base flow computed on ‘MAIN’ has been strongly truncated onto a smaller domain, with the following dimensions: $DX_{IN}=4$, $DY=4$, $DX_{OUT}=4$. Global stability analysis performed both on the small domain and on ‘MAIN’ yielded very close values for the growth rate, 0.110 and 0.109, respectively. Nevertheless, all stability calculations have been performed with the same grid and resolution (9×9) used for the associated base flows. Several resolution tests at various suction coefficient values have been performed using 11×11 elemental resolution in both base flow and stability calculations, and verified the

accuracy of 9×9 resolution. For example, at $Re=90$, $C_{suc}=1.76$, the global growth rates corresponding to the unstable asymmetric steady flow (chosen for its potential sensitivity to spatial discretization) computed with 9×9 and 11×11 elemental resolution are 0.000405 and 0.000417 respectively, and thus differ by only 3%.

We now present stability analysis results obtained with the domain ‘MAIN’, and compare them with some results obtained with the largest domain ‘XLW’. In Figure 6.1, global linear growth rates and frequencies corresponding to symmetric base flows at $Re = 90$ are presented, for a wide range of C_{suc} . The non-linear frequencies in the unsteady regime are also presented. First, we note that the suction coefficients at which the symmetric steady flows become unstable ($\sigma_r=0$) practically coincide with the critical values found by DNS (marked by the vertical dashed lines).

We emphasize now on the unsteady regime and the transition from steady symmetric to unsteady flow. Up to $C_{suc}=0.2$, the linear frequency remains at a constant level, while the growth rate varies linearly with C_{suc} , which is consistent with the first order approximation of σ_r near the critical value, used in the Stuart-Landau model. Note that, as expected, as C_{suc} approaches its critical value (≈ -0.145), the non-linear frequency (of the limit cycle) tends to the linear frequency.

The linear variation in both the growth rate and linear frequency stops at $C_{suc} \approx 0.3$. Further increasing C_{suc} only slightly increases σ_r up to $C_{suc}=0.6$, while σ_i drastically decreases from $C_{suc}=0.3$ to 0.6, where it becomes zero. We believe that the sudden modification in the shape of the σ_r versus C_{suc} curve for $C_{suc} \geq 0.3$ is due to a less parallel flow in the near wake. Leu and Ho (2000) conducted a similar experience in their control studies of wake flow produced by the merging of two boundary layers.

Around $C_{suc}=0.6$, the growth rate starts increasing again, while the linear temporal frequency remains at a zero value. Still in the unsteady regime, it is interesting to note that the linear and non-linear frequency start deviating from each other not too far from the critical suction coefficient. This indicates a substantial difference in the structure of linear and saturated global modes. The difference is even more pronounced in the C_{suc} range $[0.6, 0.855]$, where the linear mode is asymmetric (non-oscillatory: $\sigma_i = 0$), while the non-linear state is oscillatory ($St > 0$) and intermittent. In Figure 6.2, the structure of the oscillatory dominant eigenmode corresponding to the base flow at $C_{suc}=0.4$ (a), and of the asymmetric eigenmode corresponding to the base flow at $C_{suc}=0.8$ (b) is illustrated, in terms of velocity

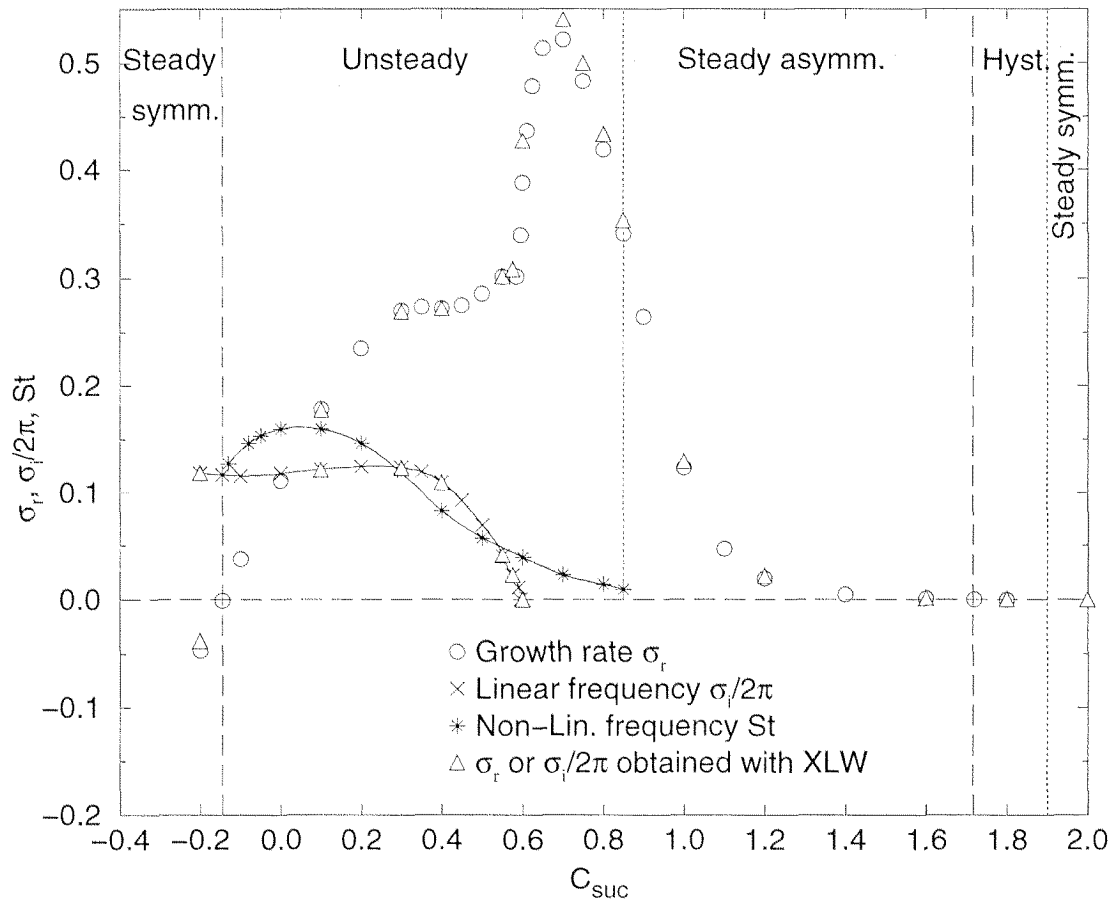


Figure 6.1: $Re=90$: global growth rate (σ_r), linear frequency ($\sigma_i/2\pi$), and non-linear frequency (St), versus suction coefficient C_{suc} , for symmetric base flow solutions. Data obtained with the domain 'MAIN', unless otherwise stated.

components isocontours. Spatial oscillatory patterns are clearly identified at $C_{suc}=0.4$, with maximum mode amplitudes rather close to the cylinder base; this is also the case for the non-linear saturated flow state at the same parameter set (see Figure 4.4). At $C_{suc}=0.8$, we find a pronounced asymmetry of the linear eigenmode, also very close to the cylinder base. At a higher suction coefficient, $C_{suc}=1.0$, the streamline pattern (see Figure 4.12) shows that flow asymmetry is maximal in the region close to the cylinder base. Note that, while the eigenmode structure at $C_{suc}=0.8$ and $C_{suc}=1.0$ is quite similar, the saturated non-linear flow states differ dramatically: the saturated flow is oscillatory at $C_{suc}=0.8$, and steady asymmetric at $C_{suc}=1.0$.

The growth rate σ_r reaches a maximum at $C_{suc}=0.70$ (see Figure 6.1), before transition to asymmetry, and then decreases rapidly in a first stage (until $C_{suc} \approx 1.1$), followed by a rather slow decrease (for $C_{suc} \geq 1.1$). The growth rate becomes zero at the second critical suction coefficient $C_{suc,2}=1.72$, in agreement with the DNS results. For $C_{suc} > 1.6$, σ_r remains smaller than 10^{-3} .

A number of stability computations has been performed with the largest domain ‘XLW’ at $Re=90$, to check the influence of domain size on results. The base (steady symmetric) flows at different suction coefficients in the range $[-0.2, 2.0]$ have been computed with 9×9 elemental resolution on ‘XLW’; stability calculations utilized the same (‘XLW’) domain and elemental resolution (9×9). The leading eigenvalues computed are also presented in Figure 6.1. The agreement in linear temporal frequencies between ‘MAIN’ and ‘XLW’ is very good, with both becoming zero at the same suction coefficient value ($C_{suc}=0.6$). In the range $C_{suc} < 1.4$, the agreement in growth rate is also good, even close to the non-linear transition Unsteady - Steady asymmetric flow, where the discrepancy in non-linear frequency is about 580% (Table 5.2). This shows that domain size has a stronger effect on the saturated non-linear flow state (limit cycle), than on the steady symmetric flow. The trend appears reasonable, as smaller domains impose a symmetric condition at the inflow and lateral boundaries ($U=1, V=0$) much closer to the cylinder than larger domains. The unsteady (instantaneously asymmetric) flow solution is thus much more affected by the symmetric Dirichlet boundary condition at the inflow and lateral boundaries, than the steady symmetric solution. Consequently, stability calculations of symmetric base flows are less sensitive to domain size, in comparison to DNS of saturated flow states.

For $C_{suc} > 1.4$, the relative discrepancy in growth rates between ‘MAIN’ and ‘XLW’

(hardly noticed from Figure 6.1) evidently increases, since σ_r becomes zero at $C_{suc}=1.72$ with ‘MAIN’ and at $C_{suc}=2.27$ with ‘XLW’.

Figure 6.3 shows the growth rates corresponding to all symmetric and asymmetric (stable or unstable) solutions in the steady regime, obtained with domain ‘MAIN’. The growth rates corresponding to the steady symmetric and to the strongly asymmetric steady solutions in the asymmetric regime, obtained with ‘XLW’, are also presented. The vertical dashed lines stand for the critical suction coefficients corresponding to domain ‘MAIN’. The linear temporal frequencies are not represented for clarity, and because they are non-zero only for the asymmetric flows at $C_{suc} < 1.0$.

First, considering only the data obtained with ‘MAIN’, we note that, in the asymmetric regime, growth rates depend exponentially (since linearly in a lin/log plot) on suction coefficient, for both symmetric and asymmetric base flow. The σ_r values obtained with the ‘XLW’ domain, also presented in Figure 6.3, further confirm the exponential dependence of σ_r with C_{suc} , for the two types of base flow. It appears plausible that the exponential dependence would hold up to $C_{suc} \rightarrow \infty$ in an infinite domain. In that case, transition to symmetric flow would never occur, since none of the two growth rates would ever become negative. This strongly supports our previous hypothesis, that only asymmetric flows exist at high suction coefficients, in the limit of infinite flow domain.

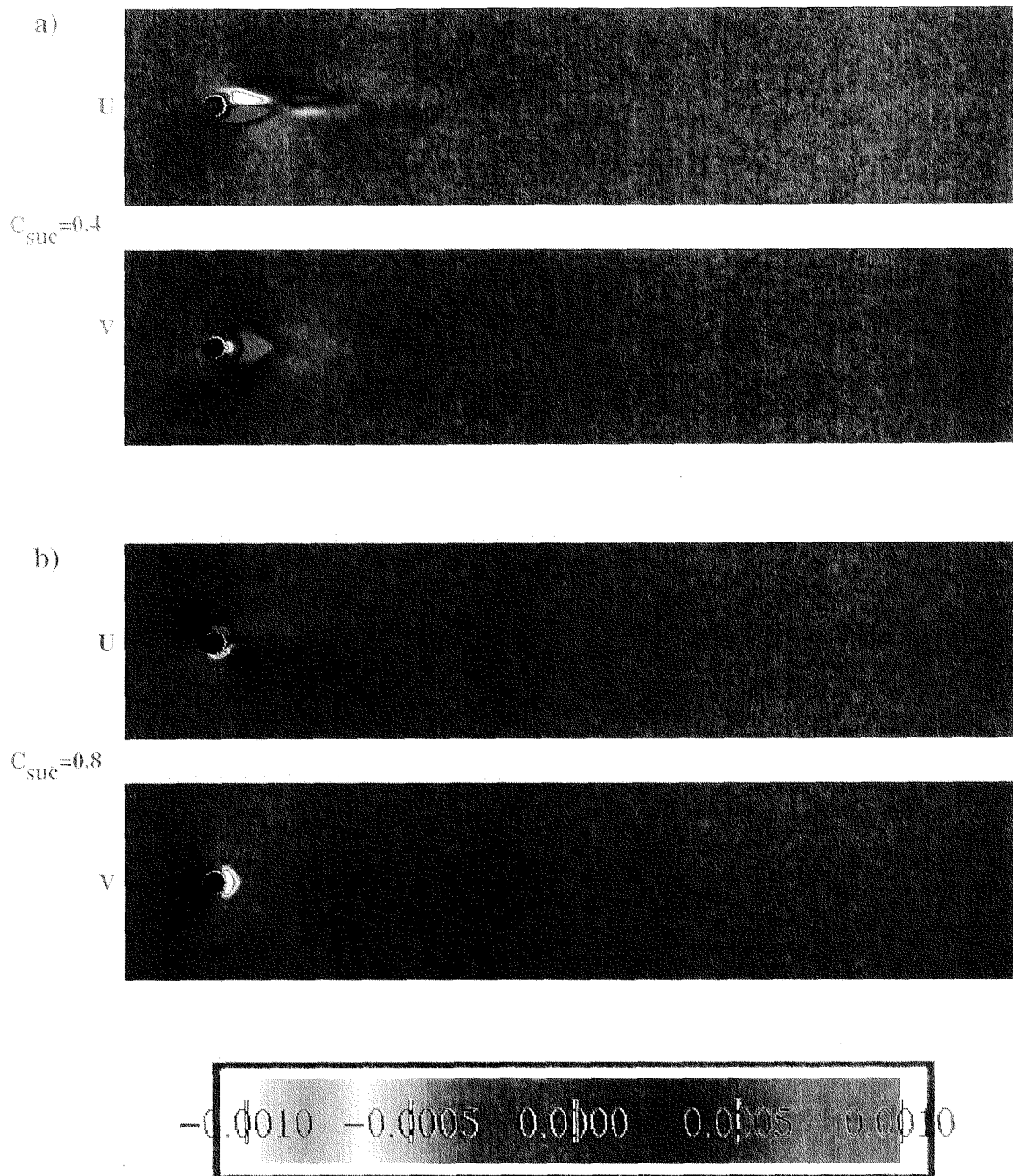


Figure 6.2: $Re=90$: U and V isocontours of the dominant eigenmode corresponding to the base symmetric flow at (a) $C_{suc}=0.4$, (b) $C_{suc}=0.8$.

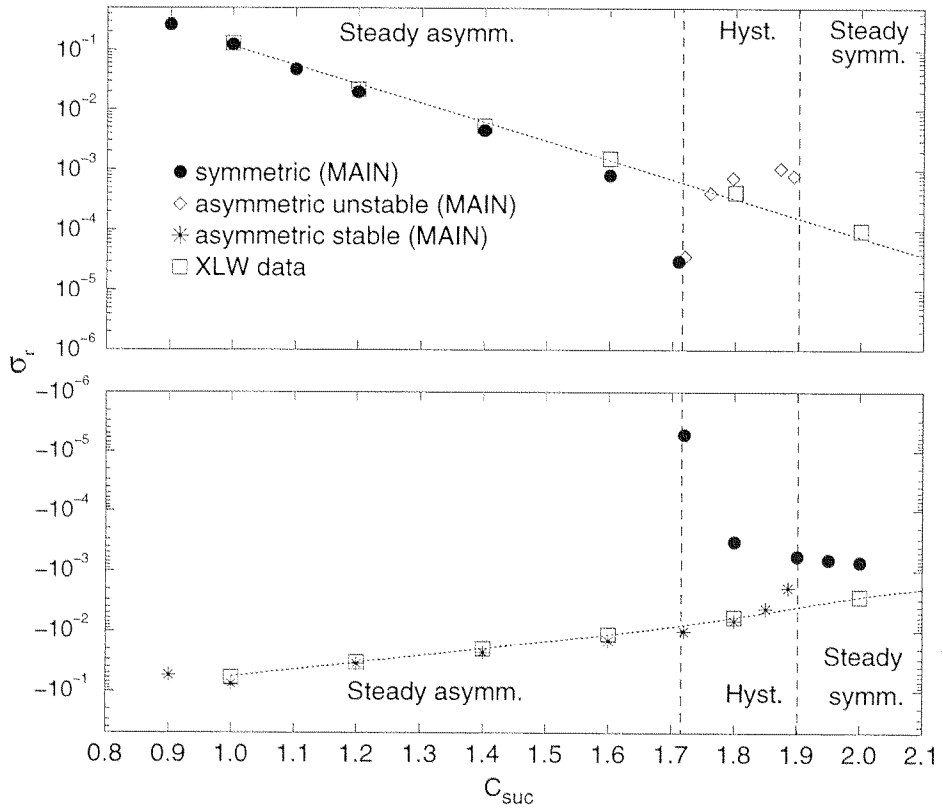


Figure 6.3: $Re=90$: global growth rate σ_r corresponding to different types of base flow, versus suction coefficient C_{suc} . The dotted lines correspond to exponential curve fits of the ‘XLW’ data.

Seite Leer /
Blank leaf

Chapter 7

Conclusions

In the present work, we have investigated the effects of base suction and blowing on the dynamics and stability properties of the flow around a circular cylinder at low Reynolds numbers, using numerical simulation and stability analysis. Both suction and blowing modify the velocity profiles in the near wake, and, consequently, affect the stability properties of the entire flow.

Numerical simulation results show that, at supercritical Reynolds numbers, slight blowing can stabilize the wake, as result of reduced back flow, and, thus, reduced absolute instability in the near wake. High enough suction can also stabilize the wake at supercritical Reynolds numbers, resulting in strongly asymmetric steady flow fields. While suction can have an inherent stabilizing effect, due to the decreased streamwise extent of absolute instability, the primary cause of transition to steady asymmetric flow appears to be the increased flow intermittency with increased suction: the non-linear flow frequency decreases with suction and reaches a zero value, corresponding to transition to steady asymmetric flow. At even higher suction flow rates, we find a subcritical bifurcation to a steady symmetric flow state.

At subcritical Reynolds numbers, sufficient suction can result in global instability and flow unsteadiness, due to increased back flow, and, thus, increased absolute instability in the near wake. With the present definition of control action, no control measure can render the wake unsteady for Reynolds number values below $Re = 17$.

Since low levels of blowing are enough to stabilize the wake at supercritical Reynolds numbers, overall, blowing does not affect the shedding frequency significantly. On the other hand, the drastic reduction in Strouhal number with suction corresponds to strong modifi-

cation of the vortex shedding process. While suction increases drag and lift, slight blowing has the opposite effect, until flow stabilization. Thus, taking into account the difference in the required transpiration flow rates for wake stabilization, blowing is energetically a much more efficient method for stabilizing the wake, than suction. Suction is only preferable when a constant non-zero value of the lift coefficient is desired.

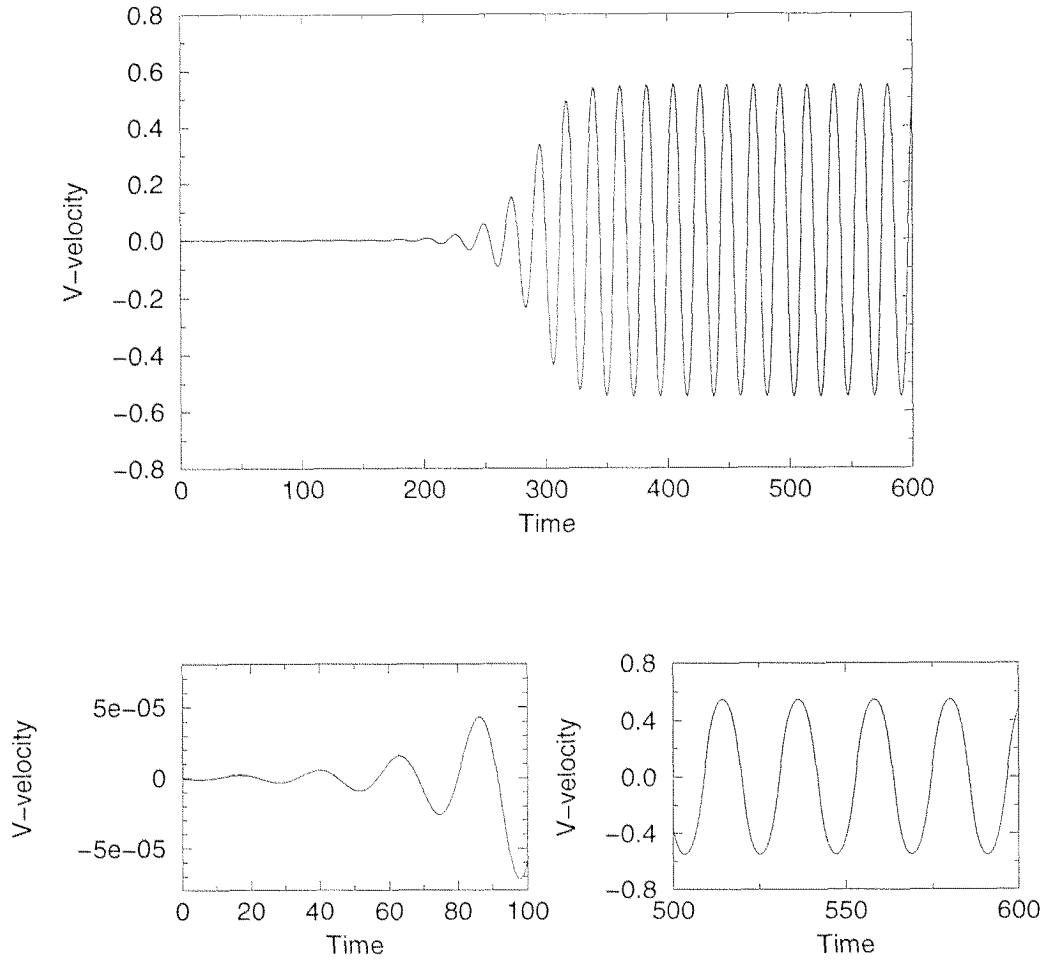
Global linear stability analysis shows that suction drastically increases the global growth rate. After a maximum is reached, the global growth rate rapidly decreases at even higher suction coefficient values, where, in general, the flow is characterized by very slow dynamics. Exploiting this slow dynamics, we developed a feedback control scheme, with which we could stabilize the unstable asymmetric solutions within the hysteresis regime, in the transition from steady asymmetric to steady symmetric flow.

Extensive tests have been performed, to investigate the dependence of the flow dynamics and the transitions reported on domain size. We find that results are only sensitive to domain size at high suction coefficients. In particular, the transition from steady asymmetric to steady symmetric flow is very sensitive to domain width, and, primarily, inflow length. We believe that the presence of inflow and lateral domain boundaries at finite distance from the cylinder in fact provokes this transition, a hypothesis also supported by the global stability analysis results.

Appendix A

Temporal Resolution Tests

(a)



(b)

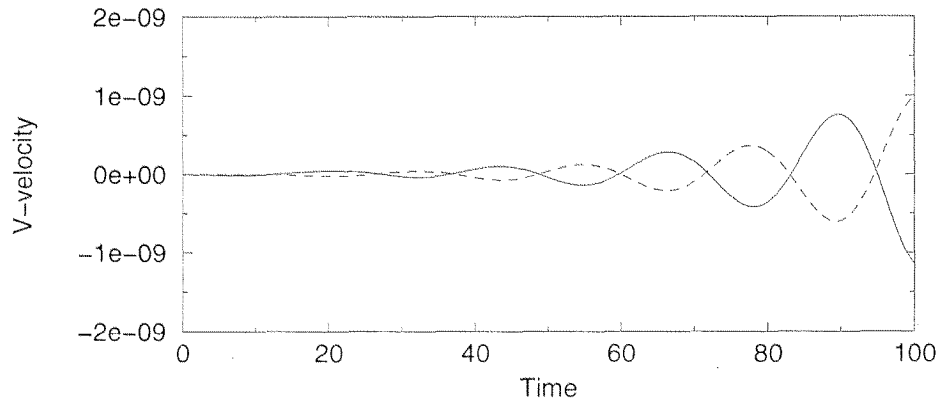
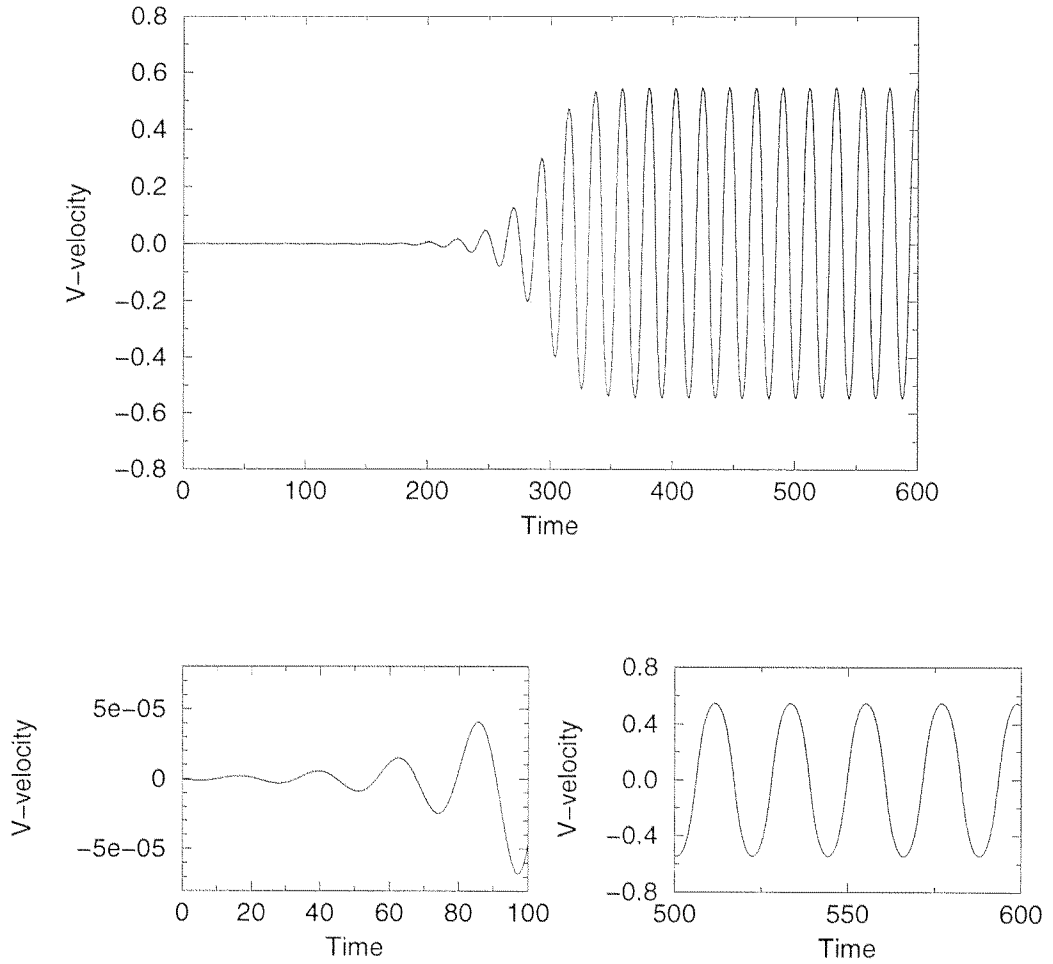


Figure A.1: Time-history of V-velocity at point A: $Re=30$, $C_{suc}=0.90$, 7×7 elemental resolution: — $\Delta t=0.001$, --- $\Delta t=0.002$. (a) Growth and saturation of global mode, using the base flow slightly perturbed as initial condition. (b) Initial stage of global mode development, using the base flow as initial condition.

(a)



(b)

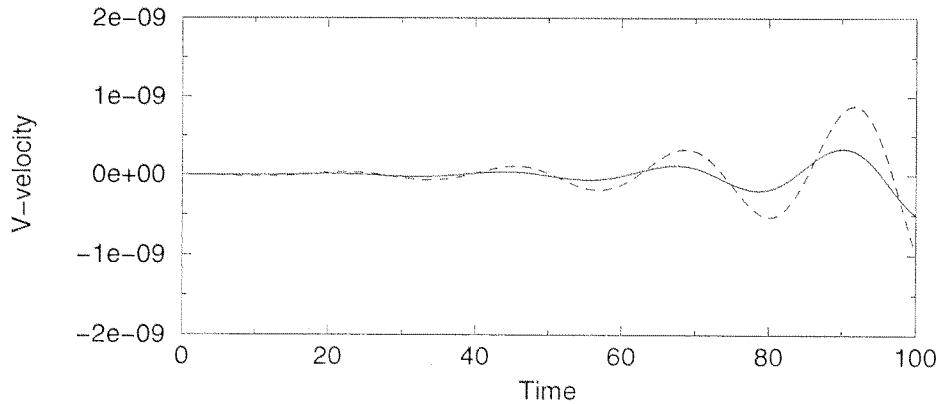
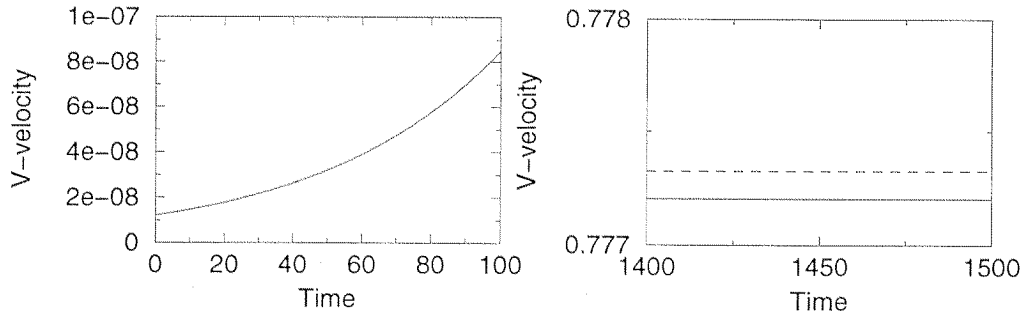
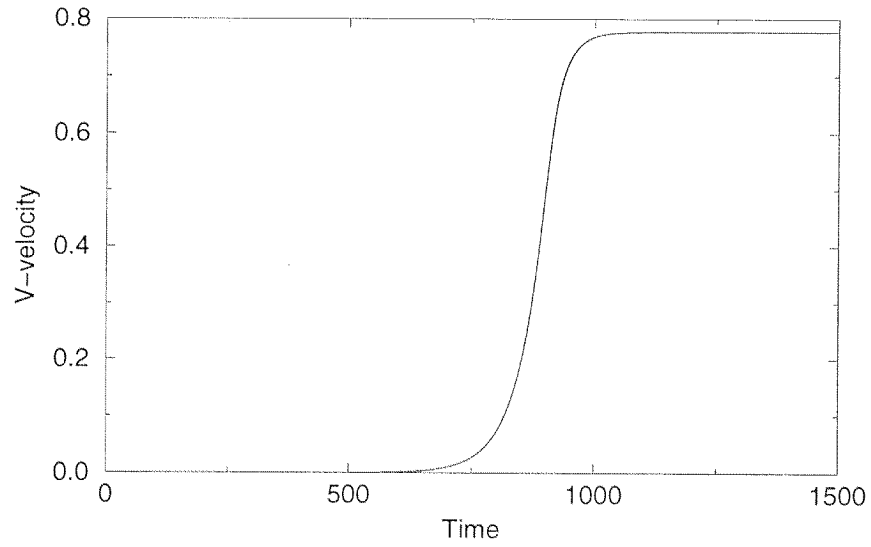


Figure A.2: Time-history of V-velocity at point A: $Re=30$, $C_{suc}=0.90$, 11×11 elemental resolution: — $\Delta t=0.001$, - - - $\Delta t=0.002$. (a) Growth and saturation of global mode, using the base flow slightly perturbed as initial condition. (b) Initial stage of global mode development, using the base flow as initial condition.

(a)



(b)

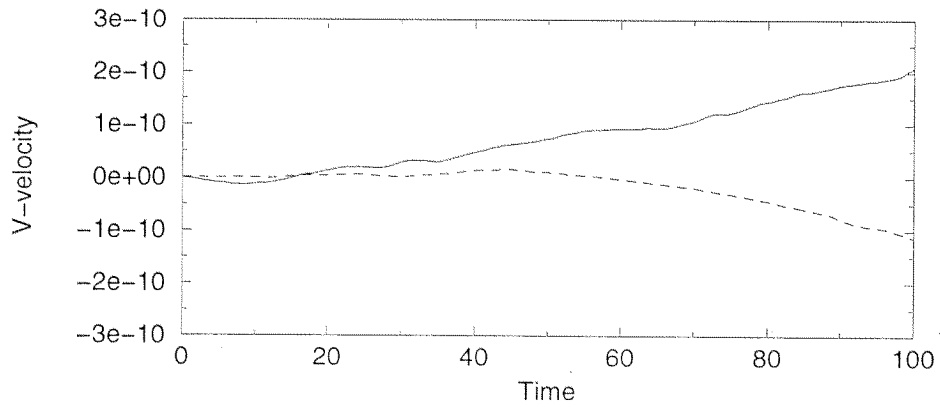
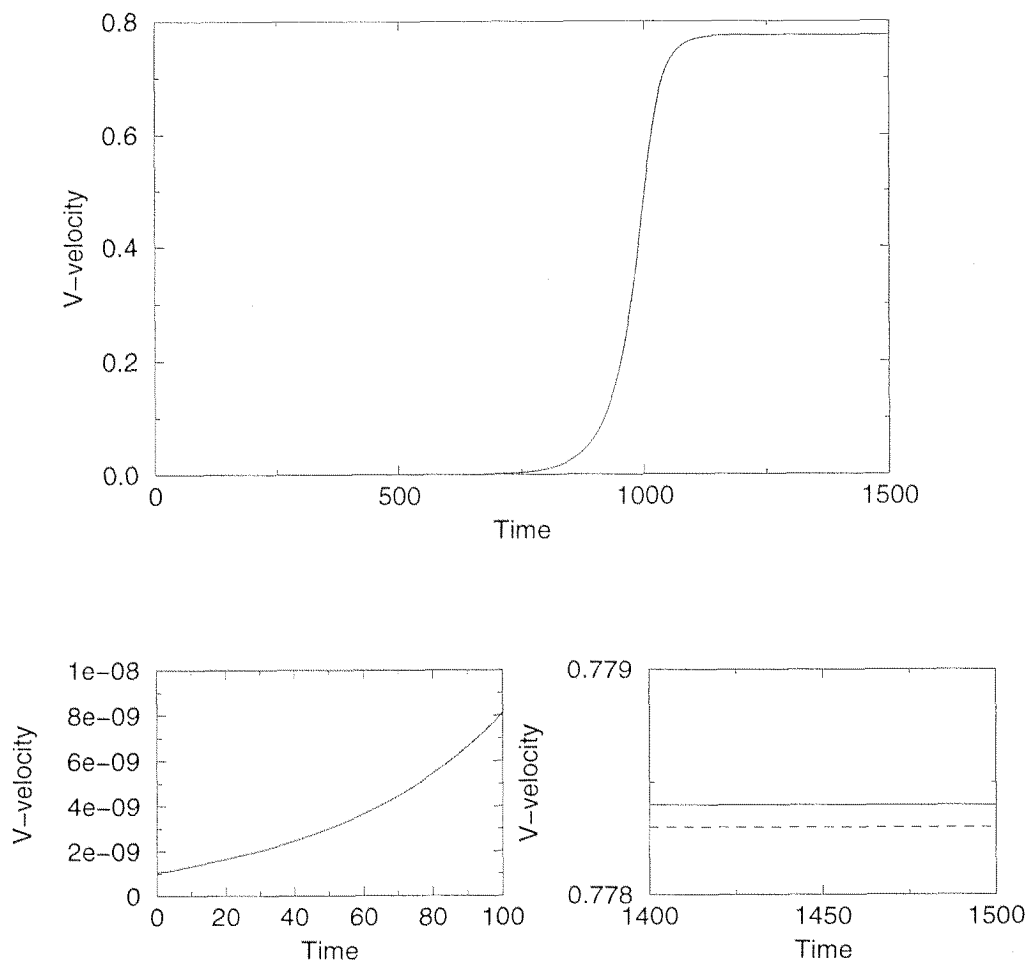


Figure A.3: Time-history of V-velocity at point A: $Re=50$, $C_{suc}=1.50$, 7×7 elemental resolution: $— \Delta t=0.00075$, $--- \Delta t=0.0015$. (a) Growth and saturation of global mode, using the base flow slightly perturbed as initial condition. (b) Initial stage of global mode development, using the base flow as initial condition.

(a)



(b)

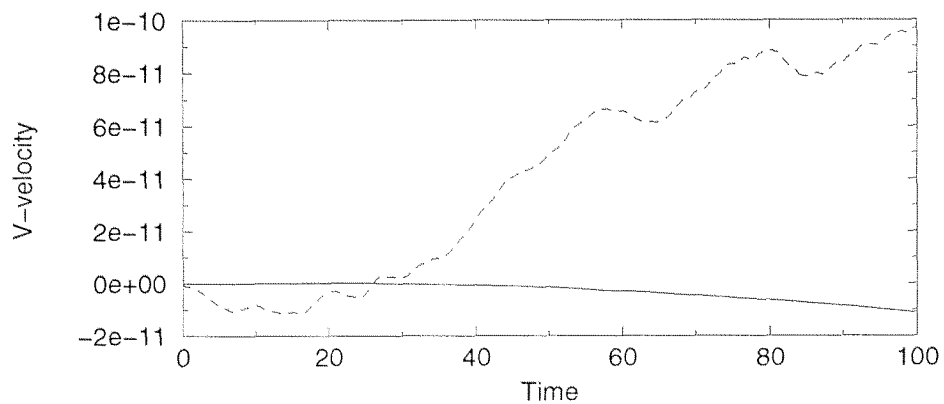
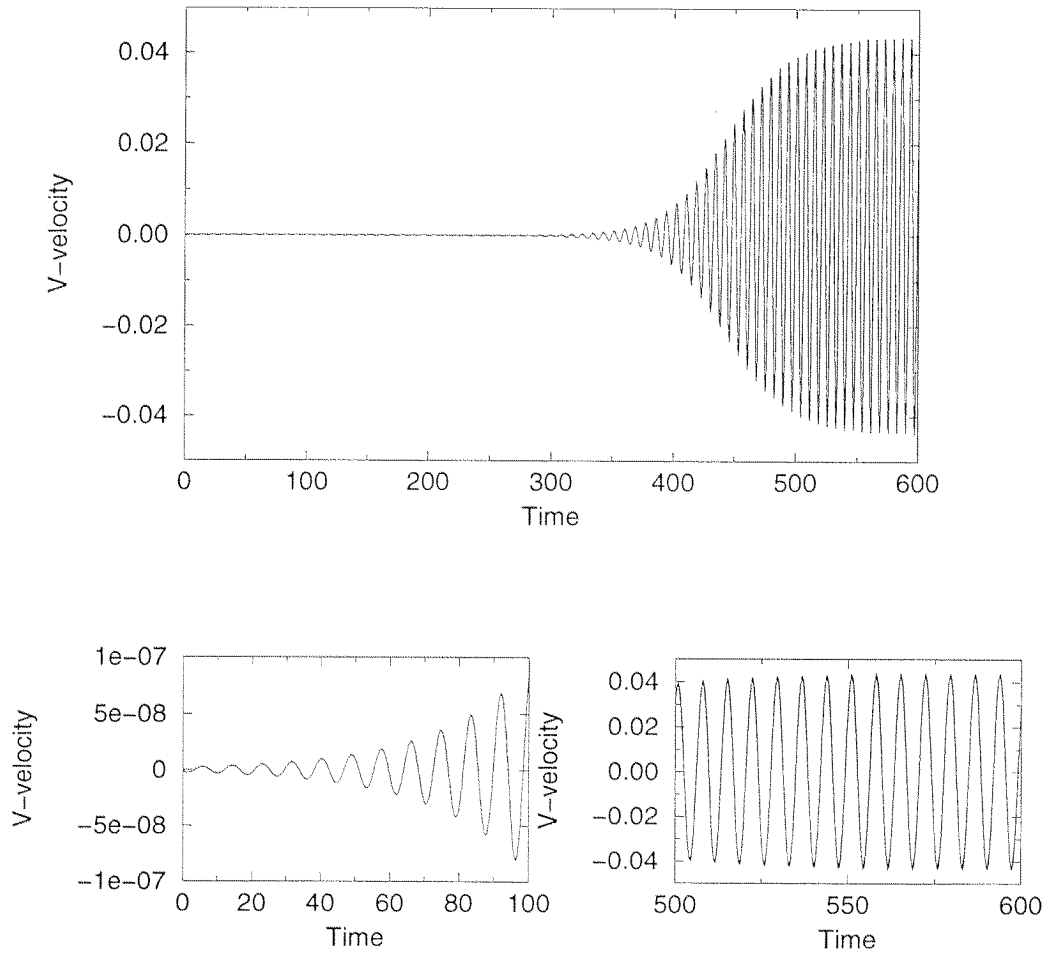


Figure A.4: Time-history of V-velocity at point A: $Re=50$, $C_{suc}=1.50$, 9×9 elemental resolution: — $\Delta t=0.0012$, --- $\Delta t=0.0007$. (a) Growth and saturation of global mode, using the base flow slightly perturbed as initial condition. (b) Initial stage of global mode development, using the base flow as initial condition.

(a)



(b)

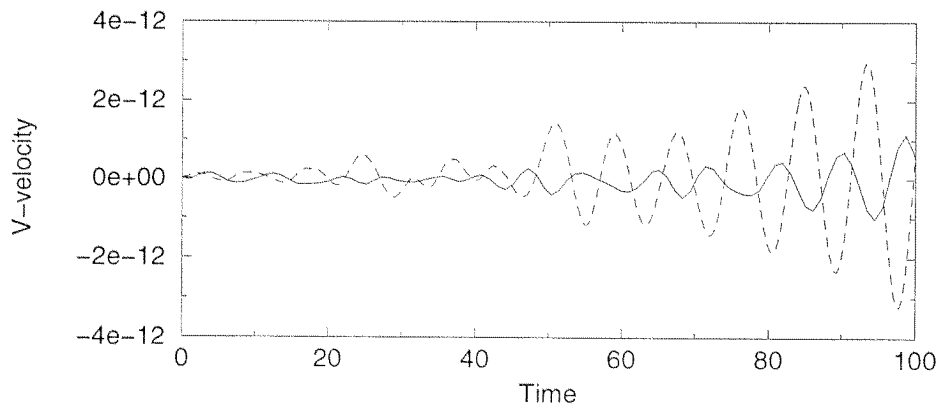
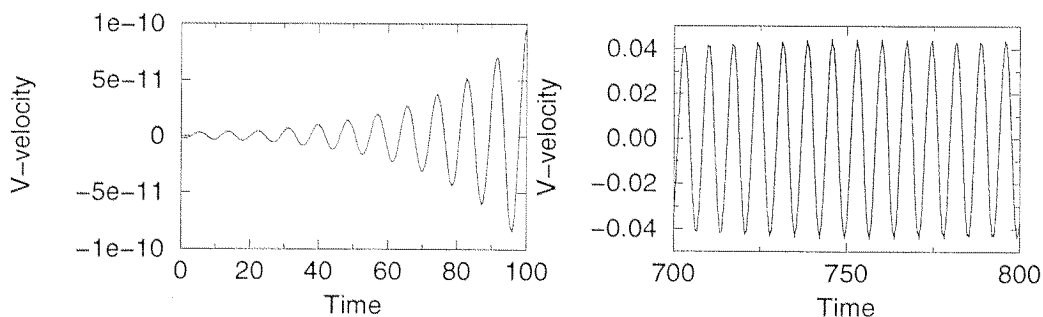
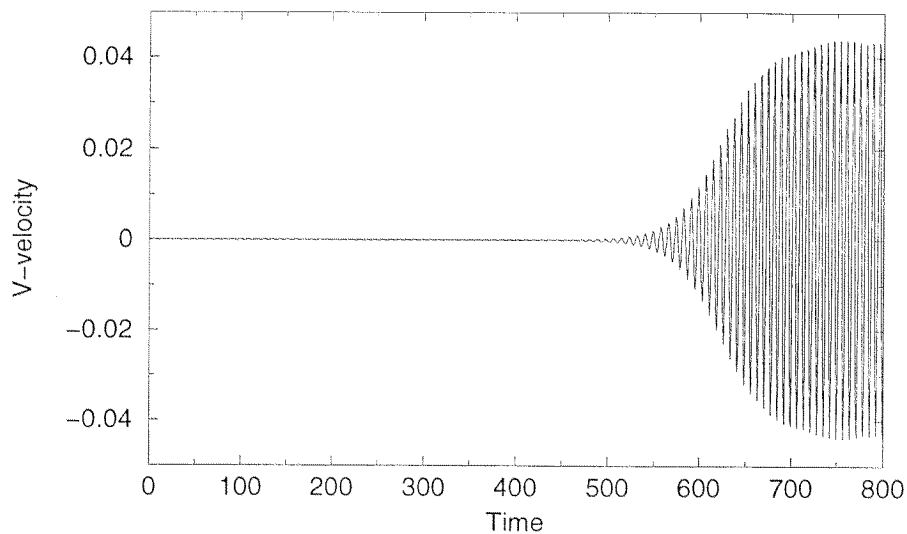


Figure A.5: Time-history of V-velocity at point A: $Re=90$, $C_{suc}=-0.10$, 7×7 elemental resolution: — $\Delta t=0.0075$, --- $\Delta t=0.015$. (a) Growth and saturation of global mode, using the base flow slightly perturbed as initial condition. (b) Initial stage of global mode development, using the base flow as initial condition.

(a)



(b)

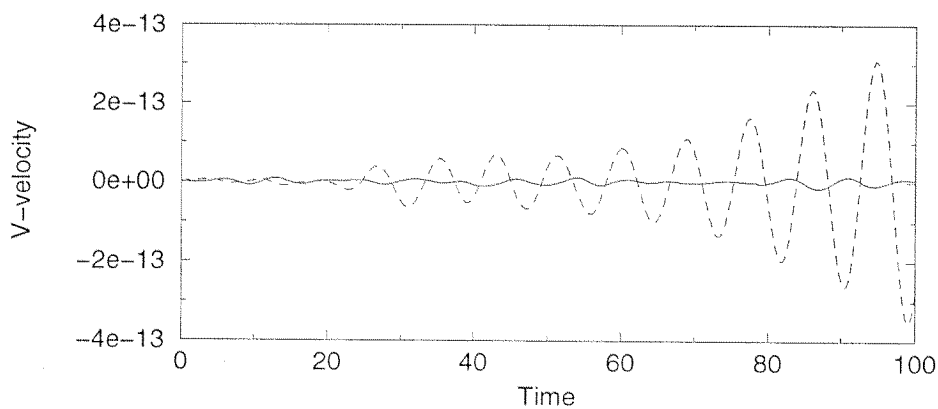
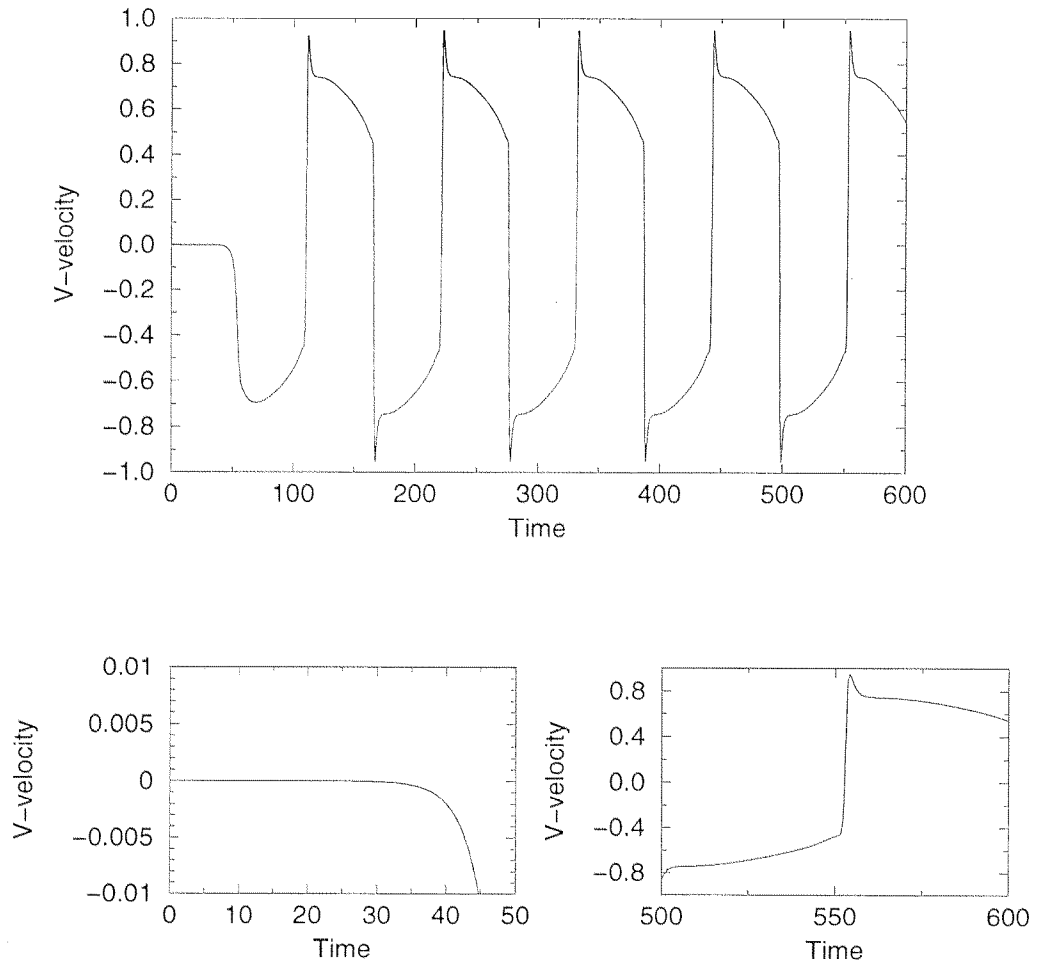


Figure A.6: Time-history of V-velocity at point A: $Re=90$, $C_{suc}=-0.10$, 9×9 elemental resolution: — $\Delta t=0.0075$, --- $\Delta t=0.015$. (a) Growth and saturation of global mode, using the base flow slightly perturbed as initial condition. (b) Initial stage of global mode development, using the base flow as initial condition.

(a)



(b)

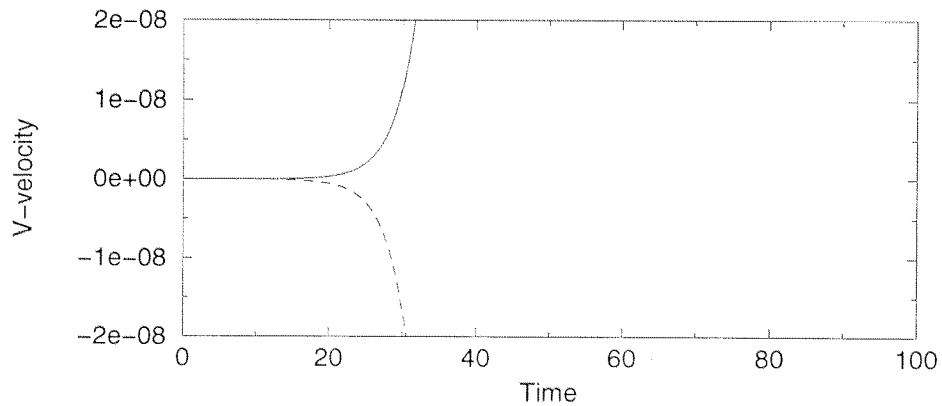
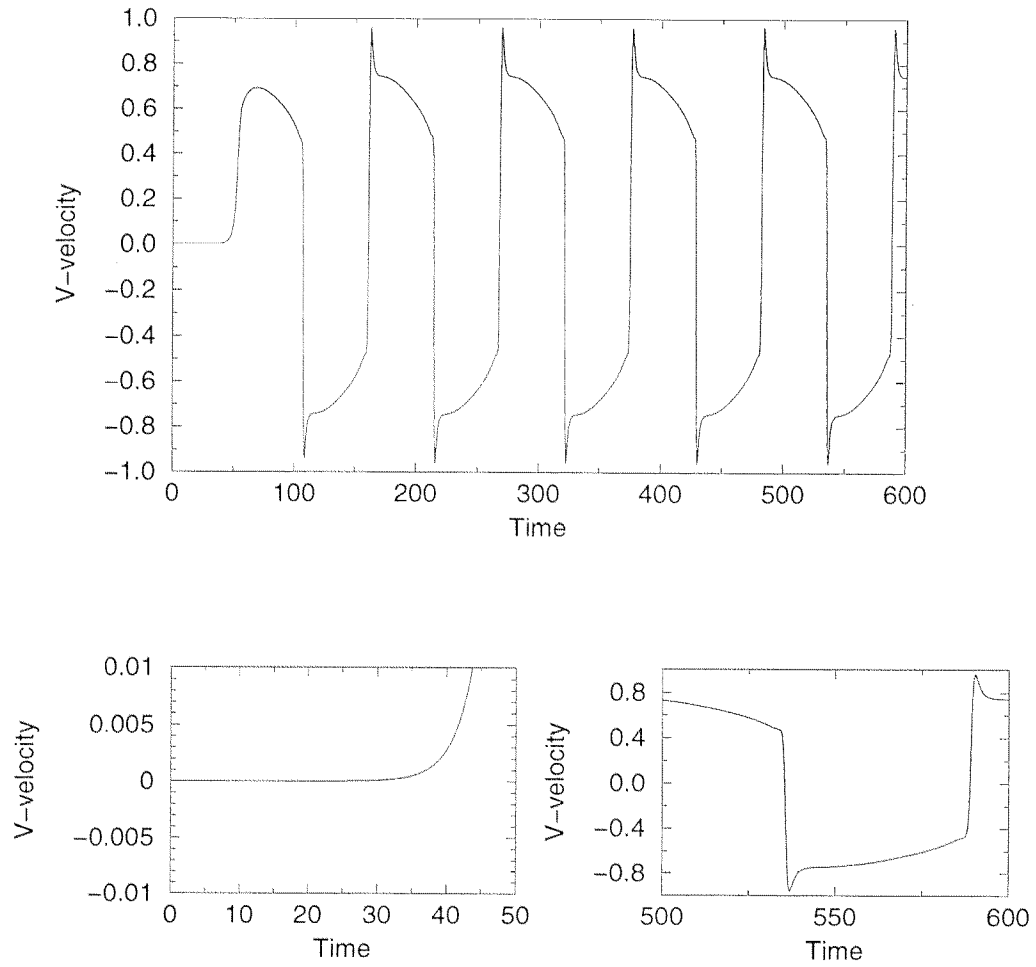


Figure A.7: Time-history of V-velocity at point A: $Re=90$, $C_{suc}=0.85$, 7×7 elemental resolution: — $\Delta t=0.001$, --- $\Delta t=0.002$. (a) Growth and saturation of global mode, using the base flow slightly perturbed as initial condition. (b) Initial stage of global mode development, using the base flow as initial condition.

(a)



(b)

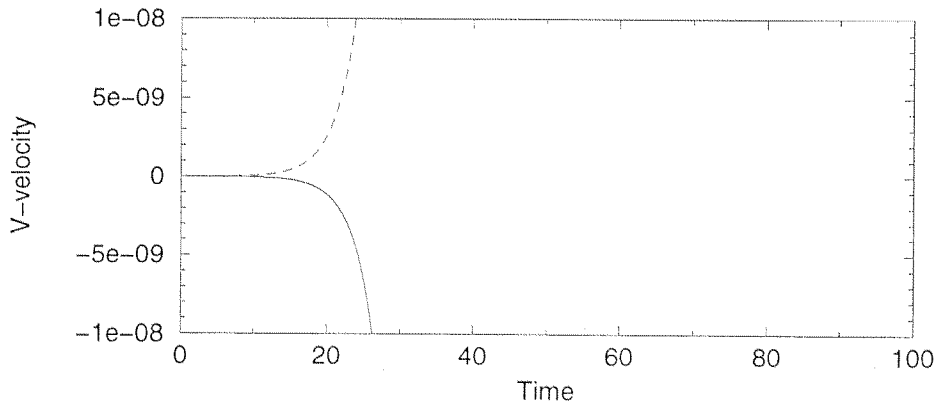


Figure A.8: Time-history of V-velocity at point A: $Re=90$, $C_{suc}=0.85$, 9×9 elemental resolution: — $\Delta t=0.001$, --- $\Delta t=0.002$. (a) Growth and saturation of global mode, using the base flow slightly perturbed as initial condition. (b) Initial stage of global mode development, using the base flow as initial condition.

Bibliography

- [1] Acrivos A., Leal L.G., Snowden D.D. and Pan F., “Further experiments on steady separated flows past bluff objects”, *J. Fluid Mech.* **34**, 25 (1968).
- [2] Apelt C.J. and West G.S., “The effects of wake splitter plates on bluff-body flow in the range $10^4 < R < 5 \times 10^4$: Part 2”, *J. Fluid Mech.*, **71**, 145 (1975).
- [3] Apelt C.J., West G.S. and Szewczyk A.A., “The effects of wake splitter plates on the flow past a circular cylinder in the range $10^4 < R < 5 \times 10^4$ ”, *J. Fluid Mech.*, **61**, 187 (1973).
- [4] Barkley D. and Henderson R.D., “Three-dimensional Floquet stability analysis of the wake of a circular cylinder”, *J. Fluid Mech.*, **322**, 215 (1996).
- [5] Berger E., “Unterdrückung der laminaren Wirbelströmung und des Turbulenzeinsatzes der Kármánschen Wirbelstrasse im Nachlauf eines schwingenden Zylinders”, *Jahrbuch der WGLR* (ed. H. Blenk), Fried. Vieweg, Braunschweig, 164 (1964).
- [6] Berger E., “Suppression of vortex shedding and turbulence behind oscillating cylinders”, *Phys. Fluids Suppl.* **10**, 191 (1967).
- [7] Braza M., Chassaing P. and Minh H., “Numerical study and physical analysis of the pressure and velocity fields in the near wake of a circular cylinder”, *J. Fluid Mech.*, **165**, 79 (1986).
- [8] Chomaz J.M. , Huerre P. and Redekopp L.G., “Bifurcations to local and global modes in spatially developing flow”, *Phys. Rev. Lett.* **60**, 25 (1988).

- [9] Chomaz J.M., Huerre P. and Redekopp L.G., “The effect of nonlinearity and forcing on global modes”, *New trends in nonlinear dynamics and pattern-forming phenomena: the geometry of Nonequilibrium* (edited by P. Coulet and P. Huerre), 259 (1990).
- [10] Chomaz J.M. , Huerre P. and Redekopp L.G., “A frequency selection criteria in spatially developing flows”, *Stud. Appl. Maths* **84**, 119 (1991).
- [11] Dennis S.C.R. and Chang G.Z., “Numerical solutions for steady flow past a circular cylinder at Reynolds numbers up to 100”, *J. Fluid Mech.* **42**, 471 (1970).
- [12] Drazin P.G. and Reid W.H., *Hydrodynamic stability*, Cambridge University Press (1981).
- [13] Düsek J., “Spatial structure of the Bénard von Kármán instability”, *Eur. J. Mech. B/Fluids* **15**, 619 (1996).
- [14] Düsek J., Le Gal P. and Fraunie P., “A Numerical and theoretical study of the first Hopf bifurcation in a cylinder wake”, *J. Fluid Mech.* **264**, 59 (1994).
- [15] Edwards W.S., Tuckerman L.S., Friesner R.A. and Sorensen D.C., “Krylov methods for the incompressible Navier-Stokes equations”, *J. Comp. Phys.* **110**, 82 (1994).
- [16] Fey U., König M. and Eckelman H., “A new Strouhal - Reynolds - number relationship for the circular cylinder in the range $47 < Re < 2 \times 10^5$ ”, *Phys. Fluids Letters*, **10** (7), 1547 (1998).
- [17] Fornberg B., “Steady viscous flow past a circular cylinder up to Reynolds number 600”, *J. Comp. Phys.* **61**, 297 (1985).
- [18] Fornberg B., “Computing incompressible flows past blunt bodies - A historical overview”, *Numerical Methods for Fluid Dynamics* (edited by Baines M.J. and Morton K.W.), 15 (1993).
- [19] Gaster M., “A note on the relation between temporally-increasing and spatially-increasing disturbances in hydrodynamic stability”, *J. Fluid Mech.* **14**, 222 (1962).
- [20] Gerrard J.H., “The mechanics of the formation region of vortices behind bluff bodies”, *J. Fluid Mech.* **25**, 401 (1966).

- [21] Gillies E., “Low dimensional control of the circular cylinder wake”, *J. Fluid Mech.* **371**, 157 (1998).
- [22] Golub G.H. and Van Loan C.F., *Matrix computations*, John Hopkins University Press, Baltimore, Maryland (1983).
- [23] Graham W.R., Repaire J. and Tang K.Y., “Optimal control of vortex shedding using low-order models. Part I – Open loop model development”, *Int. J. Numer. Meth. Engng.* **44**, 945 (1999a).
- [24] Graham W.R., Repaire J. and Tang K.Y., “Optimal control of vortex shedding using low-order models. Part II – Model-based control”, *Int. J. Numer. Meth. Engng.* **44**, 973 (1999b).
- [25] Green R.B. and Gerrard J.H., “Vorticity measurements in the near wake of a circular cylinder at low Reynolds numbers”, *J. Fluid Mech.* **246**, 675 (1993).
- [26] Hammache M. and Gharib M., “An experimental study of the parallel and oblique vortex shedding from circular cylinders”, *J. Fluid Mech.* **232**, 567 (1991).
- [27] Hammond D.A. and Redekopp L.G., “Global dynamics of symmetric and asymmetric wakes”, *J. Fluid Mech.* **331**, 231 (1997a).
- [28] Hammond D.A. and Redekopp L.G., “Global dynamics and aerodynamic flow vectoring of wakes”, *J. Fluid Mech.* **338**, 231 (1997b).
- [29] Hannemann K. and Oertel H., “Numerical simulation of the absolutely and convectively unstable wake”, *J. Fluid Mech.* **199**, 55 (1989).
- [30] Henderson R.D., “Details of the drag curve near the onset of vortex shedding”, *Phys. Fluids* **7** (9), 2102 (1995).
- [31] Huerre P. and Monkewitz P.A., “Local and global instabilities in spatially developing flows”, *Ann. Rev. Fluid Mech.* **22**, 473 (1990).
- [32] Jackson C.P., “A finite-element study of the onset of vortex shedding in flow past variously shaped bodies”, *J. Fluid Mech.* **182**, 23 (1987).

- [33] von Kármán T., “Über den Mechanismus des Widerstandes, den ein bewegter Körper in einer Flüssigkeit erfährt”, Göttingen Nachrichten, Mathematische Physikalische Klasse, 509 (1911).
- [34] Karniadakis G.E., Israeli M. and Orszag S.A., “High-order splitting methods for the incompressible Navier-Stokes equations”, *J. Comp. Phys.* **97**, 414 (1991).
- [35] Karniadakis G.E. and Triantafyllou G.S., “Frequency selection and asymptotic states in laminar wakes”, *J. Fluid Mech.* **199**, 441 (1989).
- [36] Karniadakis G.E. and Triantafyllou G.S., “Three-dimensional dynamics and transition to turbulence in the wake of bluff objects”, *J. Fluid Mech.* **238**, 1 (1992).
- [37] Koch W., “Local instability characteristics and frequency determination of self-excited wake flows”, *J. Sound Vib.* **99**, 53 (1985).
- [38] Landau L.D., “On the problem of turbulence”, *C.R. Acad. Sci. U.S.S.R.* **10** (1944).
- [39] Leu T.S. and Ho C.M., “Control of global instability in a non-parallel near wake”, *J. Fluid Mech.* **404**, 345 (2000).
- [40] Mathis C., Provansal M. and Boyer L., “The Bénard-von Kármán instability: an experimental study near the threshold”, *J. Phys. Lett. (Paris)* **45**, 483 (1984).
- [41] Min C. and Choi H., “Suboptimal feedback control of vortex shedding at low Reynolds numbers”, *J. Fluid Mech.* **401**, 123 (1999).
- [42] Monkewitz P.A., “Feedback control of global oscillations in fluid systems”, AIAA Paper 89-0991 (1989).
- [43] Monkewitz P.A., “Modeling of self-excited wake oscillations by amplitude equations”, *Exp. Therm. and Fluid Sci.* **12**, 175 (1996).
- [44] Monkewitz P.A., Huerre P. and Chomaz J.M., “Global linear stability analysis of weakly non-parallel shear flows”, *J. Fluid Mech.* **251**, 1 (1993).
- [45] Monkewitz P.A. and Nguyen L.N., “Absolute instability in the near-wake of two-dimensional bluff bodies”, *J. Fluids Struct.* **1**, 165 (1987).

- [46] Mutschke G., Gerbeth G., Shatrov V. and Tomboulides A., “Two- and three-dimensional instabilities of the cylinder wake in an aligned magnetic field”, *Phys. Fluids* **9** (11), 3114 (1997).
- [47] Nishioka M. and Sato H., “Mechanism of determination of the shedding frequency of vortices behind a cylinder at low Reynolds numbers”, *J. Fluid Mech.* **89**, 49 (1978).
- [48] Noack B.R. and Eckelmann H., “A global stability analysis of the steady and periodic cylinder wake”, *J. Fluid Mech.* **270**, 297 (1994).
- [49] Park D.S., “Theoretical analysis of feedback control of vortex shedding at slightly supercritical Reynolds numbers”, *Eur. J. Mech. B/Fluids* **13**, 387 (1994).
- [50] Park D.S., Ladd D.M. and Hendricks E.W., “Feedback control of von Kármán vortex shedding behind a circular cylinder at low Reynolds number”, *Phys. Fluids* **6**, 2390 (1994).
- [51] Patera A.T., “A spectral element method for fluid dynamics; laminar flow in a channel expansion”, *J. Comp. Phys.* **54**, 468 (1984).
- [52] Provansal M., Mathis C. and Boyer L., “Bénard-von Kármán instability: transient and forced regimes”, *J. Fluid Mech.* **182**, 1 (1987).
- [53] Rayleigh L., “On the question of stability of the flow of fluids”, *Phil. Mag. (5)* **34**, 59 (1892).
- [54] Reynolds O., “On the dynamical theory of incompressible viscous flows and the determination of a criterion”, *Phil. Trans. R. Soc. London* **186**, 123 (1883).
- [55] Roshko A., “On the development of turbulent wakes from vortex streets”, NACA, Rep. 1191 (1954).
- [56] Roshko A., “On the wake and drag of bluff bodies”, *J. Aero. Sc.* **22**, 124 (1955).
- [57] Roshko A., “Perspectives on bluff body aerodynamics”, *J. of Wind Eng. and Ind. Aero.* **49**, 79 (1993).
- [58] Roussopoulos K., “Feedback control of vortex shedding at low Reynolds numbers”, *J. Fluid Mech.* **248**, 267 (1993).

- [59] Roussopoulos K. and Monkewitz P.A., “Nonlinear modeling of vortex shedding control in cylinder wakes”, *Physica D* **97**, 264 (1996).
- [60] Schumm M., Berger E. and Monkewitz P.A., “Self-excited oscillations in the wake of two-dimensional bluff bodies and their control”, *J. Fluid Mech.* **271**, 17 (1994).
- [61] Stansby P.K., “The effects of end plates on the base pressure coefficient of a circular cylinder”, *Aerosp. J.* **78**, 36 (1974).
- [62] Strouhal V., “Über eine besondere Art der Tonerregung”, *Annalen der Physik und Chemie*, Bd. 5, Nr.9 (1878).
- [63] Strykowski P.J. and Sreenivasan K.R., “On the formation and suppression of vortex ‘shedding’ at low Reynolds numbers”, *J. Fluid Mech.* **218**, 71 (1990).
- [64] Stuart J.T., “On the non-linear mechanics of hydrodynamic stability”, *J. Fluid Mech.* **4**, 1 (1958).
- [65] Stuart J.T., “Non-linear stability theory”, *Ann. Rev. Fluid Mech.* **3**, 347 (1971).
- [66] Stuart J.T. and Watson J., “On the non-linear mechanics of wave disturbances in stable and unstable parallel flows”, *J. Fluid Mech.* **9**, 353 (1960).
- [67] Takami H. and Keller H.B., “Steady viscous flow of an incompressible fluid past a circular cylinder”, *Phys. Fluids Supp. II* **12**, 51 (1969).
- [68] Taneda S., “Visual observations of the flow past a circular cylinder performing a rotary oscillation”, *J. Phys. Soc. Japan* **45**, 1038 (1978).
- [69] Tokumaru P.T. and Dimotakis P.E., “Rotary oscillation control of a cylinder wake”, *J. Fluid Mech.* **224**, 77 (1991).
- [70] Tomboulides A., Triantafyllou G.S. and Karniadakis G.E., “A new mechanism of period doubling in free shear flows”, *Phys. Fluids. A* **4**, 1329 (1992).
- [71] Tomboulides A., “Direct and large-eddy simulation of wake flows: flow past a sphere”. PhD Thesis, Department of Mechanical and Aerospace Engineering, Princeton University, USA (1993).

- [72] Tritton D.J., “Experiments on the flow past a circular cylinder at low Reynolds numbers”, J. Fluid Mech. **6**, 547 (1959).
- [73] Triantafyllou G.S., Triantafyllou M.S. and Chryssostomidis C., “On the formation of vortex streets behind stationary cylinders”, J. Fluid Mech. **170**, 461 (1986).
- [74] Twiss R.Q., “Propagation in electron-ion streams”, Phys. Rev. **88**, 1392 (1952).
- [75] Watson J., “On spatially-growing finite disturbances in plane Poiseuille flow”, J. Fluid Mech. **14**, 211 (1962).
- [76] Williamson C.H.K., “Defining a universal and continuous Strouhal-Reynolds number relationship for the laminar vortex shedding of a circular cylinder”, Phys. Fluids **31** (10), 2742 (1988).
- [77] Williamson C.H.K., “Vortex dynamics in the cylinder wake”, Ann. Rev. Fluid Mech. **28**, 477 (1996).
- [78] Wong H.Y., “Wake flow stabilization by the action of base bleed”, J. Fluids Engng., **107**, 378 (1985).
- [79] Wood C.J., “The effect of base bleed on a periodic wake”, J. R. Aero. Soc. **68**, 477 (1964).
- [80] Zdravkovich M.M., “Review and classification of various aerodynamic and hydrodynamic means for suppressing vortex shedding”, J. Wind Engng. and Ind. Aero. **7**, 145 (1981).
- [81] Zdravkovich M.M., *Flow around circular cylinders. Volume 1*, Oxford University Press (1997).

Curriculum Vitae

- 23.6.1972 Born in Courbevoie, France
- 1978-1983 Primary school, Angers, France
- 1983-1990 Secondary school, Angers, France
- 1990-1992 Classes préparatoires, Nantes, France
- 1992-1995 Undergraduates studies in Hydraulics and Fluid Mechanics,
National Institute of Technology (INP), Toulouse, France.
- 1995 Diploma
- 1994-1995 Diplôme d'Etudes Approfondies (DEA), INP, Toulouse, France
- 1995-1997 Research scientist, Institute of Hydraulics,
Hydrology and Water Resources Management,
University of Technology, Vienna, Austria
- 1997-2000 Doctoral student, Institute of Energy Technology,
Federal Institute of Technology, Zürich, Switzerland